Cation Exchange in Nanocrystals Towards Novel Ternary Copper Chalcogens

By

Christopher George Sharp

Dissertation
Submitted to the Faculty of the
Graduate School of Vanderbilt University
in partial fulfillment of the requirements
for the degree of

DOCTOR OF PHILOSOPHY

in
Chemistry
May 12, 2022
Nashville, Tennessee

Approved:

Janet E. Macdonald, Ph.D.
Timothy P. Hanusa, Ph.D.
Nathan D. Schley, Ph.D.
Sean B. Seymore, Ph.D.

DEDICATION

This thesis is dedicated to my peers whose experiments don’t work.

Sorry. Science be like that sometimes.

ACKNOWLEDGEMENTS

The following work was supported by the Vanderbilt University Chemistry Department, National Science Foundation grants SUSChem CHE 1253105, CHE 1905265, and EPS-1004083, and the Mitchum E. Warren Fellowship. Portions of this work were performed at the Vanderbilt Institute of Nanoscale Science and Engineering. Financial support for travel and registration at academic conferences were provided by the Graduate School at Vanderbilt as well as the American Chemical Society – Nashville Section.

Janet, of all the traits you possess which have made you a successful PI, your transparency has provided me with invaluable guidance. Your oddly kind but blunt mentorship imparted wisdom which both discouraged me from repeating mistakes while also preventing potential ones. Thank you for your understanding, patience and grace while helping me stumble my way to the finish line. Dr. Strouse, thank you for opening your lab to me at the start of my research journey; Dave, I'll forever appreciate your guidance during throughout my time undergraduate career from analytical lab (though I'm still annoyed you gave me an A-) to the Strouse lab. Dr. McBride, your continued support with the VINSE microscopy core has been invaluable.

To the Bierhaus Boys. The Wedgewood Refugees. The Charlotte Citizens. Y'all have been the best trivia/drinking/sporting/gaming friends a guy could ask for (the following is in alphabetical order so that those listed do not argue about their order of mention). Andrey, thanks for always being our hypeman. Could always count on you to turn a good time into a great time. Try not to get anyone else kicked out of Fleet Street in the future. Nathan – in addition to your friendship – thank you for your pragmatism. Every squad needs a safety officer. Thanks for keeping our antics from going from bad to worse without being a buzz kill. Will, thank you for being the nucleation point. From the first nights in the Stein club to the 5 years that were to follow,

all of that might not have happened were it not for you. I wish that I could say more but I'm pretty burnt out on writing this, so I'll just tell you in person. Y'all were always there through thick and thin and are basically family, now. Let's all make sure to keep in touch on the regular.

To the former Macdonald group, thank you for your experience navigating both the research space and graduate life. Emil, your mentorship over my first year was instrumental for my entire PhD as was your Spotify playlist. Evan, I'm grateful for you preparing me to take over the XRD core as well your advice on career plans from an industry perspective. Jordan, we kept your sketches up at your desk; thanks for all the art and design tips which have been great for posters. Andrew, thanks for organizing tabletop game nights. We didn't do it much, but your D&D campaigns were a hoot. Alice and Suresh, y'all were amazing collaborators. It's an honor and a privilege to share names on your work.

To the next Macdonald group, y'all have certainly made these past 5ish years memorable. Maddy, thanks for being our resident engineer; those broken pumps and GC never stood a chance. Danielle, thanks for your organic expertise; after Andrew's departure, it was a skillset we desperately needed. Jeremy, take good care of Cammie (the Rigaku Smartlab). I know she'll be in good hands with you around. No, you can't change her name. Lexie, make sure you keep Jeremy in check. I realize that's an overwhelming job, but someone has to keep him from wilin' out. I know you can do it. Emma and Tony, among other things thanks for the lab banter. Your dynamic has provided brief respite from the research slog more than a few times. Pete, good luck in med school. Also make sure to keep sending me hot take sports predictions. Those are always a riot.

To my remaining colleagues, there's so many contributions that will go unacknowledged. Henry, being friends with you has been a scheduling crisis. I really wish we'd hung out more than we have, but I'll always remember our late hangouts, friendly debates, and the briefly lived weekly

Anime Night. Aaron and Velia, thanks for helping me get acquainted with Nashville so early on. Y'all knew so many of the best local spots and were always down to clown. All those movie nights will be sorely missed. Caleb and Kelsey, in the same vein thanks for being monthly dinner night buddies. We had a good thing going until y'all decided to graduate and become real adults with jobs and stuff. I hope to see you on the other side, shortly. Give Russ some head scritches for me.

Sophie, I don't think I could've asked for a better roommate. You took a gamble on some rando you met exactly once and 5 years later you're one of my closest confidants. There's a lot I'm going to miss like you letting me test your food for poison (none found, yet; must continue trials) or our unprompted hours long deep conversations. We've shared so many things which have vastly impacted my world view, spirituality, fears and insecurities, etc. that it's hard to describe the full extent to which you've impacted my life. My biggest hope is that I contributed to yours at least a fraction of what you've contributed to mine.

To my mom and dad, I know we don't see eye to eye on a lot of things, but you guys have always supported me in your own way. You've always set high expectations which is where your criticism comes from, but I understand it is out of a desire to see me succeed. I know my path hasn't been one which is easy for you to understand with respect to motivation or direction, but you've always tried your best to be actively involved every step of the way. Thank you for the continued support and dedication that only parents can provide.

TABLE OF CONTENTS

LIST OF TABLES

LIST OF FIGURES

Chapter 1

INTRODUCTION

1.1 Introduction to Nanomaterials

While humanity continues to pursue the scientific and technologic advancements which have radically shaped modern society, our way of life is increasingly at odds with its own unsustainability. As our ancient quest for survivability has given way to modern comforts, consumption and resource scarcity have become ever more prevalent issues. Our growing population demands energy, raw materials, and nourishment at a rate far exceeding natural replenishment rates.[1–4] Pressing issues include but are not limited to energy generation, storage, planet temperature, element consumption, and clean water availability.[2,4–7] As such, many emerging technologies highlight efficiency as one of their most coveted properties, regarding both performance and resources required for development. However, the development of these new technologies is limited to the availability of materials with desired characteristics. In response, nanoscale material research has shown promise in producing novel materials with distinct thermal, optical, and electronic properties. Due to the unique physical interactions between small discrete objects and their environment, nano researchers are developing materials with radically different behaviors when compared to their "bulk-scale" counterparts.[8–12] In addition to these unique qualities, the very size of these nanomaterials presents unique applications, as there are few discrete bodies in the size regime between cellular and molecular scales such as biological markers with luminescent qualities or as metallic catalysts with morphologies of high surface area while using minimal amounts of reagent.[13,14]

The term “nanomaterial” usually defines a structure that can be measured within 1-100nm in any one direction and are often named based on their dimensionality.[15,16] Namely, a nanoparticle (NP), nanowire, and nanosheet may be described as zero, one and two dimensional, respectively. These materials may be metallic or organic in composition as well as many subcategories in-between. Furthermore, any given nanomaterial may be crystalline, amorphous, or polymer-based structures. A consequence of the wide range of nanomaterial types is that they lend themselves to a great deal of potential applications. For example, metallic nanorods may be the preferred structure for electron charge transfer compared to a quasi-spherical NP.[17,18] Meanwhile, organic nanospheres are viable as vehicles for drug delivery compared to metallic materials.[19]

Initial applications of nanomaterials date back to early in the Common Era, where nanocrystals (NCs) were used in colored glassmaking.[20] Famously, the Lycurgus cup of late Rome (4th Century) transmits red light due to its Au/Ag NC content.[20] The observed coloration is a result of plasmonic resonance, a phenomenon which occurs when the electron dipole of a given NP causes electromagnetic fields to occur at the particle surface, thereby resulting in unique light wave scattering not observed in the bulk.[21,22] As a result, gold – which appears yellow and lustrous in the bulk – is capable of scattering red or even blue light depending on its size. This same phenomenon is also seen in colloidal Au particles synthesized by Michael Faraday, who first postulated the size dependent nature of these optical properties in the mid-1800s.[23] We now describe this size dependence trend as quantum confinement: an effect which occurs as a material decreases in volume. As the available space where electrons can exist in a material decreases, the amount of energy required to excite an electron becomes both larger and more quantized as levels in the valence and conduction bands of a particle become more discrete.[24,25] This phenomenon is the underpinning principle of the novel traits in many nanomaterials derived from electronic behavior.

Nanoscale structures possess traits inherent to their size regime which lend themselves to applications based primarily on their morphology and size. For example, lipid nanoparticles are a series of structures composed of both waxy and coordinating lipids and can encapsulate products for efficient drug delivery.[26,27] Due to the size regime of lipid NPs, they are able to deliver targeted medication to cellular structures compared to a syringe which would be far too large. They can also protect the active molecule in the event it would be destroyed before arriving at its destination. Most notably, during the COVID-19 pandemic, mRNA vaccines were made viable by protecting negatively charged mRNA strands with positively charged ionizable lipids.[19,28] This facilitates the delivery of mRNA strands into cell membranes without the interference of destructive enzymes.[19,28] Further exploitation of the high surface area to volume ratio of nanoparticles involves catalytic applications where discrete bodies of charged surfaces are ideal. During Friedel-Crafts acylation, carbon shelled metals with positively charged surfaces can behave as Lewis acids, resulting in efficient catalysts compared to bulk metals.[14] Additionally, these nanoscale material sizes and morphologies are ideal for conditions where light scattering is desired. Vantablack is a super-black coating which absorbs +99.9% of visible light while retaining fairly uniform absorption from a wide viewing angle, as a consequence of the vertical carbon nanotube "forest" used to scatter light.[29,30] VANTA – vertically aligned nanotube arrays – are able to and absorb photons with unparalleled efficiency due to the high surface area available for photons to scatter off of.[29,30] This phenomenon is also responsible for why so many nanoparticle solutions appear black at high concentrations.

Further idiosyncrasies unique to materials in the nanoscale are their unusual electronic behavior, which is being applied to a swath of technologies. A prominent subject of materials research of late has been semiconductors, which are materials with properties that fall between

conductors – such as metals – and insulators like ceramics. They are often binary or ternary products but can also exist as pure elements like silicon. These products can be synthesized at diameters smaller than their own Bohr exciton radius, or the most probable distance an electron may be from an atom's nucleus in a NP.[24,25,31] Once in this size regime, the valence and conduction bands of the material begin to deviate from each other at smaller sizes. Consequently, increasingly greater energies are required excite an electron across the material's "band gap" into the conduction band. (Figure 1.1) The energy released from the following electron-hole recombination also changes with this change in band gap. The result is the ability to tune the diameters of these "quantum dot" (QD) NCs to change the energy emission during electron relaxation, and therefore the wavelengths of light emitted after excitation. Compared to metal NPs, these semiconductor QDs are particularly coveted due to their large Bohr exciton radii. Though metal NPs generally require diameters below 10 nm to behave as QDs, semiconductors demonstrate this same behavior at larger sizes.[32] This lends semiconductor NPs towards applications in optoelectronics, energy conversion, and biological tracers, and encourages the discovery of new nanomaterials with potentially novel traits. This dissertation focuses on synthesis of ternary semiconductor NPs which contain chalcogens.

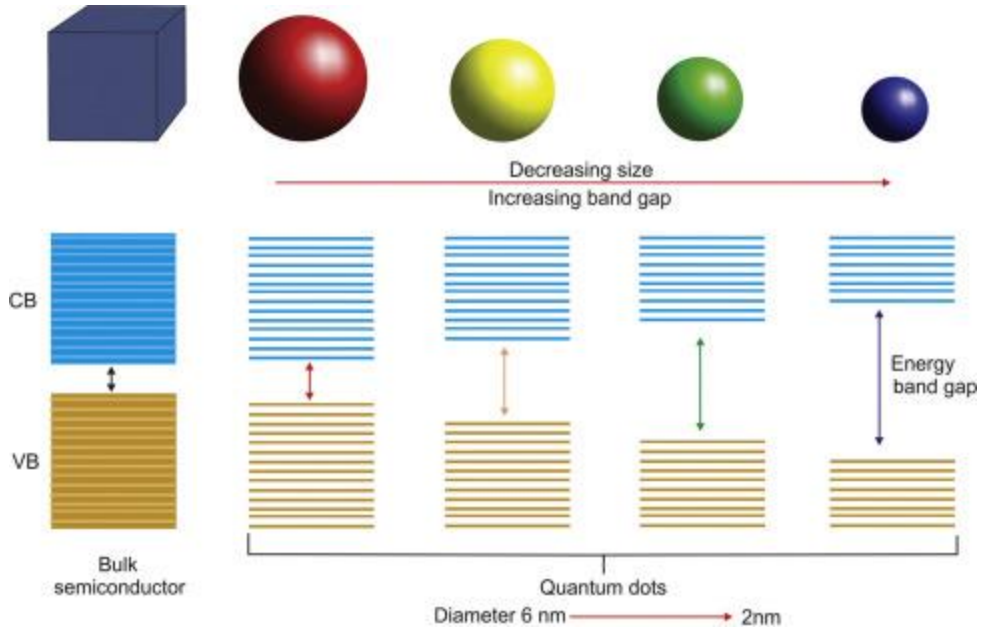

Figure 1.1 Demonstration of quantum confinement. As material volume decreases from bulk (cube) to the nano regime, energy states for electrons to occupy become more quantized and the magnitude of energy difference (band gap) increases.[33] Reprinted from Science Direct, Kumar D. S., Kumar B. J., Mahesh H. M., Quantum Nanostructures (QDs): An Overview, 59-88, Copyright 2018, with permission from Elsevier.

1.2 Research Motivation

NP research has experienced rapid growth since the late 20th Century due to advancements in synthetic and characterization techniques. Many nanosystems have been developed with highly tunable morphologies, atomic arrangements (often described as "phase"), and size distributions. Despite these advancements, the field has yet to elucidate on the finer details which dominate general synthetic trends. While other synthetic fields such as organic chemistry have thousands of mechanisms and synthetic routes to acquire their desired products, NP synthesis is comparatively viewed as a "black box," where the tunable parameters extrapolated in one system may not be applicable to another.[34,35] In response, The Macdonald lab at Vanderbilt University studies the fundamental trends of NP reactions in an effort to expand the synthetic toolkit of the field.

NP synthesis is generally categorized as top-down or bottom-up approaches, where either a bulk material is broken down into nanoscale structures, or atoms are assembled as monomers into larger structures.[20] The generally accepted bottom-up nucleation model was proposed by Victor LaMer, when he observed a concentration dependence of nucleation as monomers became increasingly available to react.[36,37] In a typical solvothermal synthesis, reagent is broken down into reactive monomers using reducing agents, coordinating ligands, and/or high reaction temperatures. As the concentration of these monomers rises, they reach a point where they begin to nucleate into particles – dubbed the "nucleation step" – and will begin to grow by taking on additional monomers. This is favorable as increasing the size of a discrete body reduces its surface energy, thereby making the NP more stable. Once the initial particles begin to form and grow, new NPs will continue to nucleate until the concentration of monomers drops below the saturation level where nucleation began. Beyond this point, remaining monomers will continue to coalesce with existing nanoparticles in what is referred to as the "growth step." Under ideal circumstances, the reaction conditions will permit a rapid rise in monomer formation, resulting in a short nucleation event. Rapid nucleation steps are preferred as they typically produce more monodisperse NPs with minimal size distributions, as very little growth is experienced between nucleation of the first and last nanoparticles. Although recent literature indicates that this model is not applicable in some size focusing syntheses, LaMer's model is still the popular rule of thumb used to model bottom-up NP reactions.[38]

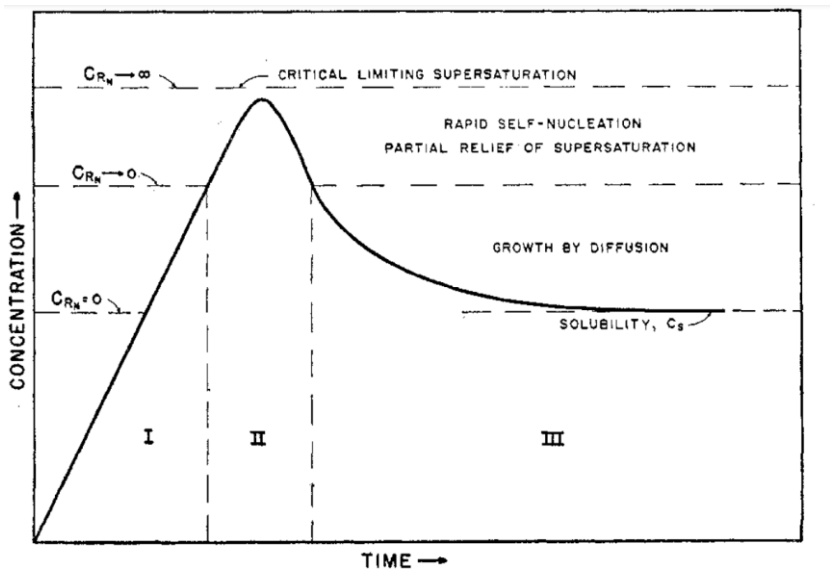

Figure 1.2: LaMer burst nucleation. Monomer formation occurs in region I as precursor reagent decomposes into substituent building blocks. As concentration rises, a critical point occurs at region II, where nucleation initially occurs – a consequence of the solution becoming supersaturated – immediately followed by growth. As monomer is consumed, concentration falls to below supersaturation, nucleation events cease and only growth continues.[36] Reprinted with permission from Ind. Eng. Chem. 1952, 44, 6, 1270–1277. Copyright 1952 American Chemical Society.

In addition to nucleation and growth control, popular features to control during NP synthesis are morphology – overall particle shape – and crystal phase, periodic arrangement of atoms within the crystal. With respect to the latter, there are two major schools of thought focused on obtaining phase pure products. When using a thermodynamic approach to phase control, the surface chemistry of the NP and its ligands is the main priority.[39–42] The coordinating ligands present will often possess different binding strengths or charges, which can modulate where on a nanoparticle surface a ligand will target. In the case of CdSe, it has been observed that anionic ligands result in a cubic crystal phase, while cationic ones synthesize hexagonal products.[39–41] One explanation for this is that anionic ligands prefer to target sides of the crystal (planes or facets) with high cationic concentrations, meaning that a cubic phase with four cationic surfaces would be the ideal product compared to a hexagonal phase which only has one.[39] This facet targeting can also manipulate NC morphology, as preferential binding to specific regions on crystal surface

leaves room for growth in areas where there is minimal ligand coordination.[43] For example, a ligand environment which targets a NC's surface on two opposing sides may result in a disk morphology as monomers are more able to grow onto the facets without ligand coordination. Therefore, ligand choice relative to the material being made is often critical in the production of specific crystal phases and morphologies.

The alternative approach to the thermodynamic argument on phase control is kinetics. The kinetic argument was first proposed by Wilhelm Ostwald, where he postulated that when different atomic arrangements of a material – referred to as polytypes – are possible, the less stable of the two forms first.[44] In practice, this means that when two crystal phases are potential products, nucleation of a crystal at any size results in the phase that is energetically unfavored to exist, which we refer to as the metastable phase. Strouse and Tilley take this one step further and go on to propose that as a crystal grows, the presence of defects like stacking faults and atomic vacancies become so numerous, that this precarious phase will rearrange into the energetically favored phase.[45] Washington *et al*. demonstrated this by synthesizing metastable CdSe NCs over 14nm in diameter; far larger than previously reported.[45] By slowing down decomposition of the precursors, Washington was able to mitigate the presence of crystal lattice defects due to the hindered growth step, thus resulting in large, defect-free metastable product. In this way, the kinetic approach can be viewed as building a house of cards, where meticulous assembly of the building blocks improves one's odds of building a large structure, and absence of these blocks will result in a change in their orientation.

A recent departure from the aforementioned bottom-up approaches has been ion exchange (IE), a post-synthetic process which focuses on preserving the existing structure of a crystal and

replacing some or all of its constituents with free ions in solution.[46] In nano synthesis, this process typically involves dispersing NC hosts in solution with a solvated reagent as a source of ions. Due to thermodynamic factors – such as association and dissociation tendencies of reagents in solution – an IE may proceed spontaneously.[47] Since the energy required to break the bonds of a NC lattice is often related to structure stability a given exchange may prove spontaneous if the product NC has a higher lattice energy of the host NC. In this instance, the association energy of the product is higher than the dissociation energy of the host. In the event an exchange is energetically unfavorable, the addition of energy in the form of heat may be sufficient to drive the reaction. This method has the added benefit of potentially raising ion mobility through solids, further encouraging diffusion of ions through a lattice. Particularly, copper is known to become extremely mobile in crystal lattices at temperatures as low as ~100 °C making it a model element in NC cation exchange reactions whether it is being introduced or removed from the lattice.[48,49]

Further considerations when designing an IE experiment are how the solvent's molecular environment stabilizes nanoparticle surfaces and ions in solution. In the same way that an anion sublattice may favor association with one cation over another, ligands will preferentially coordinate with specific ions, allowing metal precursor to be brought into solution prior to IE. Furthermore, these same molecules can coordinate with and remove ions from a host NC assuming they have a high affinity for bonding with said ions. For example, phoshine ligands – being soft bases – tend to have a high affinity for soft cations, making them suitable for removing lead or silver from a host NC.[50] This outward diffusion would then allow for solvated ions to fill vacancies forming in the crystal lattice. Similarly, the same results may be achievable by introducing chelating molecules to target host ions for removal. This is shown in Chapter 2, where neocuproine was used to remove copper cations from a Cu_2S NC prior to incorporation of iron.[51] Furthermore,

this effect can be observed with solvent-ion interactions, as has been demonstrated with ethanol, methanol, and hexanes.[52] As such, all molecular reagents present in solution should be considered carefully when designing IE experiments.

While ion exchange has been an established synthetic technique in the nanoscale[53–55], colloidal applications only became relevant less than 2 decades ago, with the Alivisatos group demonstrating fully reversible cation exchange of CdSe to Ag_2Se.[56] Here, Son *et al*. observed complete cation exchange under ambient conditions in only minutes. Additionally, the morphology of the product NCs were variable depending on host particle size, with thinner nanorods forming nanospheres and thicker rods retaining their host's morphology. This irregularity has often been attributed to reaction zone size, where smaller particles experience less equilibrium across the particle throughout the exchange and therefore undergo a change in morphology to a more thermodynamically favored shape. However, larger particle surfaces possess propagated reaction zones, thus allowing for equilibrium to be achieved in the particle more quickly, thereby preserving particle morphology.[56]

Despite these changes in particle shape, Son *et al*. noted that the anion sublattice remained relatively consistent under variable reaction conditions.[56] This trend has remained one of the hallmarks of IE and been exploited to yield products of specific crystal phases which would otherwise be difficult to synthesize. Of note are the isolation of metastable transition metal chalcogenides. Early reports of this include the synthesis of metastable CdSe and Cu_2S via cation exchange of rock salt PbSe and wurtzite CdS, respectively.[57,58] In later studies, it was found that cation exchange reactions have the potential to preserve both the cation and anion sublattice orientation, allowing the Schaak group to synthesize metastable CoS and MnS from hexagonal $Cu_{2-x}S$ with retention of the hexagonal phase and platelet morphology of the host NC.[59,60] This was

particularly significant because in addition to reporting on previously unobserved cation sublattice retention, the Schaak group made use of 3d transition metals not typically utilized in these reactions, thus further emphasizing the potential for cation exchange in synthesizing NCs of unusual phases and composition.[60]

Although IE reactions can preserve a host particle's lattice, they are not a foolproof synthetic technique. While crystal phase of the host can often be retained in the product, more strenuous reactions can reduce this likelihood. Hernández-Pagán *et al*. demonstrated a phase conversion of hexagonal $Cu_{2-x}S$ to cubic Au_2S during cation exchange.[61] This has been attributed both to expansion of the lattice due to the large ionic radii of gold relative to copper as well as lattice plane shifts throughout the exchange.[61] Further risks are presented when introducing molecular driving forces, as coordination to undesired atoms in solution or formation of excessive vacancies lower the chance that the counterion sublattice will be retained. This was again shown during the conversion of hexagonal Cu_2S to cubic $CuFeS_2$ (explained in detail in Chapter 2). Above all else, temperature remains one of the biggest risks to phase preservation during ion exchange. As observed during exchange of cubic SnS to hexagonal $Cu_{1.8}S$, greatly increasing ion mobility may have unintended consequences on diffusion rates. Due to the increased mobility causing tin to vacate the lattice faster than the entering copper ions, both the NC phase and morphology were altered despite many stable cubic copper sulfides being known to exist (explained in detail in Chapter 3). Unsurprisingly, ion exchange can yield unpredictable polytypes when reaction conditions are too aggressive to allow for counter-ion sublattice retention.

1.3 Scope of Dissertation

This thesis concerns the synthesis of copper chalcogen nanocrystals through cation exchange with focus on ternary intermediate and final products. In Chapter 2, synthetic targeting of metastable and thermodynamic $CuFeS_2$ from Cu_2S hosts is demonstrated where electron donor strength dictates whether the wurtzite or tetragonal phase forms. In Chapter 3, high surface area $Cu_{1.8}S$ Roxbyite nanocubes are synthesized from a cubic SnS with copper-tin-sulfide intermediate shell structures. In Chapter 4, preliminary work on an auric ion exchange with Cu_2Se towards an unresolved copper gold selenide product is discussed with focus on synthetic techniques and limitations on characterization. This appears to be the first time this metastable structure has been observed.

Chapter 2

TOLMAN'S ELECTRONIC PARAMETER OF THE LIGAND PREDICTS PHASE IN THE CATION EXCHANGE TO $CuFeS_2$ NANOPARTICLES

2.1 Abstract

The metastable and thermodynamically favored phases of $CuFeS_2$ are shown to be alternatively synthesized during partial cation exchange of hexagonal Cu_2S using various phosphorus-containing ligands. Transmission electron microscopy and energy dispersive X-ray spectroscopy (EDS) mapping confirm the retention of the particle morphology and the approximate $CuFeS_2$ stoichiometry. Powder X-ray diffraction patterns and refinements indicate that the resulting phase mixtures of metastable wurtzite-like $CuFeS_2$ versus tetragonal chalcopyrite are correlated with the Tolman electronic parameter of the tertiary phosphorus-based ligand used during the cation exchange. Strong L-type donors lead to the chalcopyrite phase and weak donors to the wurtzite-like phase. To our knowledge, this is the first demonstration of phase control in nanoparticle synthesis using solely L-type donors.

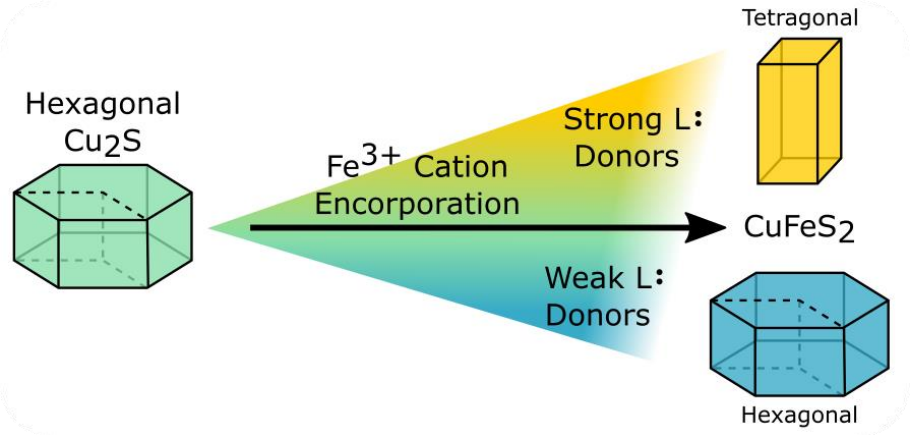

2.2 Introduction

Crystallographic polytypes give opportunities for diversification of material properties without changing composition. In nanomaterials, the cubic/hexagonal polytypism was first exemplified with the II−VI semiconductors such as CdSe and CdS in which both polytypes were both known as bulk materials.[62–64] In more recent years, nanocrystal synthesis has led to the discovery of novel crystal phases in other materials where previously only one of the hexagonal or cubic phases were known in the bulk.[60,65–71] Ternary I−III−VI_2 semiconductor nanocrystals are potential less-toxic replacements of cadmium and lead chalcogenide nanocrystals. Their diversity of composition allows for tunability of their band gaps and other physical properties. Furthermore, when cation poor, these semiconductors often possess surface plasmon resonances centered in the NIR portion of the spectrum. Many of the I−III−VI_2 semiconductors have chalcopyrite (CP) thermodynamic phases, that is, crystal structures based on a doubled unit cell of cubic zinc blende to accommodate ordering of the two cations. However, metastable wurtzite-like (WZ-like) analogous polytypes, not known in the bulk, have also been prepared in colloidal nanocrystal (NC) preparations. Examples include $CuInS_2$, $CuInSe_2$, and $CuGaO_2$.[65–71] These new polytypes present a further field of diversity of semiconductor properties, including an inherent asymmetry built into a hexagonal crystal structure, in which the crystallographic c-direction is chemically and electronically unique to the a- and b-directions.

Our research group strives to understand why unusual metastable products form in nanocrystal syntheses, not only to achieve reproducibility but also to provide the synthetic framework to facilitate the syntheses of other novel crystallographic phases through bottom-up synthesis. Here we add to this body of work, exploring the phase-controlled synthesis of $CuFeS_2$ and present a novel wurtzite-like (WZ-like) phase. A hexagonal analogue of $CuFeS_2$ is particularly

interesting, because as an inherently anisotropic material it may have present advantages in thermoelectric, photocatalytic, and electrochemical applications over the already promising chalcopyrite phase.[72,73] Here we also illustrate how ligand environment influences the phase in partial cation exchange processes to metastable phases. Here, "partial" is used to denote that not all of the Cu is removed from the particles in the reaction rather than to imply an incomplete reaction to the product $CuFeS_2$ phases.

It has been observed previously that ligand choice in colloidal syntheses is imperative to polytype control.[42,74,75] In the case of well-studied CdSe, ligand choice has been shown to change the rate of the reaction, preventing or creating stacking faults and other defects during crystal growth that can catalyze transformations between metastable and thermodynamic polytypes.[45] It has also been observed that strong anionic X-type ligands, such as phosphonate and oleate, stabilize cubic CdSe with its four, equivalent, cation-rich [111] facets. The hexagonal wurtzite phase has only one cation-rich [200] facet and so is preferred under conditions dominated by neutral L-type donors such as amines.[75]

In the phase control of I−III−VI semiconductor nanocrystals, ligands have been shown to also control phase but through a differing mechanism. The role of ligands, such as 1-dodecanethiol, is to influence the formation of phase-directing intermediate nanocrystals.[76] In this case, the 1-dodecanethiol plays a special role as a reagent at high temperatures, becoming a sulfur source. Under these conditions, hexagonal Cu_2S forms as an intermediate and becomes a cation exchange host to WZ-like Cu−III−S_2 products.[77,78] Similarly, Brutchey showed that the phase control of nanocrystals of WZ-like $CuInSe_2$ forms though specific copper selenide intermediates.[70,79]

The conservation of the structure of the anionic sublattice has been an underpinning feature of cation exchange in general and is now a well-established route to metastable phases of

nanomaterials.[80,81] It is important to note that the phase control of the second cation-exchange step to ternary materials has been previously thought to be relatively independent of the ligand environment. In contrast, here we show that the phase of $CuFeS_2$ product resultant of cation exchange is not independent of ligand environment even at room temperature. From the same hexagonal Cu_2S starting point, the WZ-like/CP phase composition of the product has a linear relationship with the Tolman Electronic Parameter (TEP) of added phosphines and phosphites. Strongly donating phosphines lead to the thermodynamic chalcopyrite phase, and weakly donating phosphines allow for the maintenance of the hexagonal anion lattice and the formation of the metastable wurtzite-like $CuFeS_2$ phase (Figure 2.1). In comparison to the use of ligands to influence the phase of CdSe, here all the phosphine ligands are strictly L-type.[72,73,82] This brings into question the hypothesis that anionic X-type ligands are needed to stabilize many charged facets to influence structural transformations to cubic and cubic-like phases.

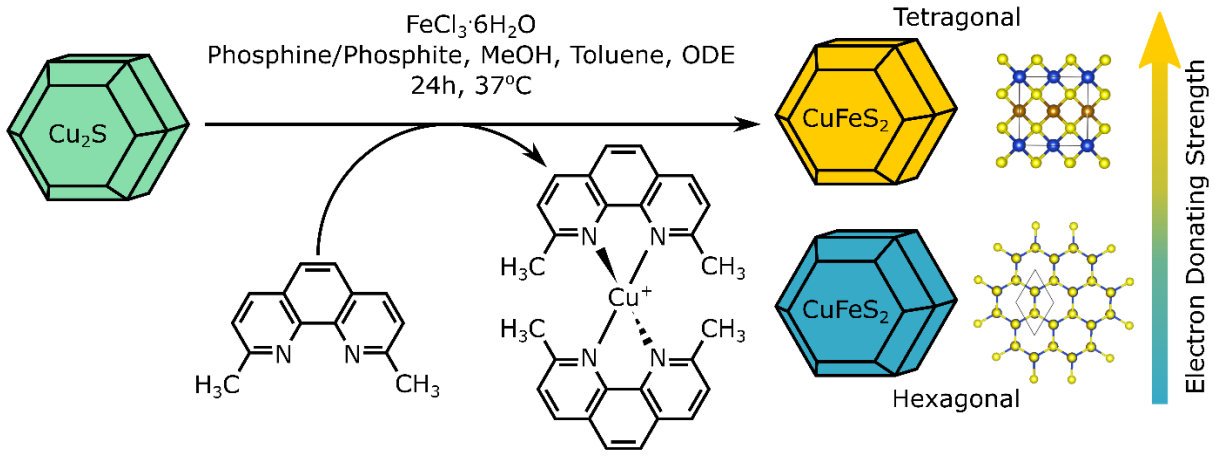

Figure 2.1. Schematic of the synthesis used to exchange Cu_2S into tetragonal and WZ-like $CuFeS_2$ particles. Reprinted with permission from Nano Lett. 2020, 20, 12, 8556–8562. Copyright 2020 American Chemical Society.

Among I–III–VI_2 semiconductors, $CuFeS_2$ has been studied extensively in its thermodynamically favored tetragonal phase. Chalcopyrite (CP) has seen application in solar cells, lithiumion batteries, and thermoelectrics.[72,83] Metastable $CuFeS_2$ may offer a greater degree of

electronic control due to the propagation of electron flow in anisotropic directions commonly seen in hexagonal rather than cubic structures.[84–86] The three reported syntheses of metastable $CuFeS_2$ have focused on kinetic approaches by manipulating nucleation temperatures and reaction temperature ramp rates.[72,73,82] Rather than a one-pot synthesis, here we employ a partial cation exchange (CE) of hexagonal Cu_2S to produce WZ-like $CuFeS_2$ in a method analogous to those performed for $CuInS_2$.[77,87,88] The two-step method provides opportunity for detailed study of the mechanisms of phase control.

2.3 Results and Discussion

Cu_2S seed particles were prepared through a literature procedure by heating $Cu(acac)_2$ in 1-dodecanethiol. The resulting Cu_2S nanocrystals (13.96 ± 0.83 nm, n = 200) had the low chalcocite crystal structure (Figure 2.2) with a pseudo hexagonal anion sublattice. These nanocrystals were the host materials for cation exchange to $CuFeS_2$. The method of utilizing the Cu_2S seed anion sublattice to template the metastable hexagonal crystal phase in the product allows for a wide variety of products of the ternary material with regard to size and morphology. Cu_2S nanocrystals in the literature include spheres ranging from 2 to 20 nm spheres as well as rods.[84,89–91]

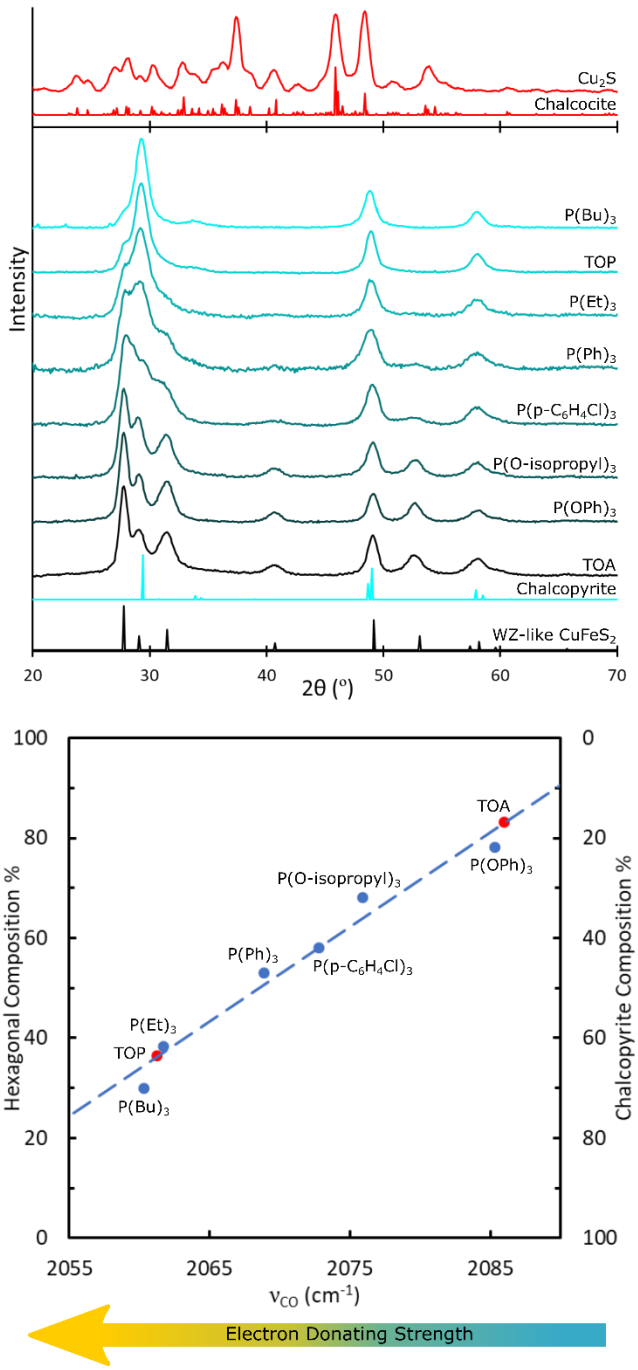

Figure 2.2. PXRD of $CuFeS_2$ products exchanged in the presence of varying phosphorus-based ligands. The resulting products had their percent phase composition analyzed using Rietveld refinements and the resulting compositions graphed in relation to the electron donating tendencies of the coordinating ligand as measured by Tolman et al.[92] Reprinted with permission from Nano Lett. 2020, 20, 12, 8556–8562. Copyright 2020 American Chemical Society.

The synthesis of $CuFeS_2$ was performed by stirring a toluene solution of host Cu_2S nanocrystals with $FeCl_3$ dissolved in MeOH based on the synthesis reported by Alice Leach.[93] Neocuproine was added to help drive the cation exchange forward, as it is known as a very strong, selective chelator for Cu(I).[94–96] Under the conditions reported in the SI, the cation exchange required stirring overnight. As an aside, halving the concentration of all components increased the reaction time to several days, up to a week. As a last component, amines, phosphines, or phosphites were added as surface stabilizing ligands (Figure 2.1) which unexpectedly were instrumental in controlling the phase of the $CuFeS_2$ product.

All products were characterized with powder X-ray diffraction (pXRD) (Figure 2.2a). When strongly donating phosphines such as tributyl phosphine were employed, the resultant nanoparticles showed the thermodynamic chalcopyrite phase of $CuFeS_2$. In the presence of the weakest donating phosphine, triphenyl phosphite, the product nanoparticles produced a diffraction pattern similar to wurtzite-like polytypes, such as $CuInS_2$ or $(Cu(i)P)S_2$, and was consistent with the few patterns reported for a WZ-like phase of $CuFeS_2$ NC.[72,73,82,97,98] (Figure 2.2) The pattern was refined to a WZ unit cell with dimensions of a = 3.70 Å, c = 6.12 Å with an hcp-packed sulfur lattice and 50% occupancy of the tetrahedral holes by an equal ratio of Cu and Fe cations. This unit cell was chosen for simplicity despite the likelihood that the structure supports a lower symmetry and cation ordering, or even several types of cation ordering as has been seen in aberration corrected STEM for WZ-like $CuInS_2$ nanocrystals.[65]

Phosphorus ligands with intermediate electron donating abilities produced a mixture of phases. Resulting phase compositions were determined using Rietveld refinement (Figures A.1, A.2) and found to agree well with varying percent compositions of wurtzite-like and tetragonal patterns. The percent composition was plotted against the TEP of the ligand, which gives a

quantifiable measure of electronic donation based on CO stretching frequencies of $NiL(CO)_3$ complexes, where L is a phosphine/phosphite ligand.[92] Low CO stretching frequencies are indicative of a strongly donating ligand. A clear linear correlation between the electron donation strength and the % chalcopyrite was observed (Figure 2.2b).

This linear relationship between TEP and product phase composition allowed for high phase tunability of the product. Additionally, this trend allows us to qualitatively compare the electronic donation properties of phosphite and phosphorus ligands with low steric bulk that were never tested by Tolman. For example, trioctylphosphine produces a percent composition of $CuFeS_2$ phase intermediate to $P(Et)_3$ and $P(Bu)_3$ and so a TEP of ∼2061 cm^{-1} can be extrapolated.

In all cases, TEM of the $CuFeS_2$ particles indicated that they retained the spherelike morphology of the Cu_2S host but shrunk significantly. A lattice volume contraction of ∼23% is to be expected based on the unit cells of chalcocite, WZ-like, and CP $CuFeS_2$ phases which equates to a reduction of diameter by 8.5%. Upon cation exchange from Cu_2S to $CuFeS_2$, a larger decrease in particle diameter of 14−36% was observed with the particles prepared in the presence of strongly donating phosphines being the smallest. It can be concluded that in addition to the lattice contraction the strong phosphines are etching the Cu_2S precursor, similar to that observed by the Robinson group.[99] Cation exchange of seed particles that were only 10 nm (∼25% smaller) did not cause a noticeable difference in the resultant phase ratio. Size effects on phase control can be excluded as an explanation from this system.

Quantitative EDS indicated that the cation composition of the particles was close to stoichiometric 1:1 Cu/Fe (Figure 2.3). It was noted that in the presence of the strongest donating phosphines, the particles were cation-rich with a stoichiometry of $Cu_{1.0}Fe_{1.0}S_{1.6}$. This is consistent with the observations of the Robinson group that phosphines preferentially etch the sulfur of

copper(I) sulfides. In the presence of weakly donating triphenylphosphite, the sulfur content remained high with resultant composition of $Cu_{1.1}Fe_{1.0}S_{2.1}$.

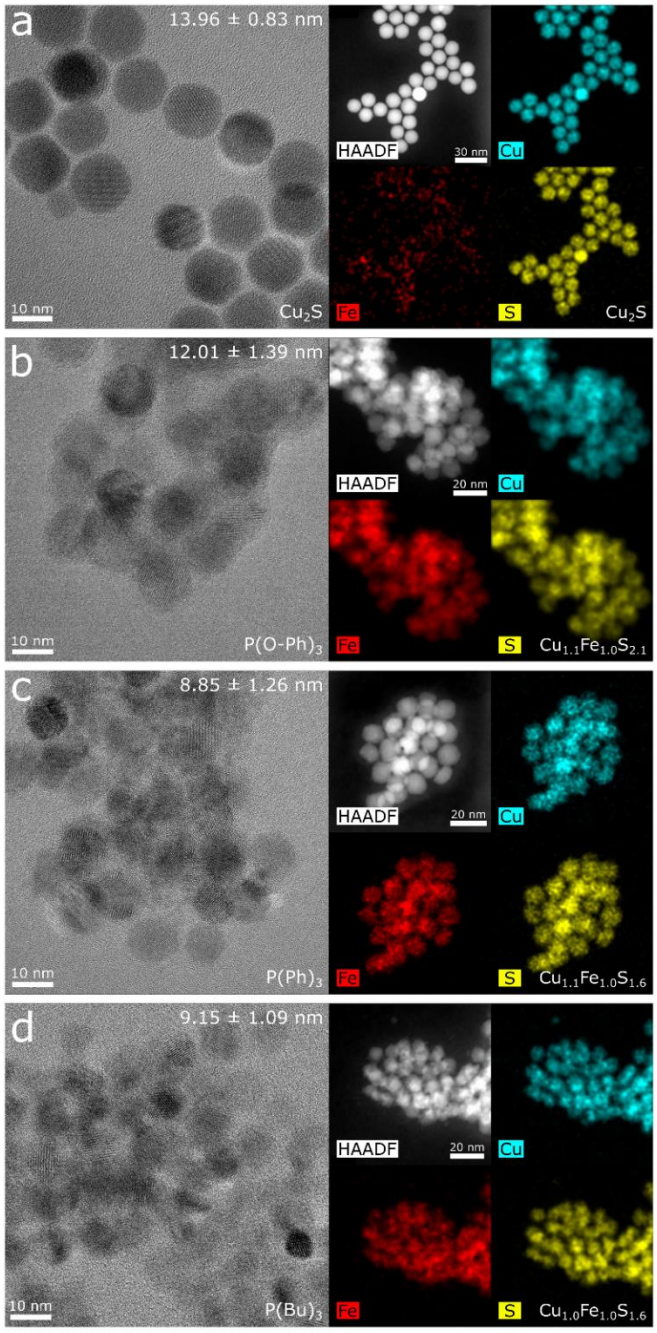

Figure 2.3. TEM and TEM-EDS images acquired of $CuFeS_2$ at either phase extreme of (a) WZ-like, (b) mixed phase, and (c) tetragonal products. EDS shows the cation rich product as $CuFeS_2$ becomes less WZ-like as the phosphorus ligands become more electron donating. Reprinted with permission from Nano Lett. 2020, 20, 12, 8556–8562. Copyright 2020 American Chemical Society.

HR-TEM of the product nanoparticles demonstrated that the WZ-like $CuFeS_2$ particles were single crystalline, as is expected from cation exchange with a retained anion sublattice. However, the CP particles were polycrystalline, indicating a major anion reorganization and recrystallization into the FCC stacking of sulfur anions occurs from several points in each nanoparticle (Figure 2.4).

At first pass, the observed trend that strongly donating ligands prefer the tetragonal phases seems to agree with the existing phase control literature on CdSe quantum dots. Huang et al. observed that strong anionic ligands favored the four cationic [111] surfaces of zincblende CdSe NCs, directing the phase in syntheses to the cubic phase.[75] Indeed, our observations on stoichiometry seem to agree; the CP $CuFeS_2$ particles formed are cation rich, perhaps suggesting cation-rich surfaces, whereas the WZ particles are stoichiometric. What is most curious is that the existing literature observations with CdSe indicate that the ZB directing ligands must be X-type and the WZ directors must be L-type. Instead, here both directing ligands are L-type. Such a discrepancy with the prevailing logic requires further investigation.

Existing literature has emphasized the role of ligands stabilizing specific ion rich facets in different crystal phases, which has been used to selectively produce cubic and hexagonal phases both during and in post synthetic steps.[41,42,74–76] Mahler, Lequeux, and Dubertret et al. noticed that heating preformed ZB-CdSe NCs at 200 °C in excess Ltype oleylamine could induce a phase transition to WZ.[74] Similar annealing experiments by Talapin et al. in high purity L-type TOPO showed transformations of ZB CdSe to the WZ phase.[75] As a counterpoint, when heating WZ CdSe the addition of X-type alkyl phosphonates promoted the partial transformation of WZ NCs to ZB.[75]

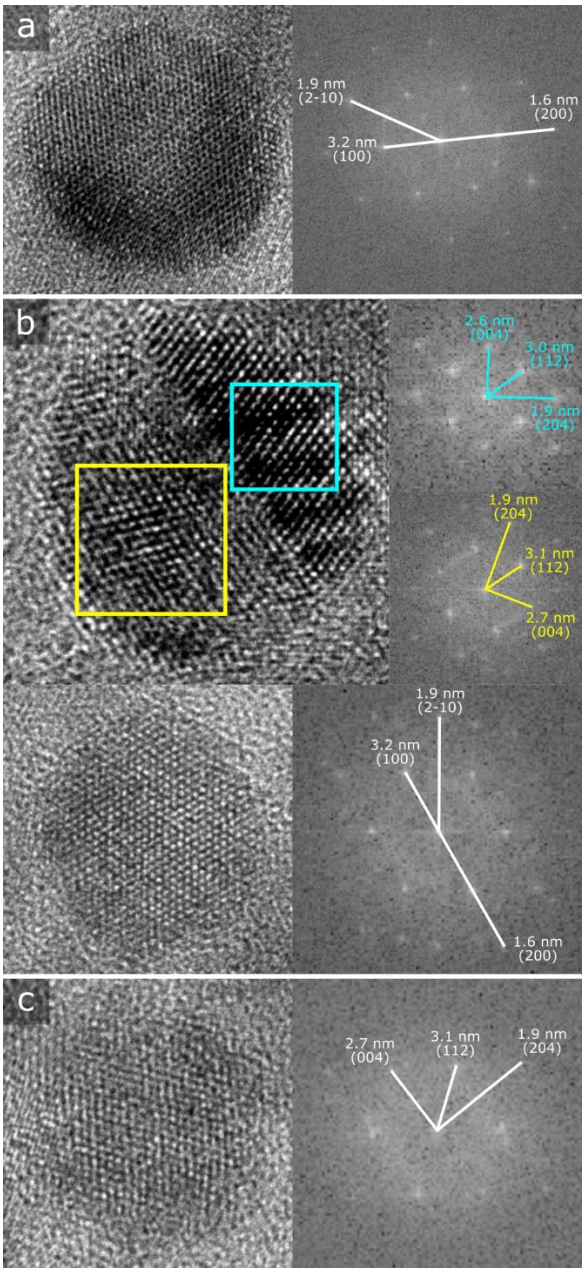

Figure 2.4. HRTEM of and FFT of particles of (a) WZ-like phase obtained in the presence of weakly donating triphenylphosphite and (b) both phases obtained in the presence of intermediate donating triphenylphosphine. Particles that exhibited the CP phase were polycrystalline (top) yet those that showed the WZ-like phase were single crystalline (bottom). Mixed-phase particles were not readily observed. (c) Chalcopyrite was produced in the presence of strongly donating trioctylphosphine (TOP). Reprinted with permission from Nano Lett. 2020, 20, 12, 8556–8562. Copyright 2020 American Chemical Society.

To test if $CuFeS_2$ polytypism is sensitive to similar particle surface stabilization as CdSe nanocrystals, we examined if phase can be tuned postsynthetically. Both WZ-like and mixed phase $CuFeS_2$ samples were stirred in the presence of excess strongly donating PBu_3 to see if

postsynthetic phase conversion was possible. Under synthetic conditions, the transformation of the anion lattice from WZ-like to cubic to yield the CP phase occurs in the presence of PBu_3 but under these postsynthetic conditions the resulting products did not indicate any change in phase composition by pXRD (Figure 2.5). A substantial activation energy between the WZ-like and CP phases must therefore exist, and more importantly the event of cation exchange is critical to the phase control of this reaction.

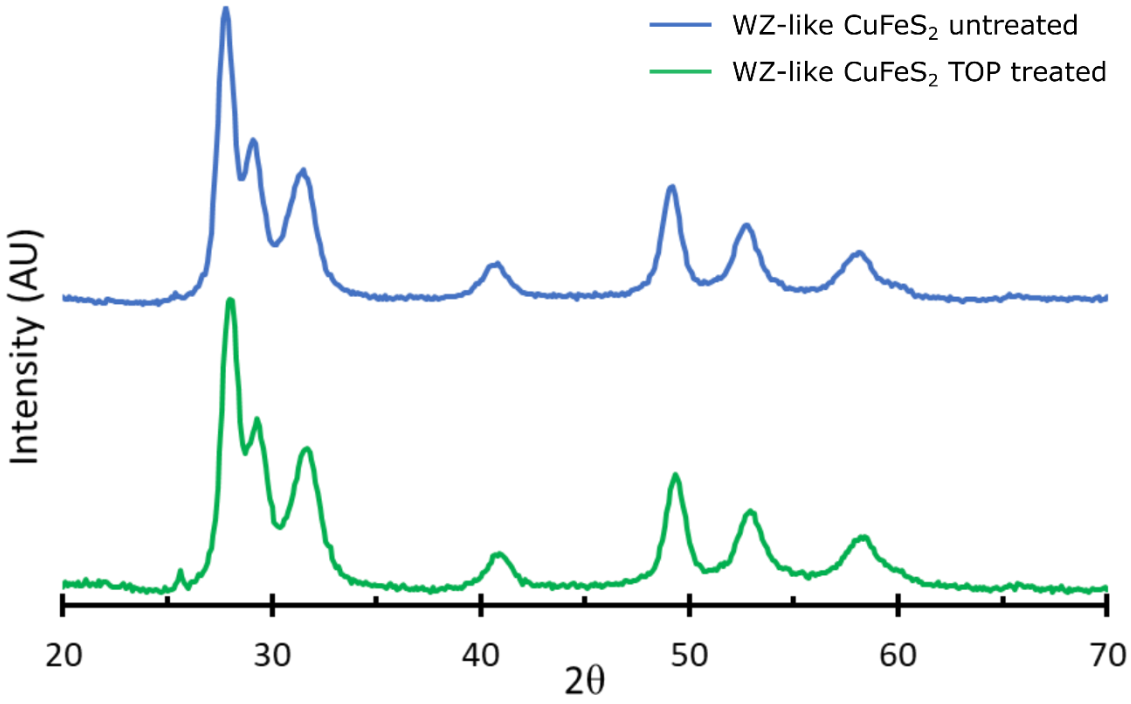

Figure 2.5. Blue) pXRD of WZ-like $CuFeS_2$ synthesized in the presence of weakly donating triphenylphosphite. Green) The product was then stirred at 80°C overnight in anhydrous toluene and strongly donating tributylphosphine, to determine if post synthetic phase transition from metastable WZ-like to the thermodynamic CP phase was possible. There did not appear to be any significant change in the product phase, unlike what has been shown with CdSe zincblende and WZ cores.[74] Reprinted with permission from Nano Lett. 2020, 20, 12, 8556–8562. Copyright 2020 American Chemical Society.

Further attempts at postsynthetic phase conversion were performed using a high-temperature pXRD furnace to further rule out thermal interconversion between the phases. Metastable WZ-like $CuInS_2$ will convert to the thermodynamically stable CP phase between 400

and 500 °C, whereas the metastable WZ Cu_2Se phase transforms to the cubic at only 150 °C.[67,100] WZ-like $CuFeS_2$ nanocrystals that were synthesized through cation exchange in the presence of amine ligands were heated to 500 °C. pXRD patterns were taken at room temperature and every 100° starting at 100 °C (Figure 2.6). Thermal stability of the WZ $CuFeS_2$ to 300 °C was observed, whereupon it oxidized. This temperature is similar to the oxidation of chapcolyrite ores, but the oxide products were different.[101] Such temperature stability and high activation energy for phase transformation between the metastable WZ and CP phases further indicate that the event of cation exchange is crucial to phase control.

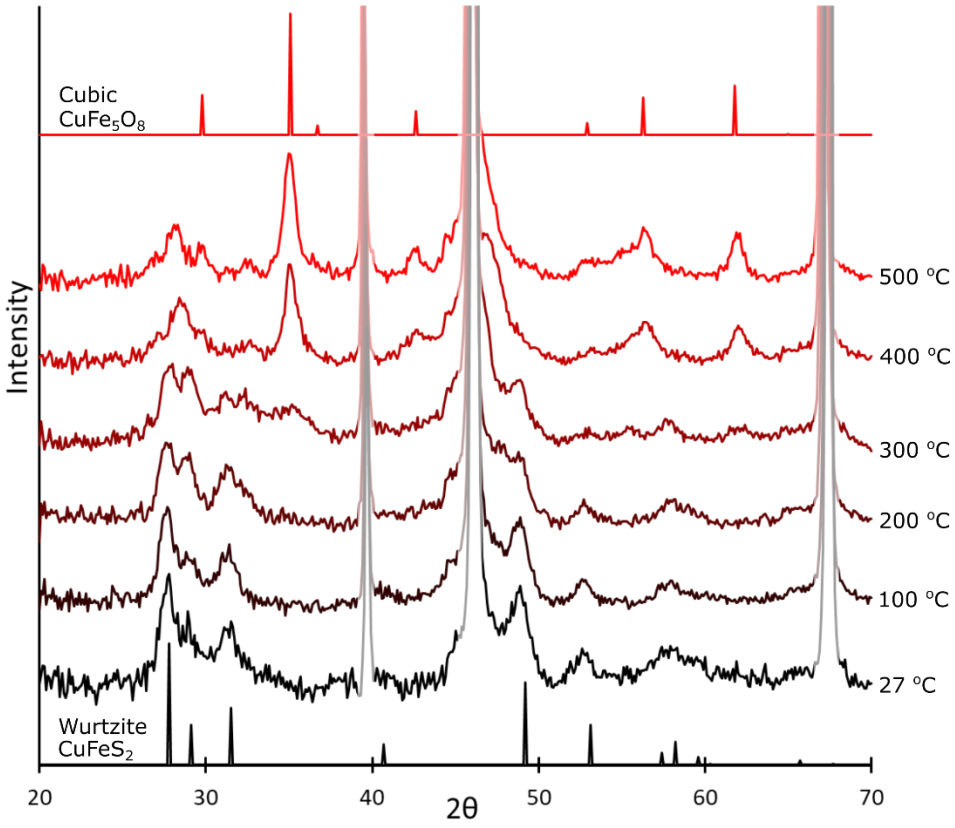

Figure 2.6. Temperature-dependent pXRD of WZ-like $CuFeS_2$ NCs. Reflections by the platinum sample holder signals at approximately 39, 47, and 67° 2θ have been faded. Reprinted with permission from Nano Lett. 2020, 20, 12, 8556–8562. Copyright 2020 American Chemical Society.

An alternative hypothesis to a dominating role of particle surface stabilization is that the differing strength of the phosphines influences the relative reactions rates in the cation exchange. Poorly matched rates cause a high density of defects that can catalyze a phase transformation. In the cation exchange to $CuFeS_2$, there is both the rate at which Cu^+ is removed from the lattice and the rate in which Fe^{3+} in incorporated. In the presence of weakly donating phosphines, $FeCl_3$ methanol solutions displayed only the charge transfer bands and yellow color of typical $FeCl_3$ solutions that are d^5 high-spin with no spin-allowed transitions. However, in the presence of a strongly donating phosphine, such as Bu_3P, the solution turned a deep purple suggesting formation of a iron tricloride-phosphine adduct with charge-transfer transitions.[102,103] The strong coordination of the ferric ions by the strongly donating phosphines slows their incorporation into the crystal lattice compared to the rate at which Cu^+ is extracted and coordinated by neocuproine. This imbalance in rates causes a transient high concentration of cation vacancy defects that catalyzes the product to convert to its more energetically favored phase, CP. This mechanism would conform with the kinetic arguments proposed originally by Ostwald and since used to grow large nanoparticles in metastable phases by selecting synthetic conditions that prevent the formation of defects that catalyzed the phase transiton.[44,45] A corollary observation has been made by Steimle et al. who noticed that phosphines can induce lattice sulfur vacancies that catalyze the transformation of $Cu_{1.8}S$ digenite (fcc-like sulfur lattice) to Cu_2S chalcocite (hcp-like sulfur lattice) prior to cation exchange to ZnS. Here, under the same phosphines the opposite transformation of the anion lattice is observed in the cation exchange to $CuFeS_2$.[104]

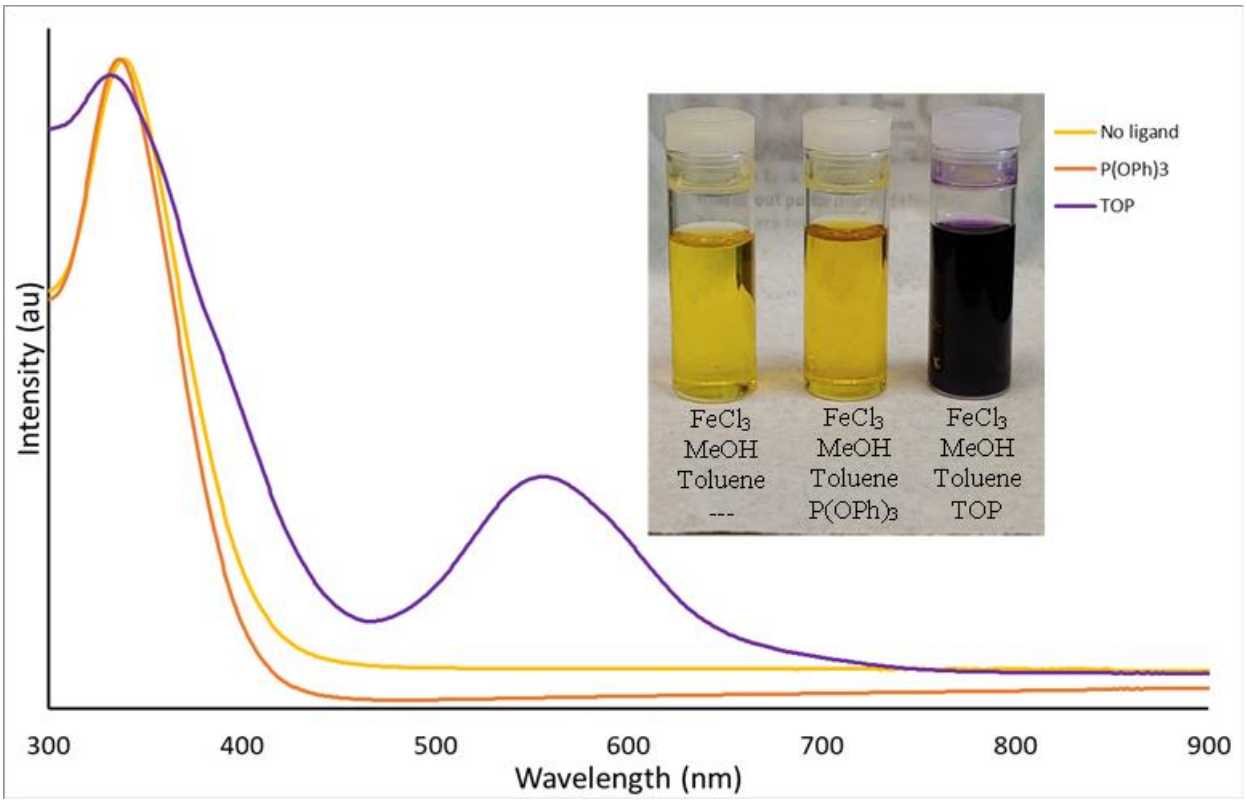

Figure 2.7. Solutions of ferric chloride in methanol/toluene with no ligand, weak donating ligand (triphenylphosphite) and a strong donating ligand (trioctylphosphine) present in solution. The strong change in color indicates a strong interaction of the ligand with ferric ions in solution prior to cation exchange. Reprinted with permission from Nano Lett. 2020, 20, 12, 8556–8562. Copyright 2020 American Chemical Society.

A test of this kinetic hypothesis is to examine closely the samples that exhibited both WZ-like and CP phases under intermediate phosphine strength. In a thermodynamically controlled process where surface energies are minimized by those presented by the CP phase, individual particles might be expected to exhibit both CP and WZ phases in some sort of equilibrium with clean, low-energy, epitaxial interfaces.[63,105] However, if the conversion process is event driven and kinetically determined, one would expect that individual particles express either WZ or CP phase but not both; under these intermediate conditions, not all particles experience the event that catalyzes the transformation from hexagonal to cubic. In the particles observed by HR-TEM, it was noted that these samples contained particles that were entirely WZ-like phase or particles that were polycrystalline CP with many faults. Particles exhibiting both phases were not readily

observed. (Figure A.3) Therefore, the HR-TEM further supports a kinetic interpretation of the phase control. The individual particles can be thought of as their own reactors. The observations of mixed-phase products containing individual all-WZ and all-CP particles suggest a stochastic formation of catalyzing vacancies across the myriad of particles.

Lowering the transient concentration of vacancies prevents the phase conversion to CP. Besides changing the identity of the iron-binding phosphine, increasing the availability of free Fe^{3+} by lowering the phosphine concentration should also increase the amount of WZ-like product. Indeed, when the concentration of intermediate binding PPh_3 was lowered from 8.5 equiv to 1 equiv (to iron), the product diffraction pattern resembled what would be expected if the weaker donating $P(p\text{-}C_6H_4Cl)_3$ was used instead. (Figure 2.8

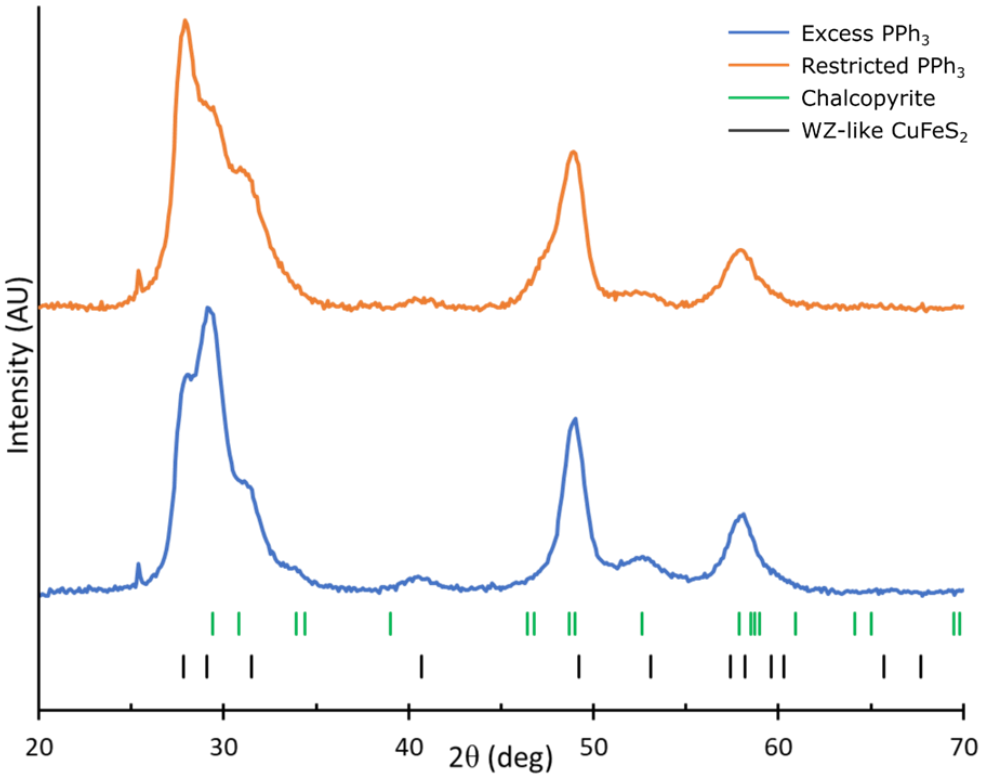

Figure 2.8. Blue) pXRD of $CuFeS_2$ synthesized in the presence of excess triphenylphosphine. Orange) Product was then synthesized using stochiometric amounts of triphenylphosphine to ferric ions in solution to determine if the kinetic impact of the phosphine ligand is significant enough to select product phases based on their ability to interact in solution. If the reaction is reliant on kinetics, less phosphorus ligand present will permit ferric ions to more freely enter the Cu^+ vacancies and retain a WZ-like phase, rather than forcing a conversion to the thermodynamic. As expected, product formed in the presence of minimal triphenylphosphine produced a diffraction pattern similar to tris-4-chlorophenylphosphine, a less electron donating ligand containing more WZ-like product. It should be noted that pattern refinement was not able to be performed on the ligand limited sample, due to additional signal present causing inconsistent matches to WZ-like and chalcopyrite reference patterns. These extra signals, such as the shoulder present at ~47 2θ (deg), appear to be various copper sulfides such as djurleite, digenite, etc. Reprinted with permission from Nano Lett. 2020, 20, 12, 8556–8562. Copyright 2020 American Chemical Society.

2.4 Conclusion

Here presented is the phase-controlled synthesis of $CuFeS_2$ through partial cation exchange from Cu_2S. Weakly donating ligand environments during cation exchange were found to favor the metastable WZ-like phase, retaining the hexagonal anion sublattice of the host Cu_2S. Strong donor environments gave the thermodynamic CP phase. Phase composition of the product has a linear relationship with the ligand Tolman Electronic Parameter.

To our knowledge, this is the first instance of phase control using L-type ligands of the same coordinating head, which is in contrast to previous phase-control work with CdSe where X- versus L-type ligands were needed to influence phase between cubic and hexagonal structures. The previous work suggests a thermodynamic stabilization of ligand surfaces influences phase. Here, the effect is kinetic. We hypothesize the ligands affect the rates of exchange of the two cations. Transient defects when the rates are imbalanced catalyze the transformation of the anion sublattice to the thermodynamic CP phase. Once formed, the metastable WZ-$CuFeS_2$ was thermally stable and upon heating oxidized between 300 and 400 °C rather than converting to the CP phase.

These experiments demonstrate that the process of cation exchange and partial cation exchange can be highly destabilizing to the anion sublattice, and that the ligand environment can be chosen carefully, even within one ligand class, to stabilize the process. The mechanisms of how ligands influence phase in direct syntheses to binary materials are not the same as those in cation exchange processes. The experiments will help the further synthesis of novel metastable materials, especially ternary semiconductors through cation exchange processes, with prospects in thermoelectric generators and other electrochemical applications.

2.5 Experimental Methods

Materials. Copper(II) acetylacetonate ($Cu(acac)_2$, 98+%), triphenylphosphine ($P(Ph)_3$, 99%), and triphenyl phosphite ($P(OPh)_3$, 97%) were obtained from Strem. Triethyl phosphine ($P(Et)_3$, 97%) was obtained from Alfa Aesar. Ferric chloride hexahydrate ($FeCl_3 \cdot 6H_2O$, 97-102%) was obtained from Fischer Scientific Education. Tris(4-chlorophenyl)phosphine ($P(p\text{-}C_6H_4Cl)_3$, 97%) was

obtained from Ark Pharm. Dioctyl ether (DOE, 99%), dodecanethiol (DDT, ≥98%), neocuproine hydrate (99%), trioctylamine (TOA, 98%), tributylphosphine (TBP, 97%), anhydrous trioctylphosphine (TOP, 90%), triisopropyl phosphite ($P(O\text{-isopropyl})_3$, 95%), chloroform, isopropanol, toluene, and methanol were purchased from Sigma-Aldrich. Wet solvents were degassed and dried over sieves before storing in a N_2 glovebox for use in cation exchange reactions. High temperature reactions were performed on Schlenk lines.

Hexagonal Cu_2S Host Particles. Hexagonal phase Cu_2S hosts were synthesized following the method reported by Kuzuya.[76] In brief, 2 mmol of $Cu(acac)_2$ was added to 1 mL of DOE and 9 mL of 1-dodecanethiol in a three-neck flask with condenser and degassed at 85°C for 30 minutes. The solution was then placed under N_2 and the temperature was raised to 215°C whereupon the reaction was stirred for 1 hr. The solution of NCs was then air cooled to ~100°C, followed by an injection of 2 mL of room temperature toluene. Isopropanol was added and the particles precipitated by centrifugation at 4400 rpm for 10 minutes. The supernatant was decanted. Twice more, the particles were suspended in chloroform and precipitated using isopropanol and centrifugation. The purified Cu_2S NCs were then dispersed in 10 mL of chloroform before storing inside a glovebox under N_2. A 10 uL aliquot of this solution was dissolved in a 10 mL volumetric flask with a mixture of 1:1 chloroform:methanol and 50 mg neocuproine for 6 h. A 1 mL aliquot was then serial diluted to 5 mL before addition to a cuvette. The visible absorbance at 460 nm was measured and compared to a calibration curve of Cu(I) neocuproine.[94] The concentration of the stock solution was calculated to be 0.279 mmol Cu(I)/mL. The particles were characterized by TEM, EDS, and powder XRD.

$CuFeS_2$ via Partial Cation Exchange. The cation exchange reactions were performed in an air free environment using an adaptation of the method reported by Leach et al.[93] Typically, three solutions of Cu_2S NCs (0.096 mmol of Cu) in chloroform, 2.5 mL of 20 mM $FeCl_3 \cdot 6H_2O$ in methanol, and 4.8 mL of 40 mM neocuproine hydrate in toluene were stirred together with 0.43 mmol of a ligand (TOA, TOP, TBP, etc.). The resulting mixture was diluted to ~12.3 mL with a 1:2 mixture of toluene:ODE. The solution was then stirred overnight at ambient glove box temperatures (37°C). The resulting particles were separated from the solvent, byproducts and unreacted precursors through precipitation with isopropyl alcohol followed by centrifugation at 8700 RPM for 5 minutes. After decanting the supernatant, the resulting pellet of NCs was dispersed in toluene and precipitated again with methanol prior to further centrifugation, twice. The purified NCs were then dispersed in toluene.

Instrumentation. Optical spectroscopy data was obtained using a Jasco V-670 Spectrophotometer and 10 mm path length quartz cuvettes. Transmission electron microscopy (TEM) was acquired using a FEI Tecnai Osiris TEM operated at 200 keV. For particle sizes, 200 NC were measured for each sample. Powder x-ray diffraction (pXRD) was performed on a Rigaku SmartLab powder X-ray diffractometer with a CuKα ($\lambda = 0.15418$ nm) radiation source set to 40 kV and 44 mA, and a D/teX Ultra 250 1D silicon strip detector. pXRD patterns were acquired with a step size of 0.1° at 1° 2θ/min. High temperature pXRD patterns were performed using a Rigaku Multipurpose High Temperature Attachment and a PTC-EVO temperature controller, with a ramp rate of 10°C/min and a holding time of 5 minutes. The furnace temperature was measured using an R type thermocouple with an accuracy of ± 1.5°C.

Chapter 3

CRACKING SHELLS AND SCRAMBLING EGGS: INTERMEDIATE SHELL FORMATION AND ANION REARRANGEMENT IN THE CATION EXCHANGE FROM π-SnS TO $Cu_{1.8}S$

3.1 Abstract

Cation exchange is used to achieve products of complex morphology, phase, or elemental compositions from host particles with similar features. Understanding which parameters are responsible for preserving or altering these features is key to predicting novel cation exchange products. Here we demonstrate cation exchange of cubic π-SnS to pseudohexagonal roxbyite ($Cu_{1.8}S$) as confirmed by powder X-ray diffraction, transmission electron microscopy, and energy dispersion spectroscopy mapping. TEM/EDS shows the initial formation of a shell of amorphous Cu-Sn-S. It is only upon elevated temperatures that the shells are breached on one facet and complete cation exchange to a copper sulfide core occurs. Mismatched diffusion rates between the outgoing Sn^{2+} and the incoming Cu^{+} cause the formation of voids in the cation exchanged nanocuboids, a documented result of the Kirkendall effect. These mismatched rates are implicated in the change of the sulfide lattice from pseudo-fcc to pseudo-hcp. The prepared nanocrystals were studied as photoabsorbers in quantum dot sensitized solar cells (QDSSCs), and it was found that the shelling of the π-SnS with the amorphous Sn-Cu-S does not greatly change the cell characteristics or performance, indicating that the voltage limiting defect in π-SnS solar cell designs is in the core, not the surface of the material.

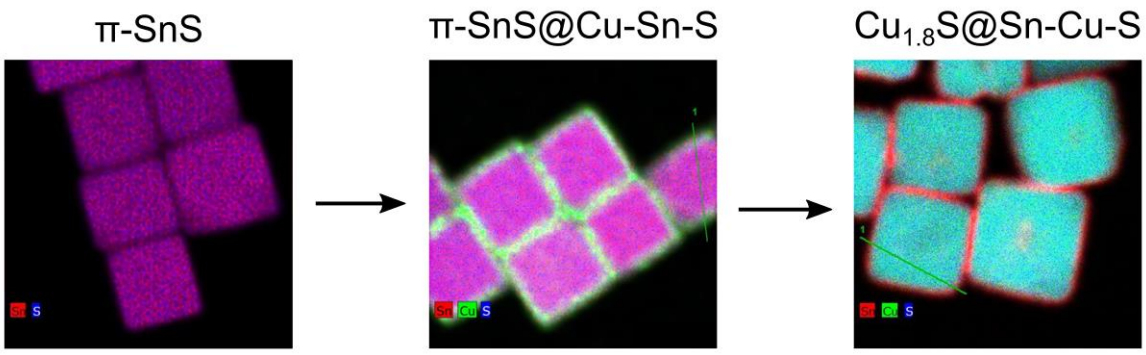

3.2 Introduction

Polytypism in crystal systems has been shown to alter the properties of materials without a change in their elemental composition.[46,80] Of note are the II−VI semiconductors, which are well studied in their known thermodynamic and metastable phases, such as the wurtzite/zinc blende polytypism of CdS and CdSe quantum dots which offer differing optoelectronic properties based on crystal structure.[62–64,74] Similar cubic/ hexagonal polytypism has been seen in unexpected places, where only one phase is known in the bulk.[51,60,69,70] The extreme kinetic trapping afforded by nanoscale synthesis and the large surface energies capture and stabilize these metastable phases.[44,45] Recent synthetic efforts have explored the tunability of nanoscale materials and the conditions necessary to achieve specific product phases to gain further control over material properties, especially in crystalline materials with complicated phase spaces.[41,42,51,61]

In addition to several compositionally different phases, the I−VI semiconductors show cubic/hexagonal polytypism in their I_2−VI compositions, some of which are already seen in mineral phases. Notable examples include the silver and copper chalcogenides which each possess several different phases of differing stoichiometry and where cubic/hexagonal polytypism further diversifies their resulting properties and potential applications.[106,107] Nanomaterials of these

semiconductors possess potential applications in thermo- and optoelectronic applications while often being comprised of abundant and environmentally friendly precursor reagents.[108,109] The copper chalcogenides have been of particular interest, due to the ion mobility of copper, lending products to a wide number of stoichiometries, each with their own unique properties.[60] This ion mobility has been further explored post-synthetically, with copper seeing use as either leaving or entering the body during cation exchange.[60,61,110,111]

These principles of ion mobility have seen popular use as a route toward nonstandard phases through cation exchange and, less commonly, anion exchange.[112,113] The ability to remove and replace ions with varying stochiometric ratios while leaving the counterions undisturbed has led to a wide variety of novel material syntheses.[114–116] Of particular note are uncommon hexagonal phases which have been sought due to the unique traits which stem from anisotropic crystal lattices. The Schaak group has demonstrated this using numerous different cations toward similarly arranged wurtzite products stemming from hexagonally packed roxbyite $Cu_{1.8}S$ as host particles.[60]

Retention of the anion sublattice structure in cation exchange is oft touted as an underpinning principle of cation exchange, and the sublattice of the host material can be a predictor of the phase of the products.[81] Exceptions where the anion sublattice is not retained can occur. Strongly unfavorable thermodynamics of the product affect anion retention. Examples include the cation exchange of Cu_2S to bcc Au_2S and also the exchange of hexagonal Cu_2S to rock salt PbS, for which there is no known hexagonal phase.[61,94]

Where polytypism is possible, ligands are usually implicated as a phase directing agent. Ligands have a complex relationship with phase control, and three different mechanisms have been identified. Ligands can manipulate the exchange kinetics of the cations. An unbalanced flow of cations in and out of the host lattice can cause collapse of the thermodynamic phase of the product.

An example was the manipulation of copper ion availability through phosphine- and amine-binding ligands to alter exchange kinetics, which allowed for a gradient between two phases to be achieved during cation exchange of Cu_2S to $CuFeS_2$.[51] Ligands can also remove anions from the host material, changing the phase of the host in situ, as was seen recently in the exchange from cubic $Cu_{1.8}S$ to ZnS. Trioctylphospine removed sulfur from the lattice of the copper sulfide to create a tetragonal Cu_2S intermediate.[104] Lastly, alteration of host thermodynamics using surface stabilizing ligands to change the ion lattice phase during and postsynthesis is a well-established process.[74,75]

Our research seeks to understand the synthetic parameters necessary for nanomaterial phase control and stability with the aim of further expanding the existing library of products not found in the bulk scale. Here we add to this knowledge with the cation exchange to copper sulfide from cubic phase π-SnS nanocrystals (Figure 3.1). Copper sulfide is chosen because there several known pseudohexagonal and pseudocubic phases. While exchange from hexagonal phases such as wurtzite CdS to hexagonal phase $Cu_{2-x}S$ is established, cation exchange from cubic phases is underexplored. Interestingly, the copper sulfide product here, from a cubic phase π-SnS, is pseudohexagonal roxbyite ($Cu_{1.8}S$), which is peculiar due to there being the established body of literature emphasizing sublattice preservation as the key parameter in controlling the product phase in cation exchange reactions.

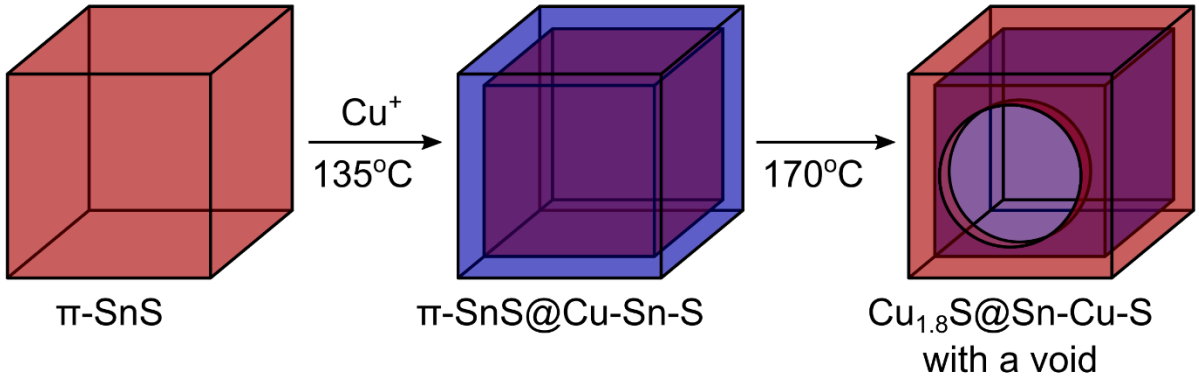

Figure 3.1. Schematic representation of the cation exchange process. Reprinted with permission from Chem. Mater. 2021, 33, 8, 3011–3019. Copyright 2021 American Chemical Society.

Through careful characterization and experiments that seek reaction intermediates, an intermediate product with an amorphous shell of Cu-Sn-S is identified as an important factor in the kinetics of the cation exchange, not the ligands.

Since π-SnS is a relatively new crystalline phase that is identified as a potentially revolutionary solar cell absorber material in tandem cell designs, we took the opportunity to study how the shell formation affects performance in the quantum dot sensitized solar cell designs.[117–119] The results suggest that the defects or semiconductor characteristics that are limiting the open circuit current of cells made with π-SnS are not located on the surface of the material.

3.3 Results and Discussion

π-SnS nanocuboids were synthesized following a modified literature method reported by Patra et al.[120] A solution of thiourea and hexadecylamine (HDA) was injected into a solution of tin(II) chloride and tributylphosphine (TBP) in HDA at 175 °C. After an initial temperature drop, the solution was held at 155 °C for 20 minutes. An aliquot of π-SnS nanocuboids was taken for characterization. Powder X-ray diffraction (XRD) confirmed the predominant presence of cubic π-SnS with an orthorhombic α-SnS (JCPDS no. 39- 0354) side product (Figure 3.2).[121,122] Both

phases can be described as distorted rock salt structures with the sulfide anions in distorted fcc arrangements. While the distortions from ideal octahedral cation coordination in α-SnS are uniaxial and lead to sheet- and plate-like structures, the distortions in πSnS happen in all directions, leading to an overall noncentrosymmetric, pseudocubic structure with a large unit cell of 64 atoms. High resolution TEM confirmed a single crystalline product with a cuboid shape (Figure 3.3, edge length = 52 ± 5 nm, n = 120, Figure B.1).

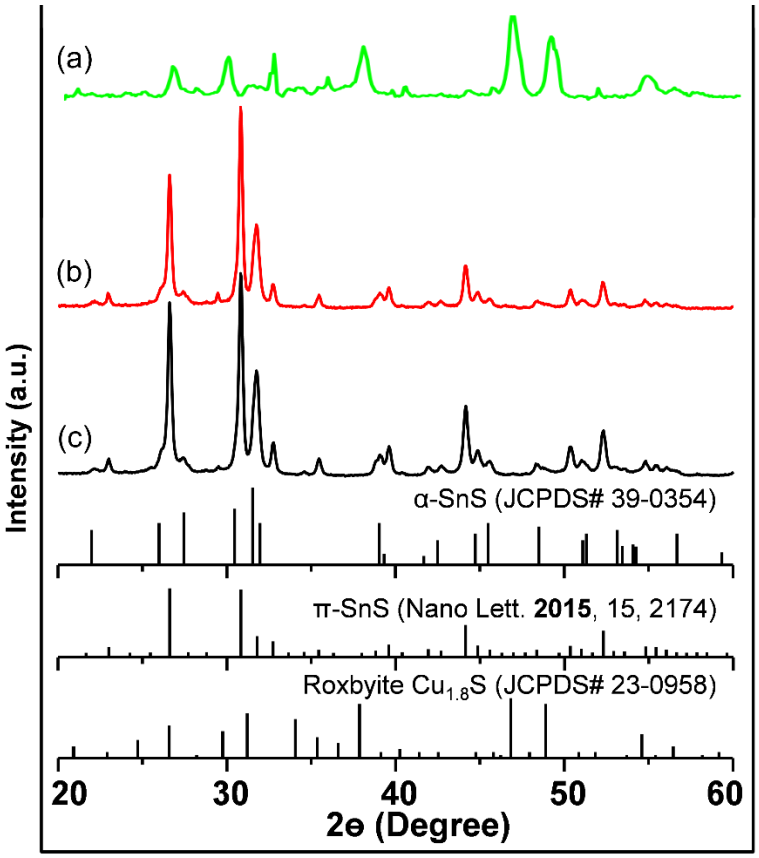

Figure 3.2. XRD at the different stages of the cation exchange reaction. (a), (b), and (c) are the XRD for $Cu_{1.8}S$@Sn-Cu-S, SnS@Cu-Sn-S, and pristine SnS, respectively. Reprinted with permission from Chem. Mater. 2021, 33, 8, 3011–3019. Copyright 2021 American Chemical Society.

The cation exchange – developed by Suresh Sarkar – was performed without purification of the SnS nanocuboids. The reaction solution was reduced to 90 °C prior to an air-free injection

of CuCl solubilized in oleylamine. The temperature was then ramped to 170 °C. Aliquots were collected at several temperatures to observe the exchange processes (Figure 3.2).

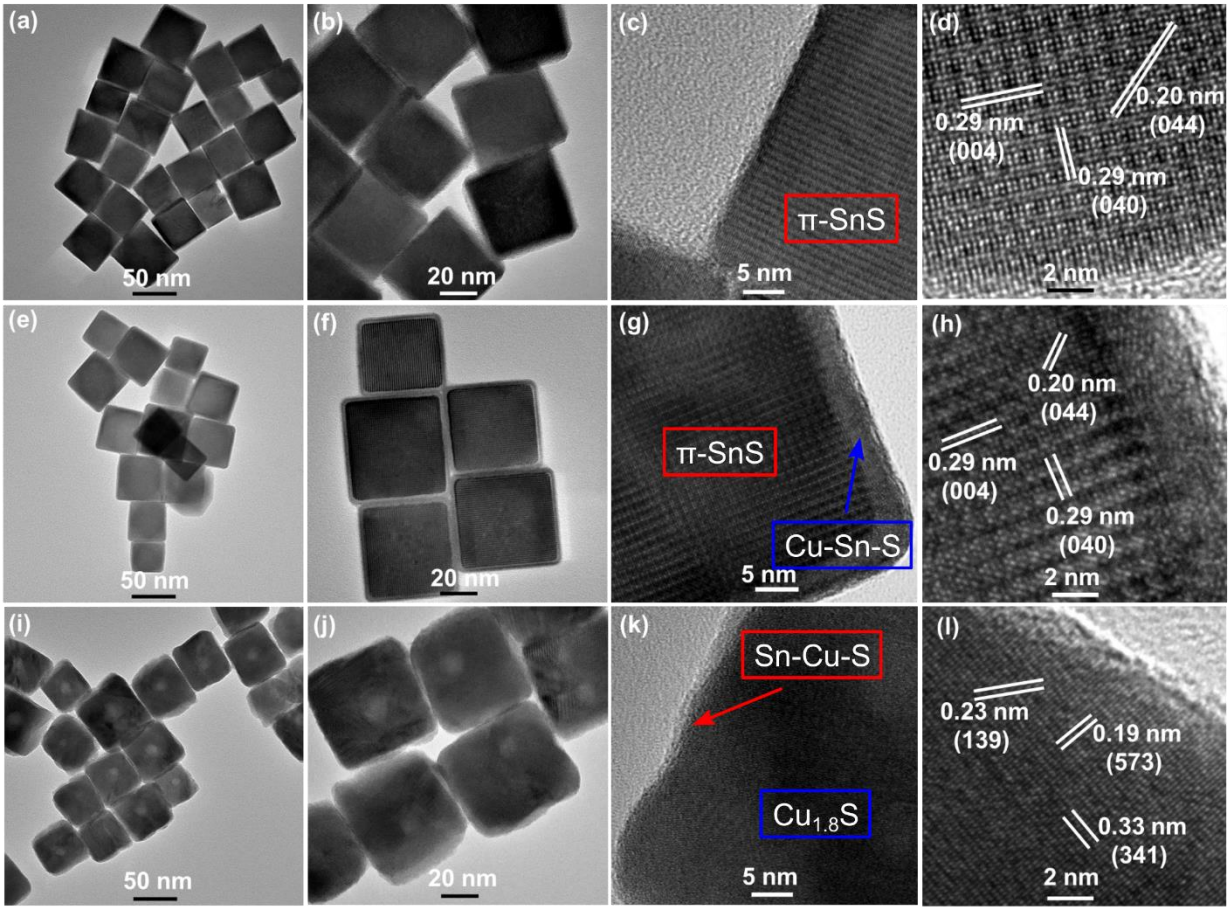

Figure 3.3. TEM and HR-TEM images of SnS nanocuboids (a−d), SnS@Cu-Sn-S nanocuboids collected at 135 °C (e−h), and $Cu_{1.8}S$@Sn-Cu-S nanocuboids collected at 175 °C (i−l). Reprinted with permission from Chem. Mater. 2021, 33, 8, 3011–3019. Copyright 2021 American Chemical Society.

TEM analysis of aliquots collected after the copper injection at 135 °C (52 ± 5 nm, n = 120) show similar morphology and size to the original SnS nanocuboids (Figure 3.3). HR-TEM shows that a 4 nm amorphous shell has developed (Figure 3.3). Energy dispersive X-ray spectroscopy (EDS) mapping and line scans across the cuboid indicate the particles possess a tin sulfide core with a copper rich copper−tin−sulfide shell (Figure 3.4), herein designated as core@shell π-SnS@Cu-Sn-S. XRD did not show additional reflections due to the shells, further

supporting its amorphous nature. HR-XPS suggests that the chemical environments of the atoms of the shell are close to that of the known crystalline phase $Cu^{1+}{}_3Sn^{4+}S_4$ (Figure B.3).[123] While there are several known ternary copper tin sulfide phases, we saw no evidence of a crystalline phase here.

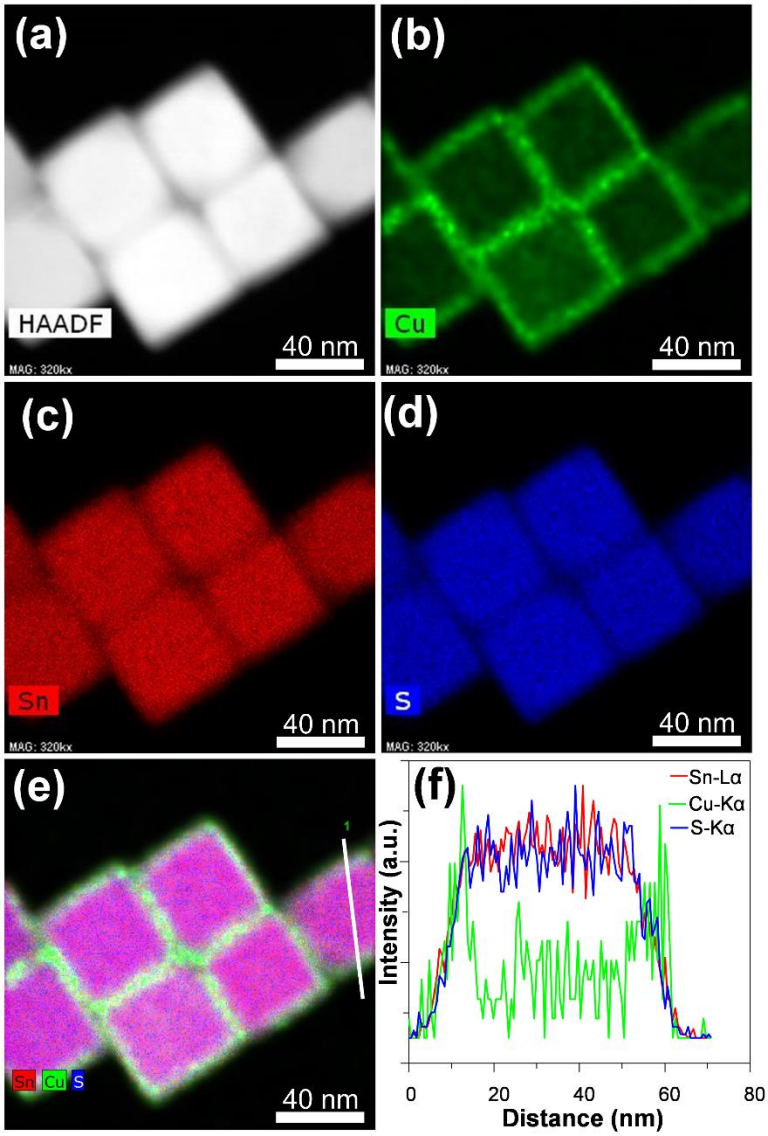

Figure 3.4. (a) High-angle annular dark field−scanning transmission electron microcopy (HAADF-STEM) image of the nanocuboids collected at 135 °C, (b−e) EDS elemental mapping, and (f) relative EDS signals of Sn, Cu, and S along the line noted in (e). Reprinted with permission from Chem. Mater. 2021, 33, 8, 3011–3019. Copyright 2021 American Chemical Society.

This first stage of cation exchange to π-SnS@Cu-Sn-S is diffusion limited and self-limiting. This conclusion is drawn because, even under extended heating at 135 °C or high copper concentrations, the shell was not any thicker. This step is also highly favored as even the addition of excess coordinating phosphine did not slow the reactivity of Cu^{+} toward the particle surface. Similar observations of core@shell nanostructures with various morphologies due to the cation exchange process (with product phase shell and pristine lattice core) have been reported.[124–127]

It was only after increasing the temperature to 170 °C that extensive cation exchange of the core of the π-SnS@Cu-Sn-S was observed. EDS mapping and a line scan across the cuboids confirmed a copper sulfide core and a remaining tin-rich, tin− copper−sulfide shell (Figure 3.5), designated herein as $Cu_{1.8}S$@ Sn-Cu-S.

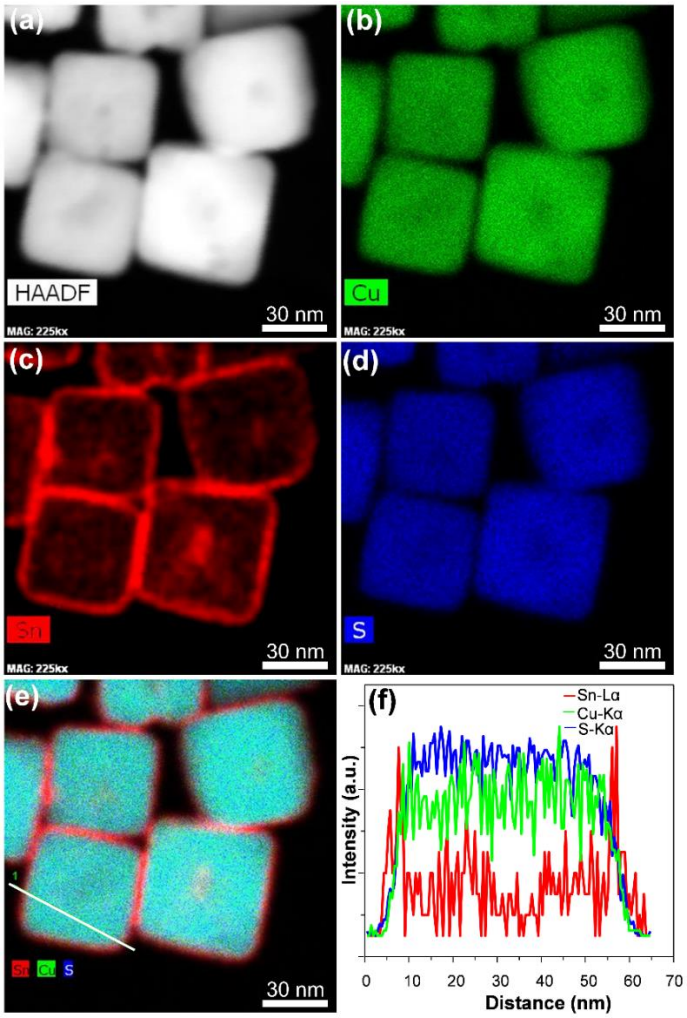

Figure 3.5. (a) HAADF-STEM image of the nanocuboids collected at 170 °C, (b−e) EDS elemental mapping, and (f) relative EDS signals of Sn, Cu, and S along the line noted in (e). Reprinted with permission from Chem. Mater. 2021, 33, 8, 3011–3019. Copyright 2021 American Chemical Society.

XRD of the product of the full cation exchange shows additional reflections at 37.7°, 46.5°, and 48.9° characteristic of a hexagonal-like copper(I) sulfide and was assigned to roxbyite, $Cu_{1.8}S$. Roxbyite has a complex structure with a large unit cell but can be approximated as a simple hexagonal structure. The reflections were accordingly assigned; 37.7° is the (102)-like planes, 46.5° is the (110)-like planes, and 48.9° is the (103)-like planes. HR-TEM showed that the particles were single crystalline. A pair of perpendicular lattice fringes was assigned to d = 0.33 nm as

(100)-like planes and d = 0.19 nm as (110)-like planes. A third set of fringes, d = 0.23 nm, was assigned to (102)-like planes.

The distorted hcp anion lattice of roxbyite $Cu_{1.8}S$ indicates that there is a major structural transformation from the fcc anion lattice of π-SnS upon cation exchange. Our observation contrasts with many studies on cation exchange which highlight a retention of the anion sublattice. For example, in our own work we have found In^{3+} and Fe^{3+} exchanges into Cu_2S yield metastable wz-$CuInS_2$ and wz-$CuFeS_2$, rather than the thermodynamic chalcopyrite cubic-like phase.[77] The Schaak group has employed exchange of $Cu_{2-x}S$ from the cubic-like (digenite) and hexagonal-like (roxbyite) phases to zinc blende and wurtzite CoS and MnS.[51,60] They show that there is a retention of both the cation and the anion lattices, as expressed in the anion stacking (ccp or hcp) and the holes (tetrahedral, not octahedral).

It is particularly intriguing that the anion lattice is not retained in the cation exchange to copper(I) sulfide as both hexagonal and cubic polymorphs are known. One might predict that the fcc lattice of rock-salt-like π-SnS in the cation exchanged with Cu^{1+} would yield cubic $Cu_{2-x}S$ digenite, anilite, or geerite (all have fcc anion lattices, with slightly different cation placement and vacancy orderings). Digenite, in particular, has been isolated in nanocrystals previously, is stable above 73 °C, and is metastable at room temperature.[128] It should be noted that there is a small lattice mismatch of less than 8% in this system despite the large change in the cation radius (Cu(I) ~ 77 pm and Sn(II) ~ 118 pm).[129] The pseudoclose packed directions have lattice spacings of 3.58 Å for roxbyite, 3.22 Å for digenite, and 3.35 Å for π-SnS.[130,131] Therefore, large lattice mismatch cannot be implicated for phase changes.[61] Furthermore, the activation energy for the transformation of digenite into a hexagonal phase such as roxbyite requires temperatures between 300 and 400

°C; such a transformation requires the presence of defects and extensive slip planes.[132,133] The cation exchange processes likely induce the required defects for such a transformation.

A plausible reason for the rearrangement of the anion lattice to yield the thermodynamic product is mismatched rates of ion diffusion, which cause the transient formation of phase-change catalyzing defects. A similar phenomenon was seen in the phase-controlled exchange of hexagonal-Cu_2S to $CuFeS_2$.[51] When the rates of Cu^{1+} removal and Fe^{3+} incorporation were matched, the hexagonal lattice of the host material was maintained to yield metastable wurtzite-like $CuFeS_2$. When the Fe^{3+} incorporation was hindered by strongly coordinating ligands in solution, the lattice transformed to the thermodynamic cubic phase $CuFeS_2$. It was hypothesized that transient defects caused by cation deficiencies were necessary to catalyze the lattice transformation.

In the experiments here, when π-SnS@Cu-Sn-S particles underwent complete cation exchange to $Cu_{1.8}S$@Sn-Cu-S, noticeable voids in the material resulted, usually on one face (though the size of the overall structure remains similar to that of the host (52 ± 5 nm, n = 120)). Such voids are a hallmark of the Kirkendall effect (Figure 3.6, Figure B.13) of slow diffusion inward compared to diffusion outward.[110,112,113,134] A study of the samples in which only some particles had undergone complete exchange is illuminating. While some pitting of the shells is observed in the π-SnS@Cu-Sn-S particles that remained, the large voids were exclusively and consistently observed in particles that had undergone exchange (Figure 3.7). This suggests that the voids are formed from the speedy diffusion of tin out of the nanostructures compared to the copper incorporation. Buhro et al. also observed a similar case of hollow formation at the interior of $CuInS_2$, while performing the diffusion of In^{3+} into $Cu_{(2-x)}S$, and has predicted that the fast outward diffusion of Cu^+ relative to the inward diffusion of In^{3+} causes the material to erode from

the center of the nanodisks.[110] Here, the opposite is seen where the copper has a slow diffusion compared to the Sn. This is remarkable as both the cubic-like and hexagonal-like copper(I) sulfides have high cation mobilities at temperatures over 100 °C.[48,49] Why, therefore, is the inward copper diffusion slow in this system?

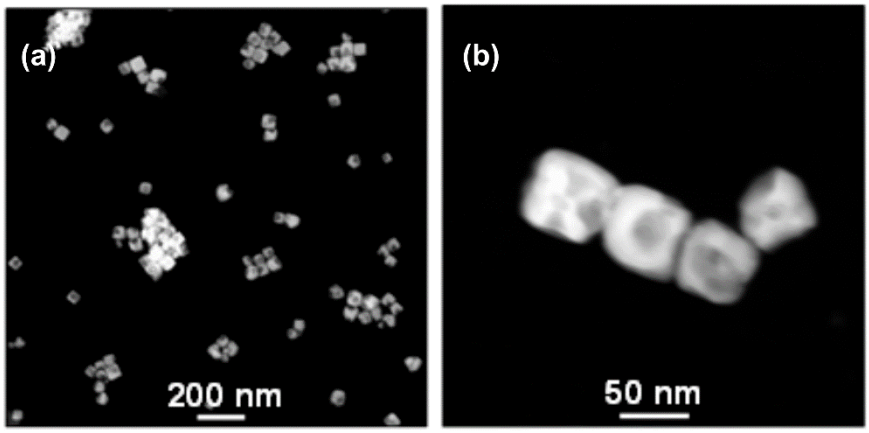

Figure 3.6. High-angle annular dark field (HAADF) imaging of $Cu_{1.8}S$@Sn-Cu-S nanocubes illustrating the voids in the structure. Reprinted with permission from Chem. Mater. 2021, 33, 8, 3011–3019. Copyright 2021 American Chemical Society.

Clues to the mechanism of the transformation came through the attempts to capture intermediates of the cation exchange reactions. Other have used these intermediates to understand the dominating epitaxial relationships between the two phases that can be observed, and the crystallographic "directions of attack" that can be deduced.[129,135–137] The Manna group has studied the conversion of particles with cubic-like crystal structures of Cu_2X to cubic SnX (X = Se or Te). In both cases, the exchange was gradual and the heterostructured intermediates contained crystalline domains of each species. While core−shell structures could be obtained, they were metastable and resolved to Janus-type structures at higher temperatures.[124,135,138]

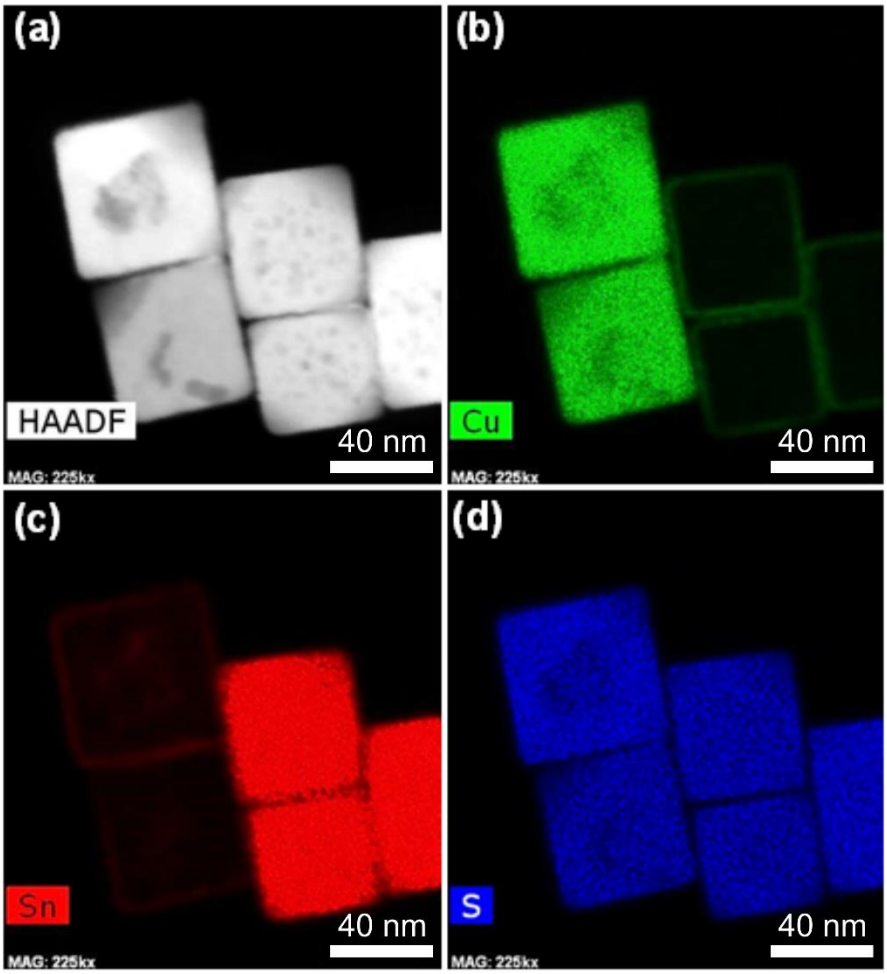

Figure 3.7. (a–d) EDS elemental mapping of an aliquot collected at 155 °C. Reprinted with permission from Chem. Mater. 2021, 33, 8, 3011–3019. Copyright 2021 American Chemical Society.

In an attempt to capture cation exchange intermediates in this reaction, aliquot studies, lower Cu^+ concentrations, lower reaction temperatures (Figure 3.7 and Figures B.4–B.7 and B.14) and different sizes of host particles (Figure B.9) were attempted. Others have previously observed striped or patchy Janus-type particles as intermediates.[134,136,139–142] However, such structures were not readily observed. While both cubic and tetragonal Cu-Sn-S phases are known, no ternary structures were captured. Instead, we observed individual particles that had completely exchanged to $Cu_{1.8}S$@Sn-Cu-S, while others remained intact as π-SnS@Cu-Sn-S (Figure 3.7, Figure B.14). In the thousands of particles imaged across more than 50 samples, only two particles demonstrated

hemispheres of $Cu_{1.8}S$ and SnS in the core (Figure B.10). This was seen upon exchange of smaller, ~20 nm SnS particles that were near spherical and lacked the strong faceting seen in the larger particles. It is likely these smaller particles contained internal defects that prevented complete exchange.

The inability to capture intermediate structures suggests that once cation exchange is initiated in each particle, the reaction proceeds to completion rapidly. Jain has observed and noted cooperative mechanisms for cation exchange from CdSe to Ag_2Se and Cu_2Se.[143] The initial diffusion of the first guest cation catalyzes the incorporation of further cations. As a result, after surpassing the activation barrier of the initial diffusion of the first cation, individual particles undergo an avalanche of cation exchange, leaving other particles yet untouched. A theoretical model proposed by Ott et al. suggests that the cooperative mechanism results from, in part, Coulombic interactions resultant from the differing valences of the host Cd^{2+} and guest Ag^{+} cations.[144] We more recently observed a cooperative mechanism in the cation exchange of Cu_2S to $Cu^{1+}Fe^{3+}S_2$.[51] Cation charge is not the only factor that leads to a cooperative mechanism as the exchange of CdS to Cu_2S does not occur through a cooperative mechanism, and instead Janus intermediates can be obtained. Therefore, it leaves additional questions as to the additional factors that lead to cooperative exchange of SnS to $Cu_{1.8}S$.

Judging by the ratio of exchanged to nonexchanged particles, the event that catalyzes the cation exchange happens more often with smaller particles and higher reaction temperatures. While some nanocuboids will exchange at lower temperatures, even with extended annealing time (1 h), not all of the cuboids to convert to $Cu_{1.8}S$@Sn-Cu-S (Figure B.8). For smaller nanocuboids (23 ± 2 nm, n = 120), some had undergone complete cation exchange to $Cu_{1.8}S$@Sn-Cu-S at the low reaction temperature of 120 °C, but again, high temperatures of 170 °C were required to fully

transform the assembly. Because there is not one universal onset temperature for small particles and another for large, each particle has its own "activation barrier" that is likely related to the locally variable structure and composition of the amorphous Cu-Sn-S shell. It should be noted that the core/shell structures and voided particles decompose when the exchange mixture is brought to the high temperature of 300 °C. The product is a mixture of chalcocite and CuSn (bronze) alloy particles (Figures B.15 and B.16).

The chemical potential of copper is also important to initiate the full cation exchange. For instance, upon increasing the Cu^{+}:Sn^{2+} ratio from 5:1 to 7.5:1, complete conversion to $Cu_{1.8}S$@Sn-Cu-S occurs at a temperature lower than that of the optimized case (detail in Figure B.11). When the amount of copper-coordinating TBP was increased from 1.0 to 1.5 mL, the cation exchange processes were inhibited.[145] Only π-SnS@ Cu-Sn-S nanocuboids were observed even after heating to 170 °C (Figure B.12). It can be hypothesized that the global cation exchange event is catalyzed by the amorphous Cu-Sn-S being breached by reactive copper ions through local weaknesses. Since the product particles each have a distinctive void centered on a face, one way to visualize the process is the Cu-Sn-S shell rupturing under pressure from copper trying to diffuse into the core and breaching the Cu-Sn-S shell. The rupture on one facet triggers a rapid loss of Sn^{2+} while stoichiometry dictates that nearly twice as much Cu^{1+} more slowly diffuses in through the same aperture under the current of escaping Sn^{2+}.

The following solar cell work was performed by Shane Finn. π-SnS has been identified as a new solar cell absorber material with its band gap of ~1.7 eV, which is significantly larger than the 1.3 eV band gap of α-SnS. π-SnS should therefore give cells with a larger photovoltage than α-SnS and could be incorporated into tandem cell designs. However, to date, π-SnS has been underperforming, yielding photovoltages of under 217 mV in functioning cells.[118,119,146] While the

reason is yet unclear, it can be hypothesized that there is carrier trapping into the defects. This study provides a convenient opportunity to test whether those defects are in the core or at the surface of the π-SnS; the products here are highly faceted, and the intermediate cation exchange products have very uniform 4 nm shells of Cu-Sn-S.

To illustrate how the amorphous mixed metal shell effects the photoresponses of π-SnS, the comparative photovoltaic performances of the pristine π-SnS, π-SnS@Cu-Sn-S, and $Cu_{1.8}S$@Sn-Cu-S core−shell nanocuboids were measured. The particles were tested (Figure 3.8) as photoabsorber materials in quantum dot sensitized solar cells (QDSSCs) prepared according to previous work,[147] with the general structure of FTO/TiO_2/nanocrystals/ZnS/polysulfide/MoS_2/Mo.

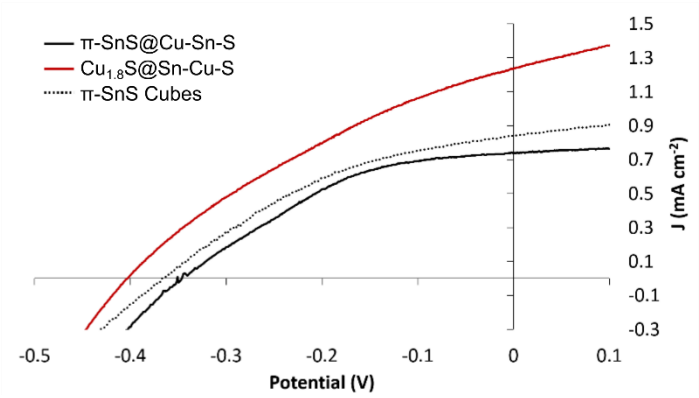

Figure 3.8. (a) J−V curve of the devices prepared using π-SnS@Cu-SnS (black), $Cu_{1.8}S$@Sn-Cu-S (red), and π-SnS (black dashed) nanoparticles under 1 Sun illumination (AM 1.5). Reprinted with permission from Chem. Mater. 2021, 33, 8, 3011–3019. Copyright 2021 American Chemical Society.

QDSSCs prepared with π-SnS nanocrystals had a larger Voc of 367 mV and a marginally better fill factor of 39% than a reported thin film cell of FTO/TiO_2/π-SnS/CdS/ZnS/ITO (217 mV and 34%) but underperformed greatly in terms of the Jsc (0.84 mA/cm^2 vs 5.4 mA/cm^2) (Table 1).[118,119,146] The poor Jsc is likely due to design differences in the thin film, QDSSCs changing the quantity of material absorbing light, and a lower driving force for charge separation across the whole system. Conversely, better potential alignments through the QDSSC system with fewer

voltage losses compared to the existing thin film designs can explain the improved Voc and is recordbreaking for π-SnS solar cell designs.[118,119,146]

Table 1. Solar Cell Characteristics of Liquid Junction QDSSCs

Photoabsorber	V_{OC} (mV)	J_{sc} (mA cm^{-2})	FF	η (%)
SnS@Cu-Sn-S	346	0.74	0.41	0.105
$Cu_{1.8}S$@Sn-Cu-S	403	1.24	0.33	0.164
SnS cuboids	367	0.84	0.39	0.119

When the shell of Cu-Sn-S was added to the π-SnS, there was only a small decrease in Voc. This is evidence that the defect or inherent semiconductor characteristic that leads to the universally poor Voc in existing π-SnS solar cell designs is not surface-based but rather in the core of the material. The increased fill factor between π-SnS and π-SnS@Cu-Sn-S suggests that the amorphous shell actually decreases resistance in the system. This may either be through increased electron injection to the TiO_2 or may be through better catalytic oxidation of the polysulfide electrolyte, the electrochemistry of which is known to be catalyzed on copper sulfide surfaces.[148,149]

Upon complete exchange to $Cu_{1.8}S$@Sn-Cu-S, the Voc jumped up to 403 mV and the Jsc to 1.24 mA/cm^2. The cell characteristics are now dominated by the roxbyite $Cu_{1.8}S$ which lacks the voltage-directing core defect of the π-SnS. The Jsc is much improved because the band gap of roxbyite is ~1.3 compared to that of 1.7 for the π-SnS and therefore absorbs more photons from the white light source.[150]

3.4 Conclusion

In this work, we show preferential phase selection in the cation exchange of cubic π-SnS to a pseudohexagonal $Cu_{1.8}S$ roxbyite core. Addition of Cu^{+} to π-SnS nanocuboids in solution produces several monolayers of amorphous Cu-Sn-S around the π-SnS core that became apparent only with HRTEM and EDS mapping. Raising the reaction temperature results in an avalanche-like exchange of the core to products of the $Cu_{1.8}S$@ Sn-Cu-S core−shell nanocuboids. The inability to capture intermediates with particles that contain domains of both Cu1.8S and π-SnS and the formation of voids in the products suggest that the cation exchange occurs through a "popping" of the shell followed by very fast exchange, where Sn^{2+} leaves faster than Cu^{1+} enters. The mismatched exchange kinetics are implicated as forming transient defects that catalyze the transformation of the sulfur lattice from pseudo-fcc to pseudo-hcp. The presence of defects during the replacement of tin forms of a cavity in the $Cu_{1.8}S$@Sn-Cu-S nanocuboids and is interpreted as the Kirkendall effect in nanoscale material.

The lesson to be learned is that the formation of very thin shells at intermediate steps in a cation exchange can greatly alter the diffusion kinetics in a system and thereby influence how a phase is retained. It is only through careful surface analysis of the intermediates, such as EDS mapping, that such a mechanism can be identified.

The particles were studied in QDSSC designs to examine how the mixed metal shell would influence the performance of π-SnS, which is an exciting, new, but underperforming photoabsorber material. As expected, the cells prepared with π-SnS showed a Voc value of only 367 mV, which is recordbreaking, but still well below the ideal given the 1.7 eV band gap of π-SnS.[118,119,146] The addition of Cu-Sn-S shells did not drastically change the cell characteristics, suggesting that the defect that is causing the low voltages is not surface associated.

3.5 Experimental

Materials. Tin(II) chloride (SnCl2, 99.99%), thiourea (≥ 99.0%), hexadecylamine (HDA, tech., 97%) oleylamine (OlAm, Aldrich, 70%), tri-butylphosphine (TBP, tech., 97%), Copper (I) chloride (CuCl, 97%), toluene, and isopropanol were purchased from Sigma Aldrich. All chemicals were used as received without further purification.

Cu^+ exchange of π-SnS Nanocuboids. The 1st step of this process is a synthesis of π-SnS nanocuboids, and the 2nd step is Cu^+ treatment to the as synthesized nanocrystals.

Synthesis of 75 ± 10 nm π-SnS Nanocuboids. Nanocuboids of π-SnS were synthesized following a modified literature method.[120] Typically, in a round bottom three neck flask, 38 mg (0.2 mmol) $SnCl_2$ and 2 g HDA were loaded. The mixture was placed under vacuum for 30 minutes at 100 °C, creating a turbid light brown solution. Then, 1 mL TBP (kept under N_2 atmosphere) was injected into the solution, and the temperature of the reaction mixture was further raised to 190 °C at a heating rate of 15 °C/min to get a transparent solution. The reaction solution was allowed to cool down to 160 °C. A hot solution of thiourea (12 mg, 0.16 mmol) dissolved in HDA (0.5 gm) through gentle heating in inert atmosphere was then injected into the reaction mixture at 160 °C. The reaction solution turned deep brown immediately after the injection, indicating the formation of π-SnS nanocuboids. It was annealed at the same temperature for a minute. The flask was then cooled to 155°C and annealed further for a total time of 20 minutes to get the desired size of π-SnS nanocuboids. It was further cooled down to 100 °C for Cu^+ treatment.

Cu^+ Treatment of 75 ± 10 nm π-SnS Nanocuboids. After cooling down the reaction solution to 100 °C, 2.2 mL of crude solution was removed for characterization after which a solution of CuCl (45 mg) dissolved in 2 mL of oleylamine under inert atmosphere was injected into the remaining solution of nanocuboids. Then the temperature of the reaction solution was raised to 170 °C (20 °C/min). Aliquots were collected at the different time points, while raising the temperature to 170 °C. All aliquots were cleaned in triplicate using a mixture of toluene and isopropanol centrifuging at 8700 rpm for 5 minutes.

Synthesis of 53 ± 5 nm π-SnS Nanocuboids. In a round bottom three neck flask, 38 mg (0.2 mmol) $SnCl_2$ and 2 gm HDA were loaded. The mixture was placed under vacuum for 30 minutes at 100 °C. It turned a turbid light brown solution. Then, 1 mL TBP (kept under N_2 atmosphere) was injected into the solution, and the temperature of the reaction mixture was further raised to 190 °C with a heating rate of 15 °C/min to get a transparent solution. The reaction mixture was allowed to cool to 175 °C, and a hot solution of thiourea (12 mg, 0.16 mmol) dissolved in HDA (1 gm) through gentle heating in inert atmosphere was injected into the reaction mixture at 175 °C. The reaction solution turned deep brown immediately after the injection, indicating the formation of π-SnS nanocuboids. It was annealed at the same temperature for a minute, after that, it was slowly (15 °C/min) cooled down to 155 °C and annealed for a total time of 20 minutes to get the desired size of π-SnS nanocuboids. It was further cooled down to 100 °C for Cu+ treatment.

Cu^+ Treatment of 53 ± 5 nm π-SnS Nanocuboids. After cooling down the reaction solution to 100 °C, 2.6 mL of crude solution was removed after which a solution of CuCl (45 mg) dissolved

in 2 mL of oleylamine under inert atmosphere was injected into the reaction mixture. Then the temperature of the reaction solution was raised to 170 °C (20 °C/min). Aliquots were collected at the different time points, while raising the temperature to 170 °C. All aliquots were cleaned in triplicate using a mixture of toluene and isopropanol centrifuging at 8700 rpm for 5 minutes.

Synthesis of 22 ± 3 nm π-SnS Nanocuboids. In a round bottom three neck flask, 38 mg (0.2 mmol) $SnCl_2$ and 2 gm HDA were loaded. The mixture was placed under vacuum for 30 minutes at 100 °C. It turned a turbid light brown solution. Then, 1 mL TBP (kept under N_2 atmosphere) was injected into the solution, and the temperature of the reaction mixture was further raised to 190 °C with a heating rate of 15 °C/min to get a transparent solution. The reaction mixture was allowed to cool down to 160 °C, and a hot solution of thiourea (39 mg, 0.51 mmol) dissolved in HDA (1.4 g) through gentle heating in inert atmosphere was injected into the reaction mixture at 160 °C. The solution turned deep brown immediately after the injection. It was annealed at the same temperature for a minute, after that, it was slowly (15 °C/min) cooled down to 155 °C and annealed for a total time of 20 minutes to get the desired size of π-SnS nanocuboids. It was further cooled down to 100 °C for Cu^+ treatment.

Cu^+ Treatment of 22 ± 3 nm π-SnS Nanocuboids. After cooling down the reaction solution to 100 °C, 3.2 mL of crude solution was removed after which a solution of CuCl (45 mg) dissolved in 2 mL of oleylamine under inert atmosphere was injected into the reaction mixture. Then the temperature of the reaction solution was raised to 170 °C (20 °C/min). Aliquots were collected at

the different time points, while raising the temperature to 170 °C. All aliquots were cleaned in triplicate using a mixture of toluene and isopropanol centrifuging at 8700 rpm for 5 minutes.

Instrumentation. Optical spectroscopy was collected using a UV-visible spectrophotometer (Jasco V-670). Photoluminescence spectra were measured using a spectrofluorometer (Jasco FP-8300) with excitation wavelength, 348 nm. Transmission electron microscopy (TEM) images were collected and energy dispersive X-ray spectroscopy (EDS) was carried out using a FEI Tecnai Osiris digital 200 kV S/TEM system. TEM samples were prepared by dropcasting a dilute solution of the nanostructures dispersed in hexanes onto a carbon coated nickel grid and drying in air at room temperature. Powder X-ray diffraction (XRD) was performed with the purified sample in powder form using a Scintag XGEN-4000 as well as a Rigaku SmartLab powder X-ray diffractometer both with a CuKα ($\lambda = 0.154$ nm) radiation source.

Chapter 4

PROGRESS TOWARDS SYNTHESIS AND CHARACTERIZATION OF $Cu_2Au_5Se_3$

4.1 Abstract

The following chapter discusses the synthesis and characterization of novel $Cu_2Au_5Se_3$ through cation exchange of hexagonal Cu_2Se host NPs. Cu_2Se nanodisks were nucleated via one-pot direct synthesis using copper(II) acetylacetonate and didodecyl diselenide as the selenium source and ligand. Auric ions were then introduced as a gold chloride salt to yield $Cu_2Au_5Se_3$. Quasi-spherical particles were then synthesized beginning with a wurtzite phase CdSe NCs which underwent full cuprous cation exchange towards hexagonal Cu_2Se, prior to the subsequent gold inclusion as described previously. Characterization was performed with powder X-ray diffraction (pXRD) and transmission electron microscopy (TEM). pXRD revealed a pattern which we were unable to match to any documented crystal phases, indicating either a novel crystal phase or mixture of several products of similar size and morphology. TEM of the quasi-spherical sample shows a homogenous product with respect to size, morphology, and elemental composition. EDS does indeed verify the presence of copper, gold, and selenium confined to the particle's structure as well as a relative ratio of roughly 2:5:3, respectively. Progress towards full characterization will likely necessitate diffraction of single nanocrystals with precisely controlled particle orientation or electron beam movement kinematic electron microscopy techniques. Elucidation of this novel phase could give insight on why certain phase transformations are observed during ion exchange and further enhance our ability to target specific phase products.

4.2 Introduction

While researchers seek to develop new nanoscale products, a frequent roadblock to product development is the lack of available materials with desired composition and characteristics. As such, methodological studies of novel NP synthesis and characterization are vital to developing new nanotechnologies. Our lack of mechanistic understanding leads to nanosynthesis being described as a black box where our control of product formation is often less rigorous than other synthetic chemistry fields.[34,35,151] Elucidation of the conditions which dictate products formed have largely focused on crystal phase selectivity, morphology control, and size focusing. With respect to phase control, cation exchange is a technique used to synthesize product of predictable crystal phase from a host NP through exchange of its existing atoms with free ions outside the crystal lattice.[46] This technique often has the benefit of preservation of the anion sublattice of the host, thus lending predictability to the resulting phase and morphology of the product.[46] Furthermore, this technique can be performed with a limited number of cations introduced, thereby yielding particles of more complex elemental composition. These cornerstones of cation exchange make it a popular method for synthesizing new nanomaterials which may be difficult to isolate using conventional solvothermal nucleation techniques.

One focus of phase preservation is the potential for metastable products to be derived from a host particle. Due to the difficulty of isolating metastable crystal phases during nucleation events – resultant from the likelihood of lattice defects and unfavorable surface energies – cation exchange can be a viable alternative to synthesizing these unstable NCs. Through careful selection of a host particle with a desired anion sublattice, metastable products sharing a common phase with their precursor have been previously synthesized.[51,60,100,111,152,153] However, there has been less study on the instances of crystal lattice conversion during cation exchange. Explanations as to why

the lattice of the host was not preserved have included the presence of coordinating ligand, development of lattice defects via vacancies, NP diameter restrictions, exchange activation energy, and bond cleavage.[51,61,79,104] I have previously demonstrated the ability for coordinating ligands to hinder cation exchange by coordinating to free ions in solution, resulting in either driving the reaction or developing lattice vacancies which push the host particle towards a phase conversion to a more stable product.[51] Dong *et al*. proposed that critical diameters of host particles may encourage phase conversion during cation exchange.[154] When converting wurtzite CdSe to cubic Ag_2Se, it was proposed that host particles too close to the reaction-zone diameter of the material would favor reorganization of the lattice, while larger particles were more able to retain the host's anion sublattice.[154] Sarkar *et al*. and Moreels *et al*. both observed conversion of lattices in high temperature environments where the significant activation energy required to drive the exchange contributed the host's lattice rearrangement.[155,156] These instances of unexpected results during ion exchange demonstrate the need for elucidation of the parameters which most influence phase retention in NPs.

Many metal chalcogenides have been derived from copper based NCs, due to the high mobility of Cu ions in crystal lattices.[49,60,99,111,137,157,158] While this has been previously shown with a variety of independent material systems, the Schaak lab has synthesized structures with as many as six different metals existing in heterostructures derived from $Cu_{1.8}S$ nanorod hosts, demonstrating the versatility of this technique in copper systems.[114–116] However, such copper systems rarely make use of gold.[100,156,159–161] Furthermore, the only copper-gold-selenide nanoparticles reported in literature are heterostructures which do not incorporate auric ions into the NC lattice.[161]

The following reports preliminary results of the synthesis and characterization of novel $Cu_2Au_5Se_3$ nanoparticles obtained via cation exchange of hexagonal Cu_2S. Morphologies obtained include both nanoscale platelets and quasi-spheres of between 10 and 20 nm. Crystal phase characterization was performed using powder X-ray diffraction (pXRD) with no known materials of similar phase found across several mineralogical databases. Further literature searches independent of crystallographic information file (.CIF) databases did not yield any similar materials reported. Transmission electron microscopy (TEM) imaging was used to monitor morphology and crystallinity of the samples from hosts to final products, where single crystalline NCs were observed across multiple exchange steps. Energy dispersive X-ray spectroscopy (EDS) was used to determine an approximate stochiometric ratio of elemental composition while mapping data verified incorporation of the exchanged ions within the crystal lattice. With no reported crystal phases to derive the product's structure from, progress towards full characterization will likely necessitate diffraction of single nanocrystals while precisely controlling particle orientation and/or electron beam movement.

4.3 Preliminary Results and Discussion

Synthesis and characterization of hexagonal Cu_2Se nanodisk hosts was based on the work of Hernández-Pagán *et al.*[100] In brief, Copper(II) acetylacetonate ($Cu(acac)_2$) and didodecyl diselenide (DD_2Se_2) were combined in octadecene (ODE) prior to heating at 165 °C for 1 hour. The nanodisks were then cooled and washed in triplicate with toluene and acetone. The resulting disks were approximately 10.01 ± 2.87 nm (n = 250) in diameter by 3.35 ± 0.50 nm (n = 50) thick as observed in TEM and possessed the same hexagonal structure reported by the Manna group.[111]

(Figure 4.1) While their reported synthesis yielded quasi-spherical Cu_2Se NCs rather than nanodisks, the one-pot synthesis used was chosen for simplicity's sake.

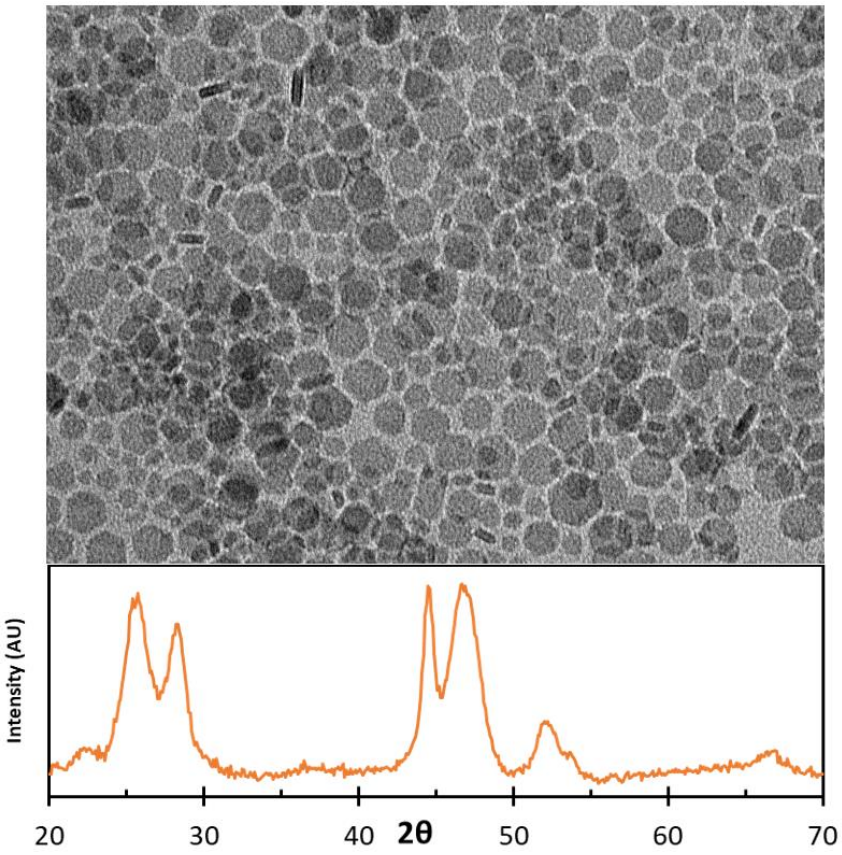

Figure 4.1 TEM imaging of hexagonal Cu_2Se nanodisks synthesized via one-pot method. pXRD matches diffraction data reported by the Manna group with the Scherrer broadening expected from small lattice areas.

Synthesis of $Cu_2Au_5Se_3$ was performed by stirring in a toluene solution of host Cu_2Se NCs with an injection of $AuCl_3$ dissolved in toluene and oleylamine (OLAM). The primary amine facilitated solubility of the gold in non-polar solution while also driving the copper from the lattice. Resulting particles were characterized by pXRD and TEM, however their disk-like morphologies resulted in numerous complications during the acquisition and interpretation of the data. Signals observed in pXRD possessed unresolved peaks while also appearing at angles corresponding to unreasonably large lattice spacings, which are known phenomenon with non-0D NP morphologies. (Figure C.1) Due to the tendency for disks and rods to deposit with preferred orientation when

drop casting, certain crystal facets may not be visible at their corresponding Bragg angle. Furthermore, artifact signals may appear if the NPs begin to stack uniformly on top of each other, effectively turning the thickness of a disk or sheet into a pseudo-spacing in the crystal structure.

TEM imaging continued to prove challenging as the nanodisks would quickly degrade under the electron beam. While standard TEM imaging was obtainable, the extended probing necessary for scanning TEM made elemental mapping difficult to obtain. Due to the rasterization necessary in scanning TEM, the electron beam assumes a sub-nm spot size, resulting in increased mobility of the atoms in the lattice and ultimately decomposition of the entire nanodisk. (Figure C.2) Copper and gold are known for particularly high mobilities – particularly at material surfaces – resulting in disproportionation under thermal strain, so high energy electron beam probing would understandably cause similar issues.[49,157,158,162,163] This issue is exacerbated in low volume structures, making $Cu_2Au_5Se_3$ nanodisks particularly difficult to characterize.

Zero dimensional $Cu_2Au_5Se_3$ was synthesized through a two-step cation exchange, where the CdSe and CuSe hosts were made in accordance with two reported syntheses.[111,164] Briefly, large-volume wurtzite phase CdSe was synthesized through combination CdO and elemental selenium in a solution of trioctylphosphine (TOP), trioctylphosphine oxide (TOPO), octadecylphosphonic acid (ODPA) and hexylphosphonic acid (HPA). The reaction was run at 370 °C before cooling and washing in hexanes and methanol. Their phase and morphology were confirmed with pXRD and scanning electron microscopy (SEM) with an average diameter of 15.3 ± 2.1 nm (n = 100). (Figure 4.2) CdSe NCs were then stirred with tetrakis(acetonitrile)copper(I) hexafluorophosphate in toluene and methanol to exchange the cadmium and cuprous ions. The resulting hexagonal Cu_2Se was then subjected to the same auric ion exchange previously described for the nanodisks.

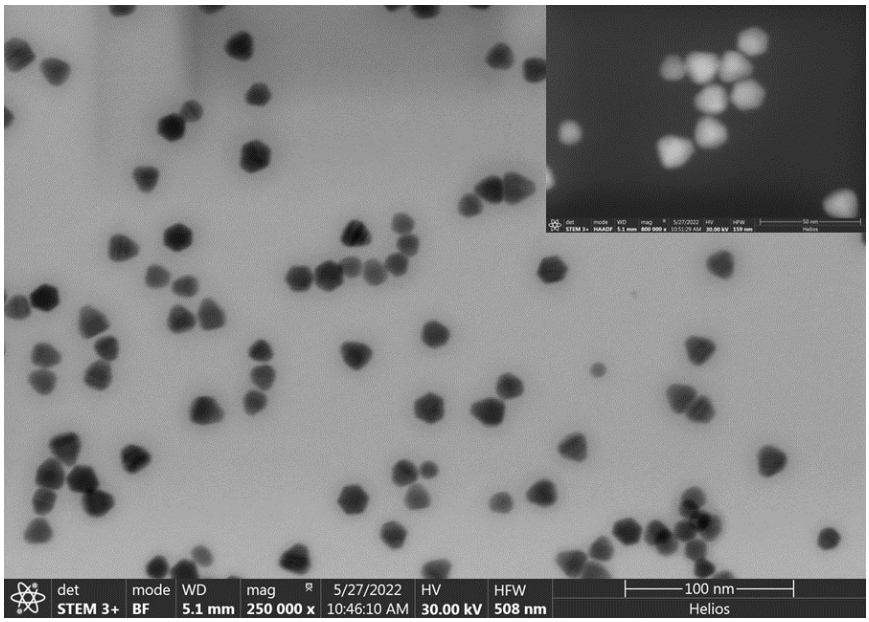

Figure 4.2 SEM bright field and high angle annular dark field (HAADF) of wurtzite CdSe nanoparticles . Scale bar of inlayed (HAADF) image is 50 nm and voltage remains consistent at 30 kV.

The resulting $Cu_2Au_5Se_3$ possessed a quasi-spherical morphology of 14.16 ± 1.94 nm (n = 200) in diameter. Indeed, this allowed for more random orientation of NCs during pXRD sample preparation. The resulting diffraction patterns were rid of artifact peaks observed from disk stacking as well as fully resolving previously unobserved signals. (Figure 4.3, C.3) The pattern observed was not able to be matched to any known crystal phase – or combinations thereof – reported in the Crystallographic Open Database or the Inorganic Crystal Structure Database. Expanding this search to include all transition metals, sulfur, and various main group elements did not yield any analogous structures which $Cu_2Au_5Se_3$ could be based on. Further literature searches showed no reports of similar ternary structures. Unfortunately, phase and space group characterization are limited in the nanoscale due to the 1-dimensional nature of powder diffraction compared.

To overcome this, simulation fitting and refinement are used when solving a powder diffraction pattern. Current techniques involve estimating a unit cell – often derived from an

analogous structure – and manipulating individual variables of atom placement and unit cell dimensions to fit simulated reflections to the experimentally observed intensities.[165] With modern computing, this process is a viable method of elucidating crystal structures from only a powder diffraction pattern, however there are limitations in applicability. This process is most efficient when analogous structures to derive a novel one from exist, as the general structure of the crystal lattice should only minorly vary with respect to reflection spacing and intensity. For example, Chapter 2 derives a novel hexagonal structure of $CuFeS_2$ from the wurtzite parent structure.[51] Materials such as hexagonal ZnS and CdSe diffract similarly, therefore the novel product was indexed by beginning with a generic wurtzite structure and adjusting the unit cell parameters as needed to sufficiently fit the experimental data acquired.

However, in the event no parent structure can be determined, there may be several reasons as to why. Firstly, the product in question may have too poor crystallinity to be accurately indexed by pXRD, particularly if signals observed are broad enough to obscure other low-intensity peaks. Optimistically, the product in question may possess a crystal structure significantly different than all known phases that it has been checked against. However, the more likely alternative explanation is that the sample is heterogeneous, resulting in a diffraction pattern comprised of several different phases. Therefore, further analysis of this product may necessitate diffraction performed in electron microscopy to eliminate heterogenous particle variability.

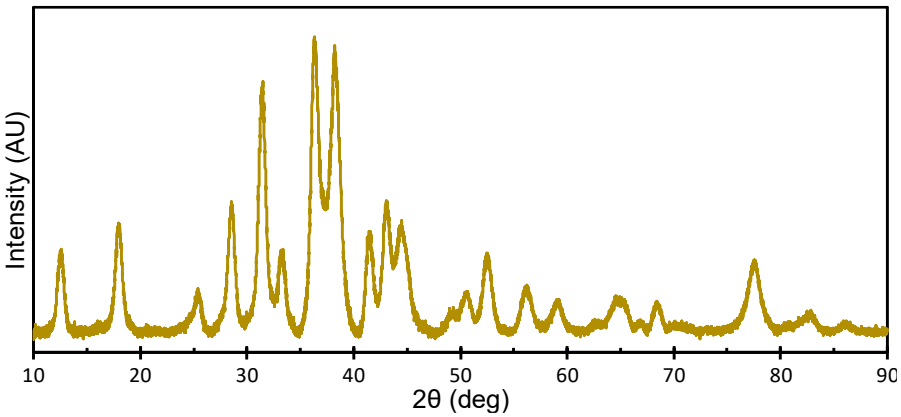

Figure 4.3 pXRD of quasi-spherical $Cu_2Au_5Se_3$ NCs. Signals acquired possess fairly uniform full width half maximums as expected from a 0D single crystalline powder sample.

The larger volume crystals proved much more robust during TEM imaging compared to the nanodisks, allowing for better visualization of the crystal lattice as well as dark field imaging for elemental mapping and quantification. (Figure 4.4) The NCs did not experience significant degradation even after 2 minutes under high resolution rasterized scanning. Elemental maps verified that gold was in fact restricted to the NC volume and elemental analysis indicated an average stochiometric ratio of 22.3:47.6:30.1 normalized atomic percent. High resolution TEM of the NCs demonstrated retention of single crystallinity in the product, which indicates minimal anion reorganization throughout the two ion exchanges. This suggests that $Cu_2Au_5Se_3$ may be hexagonal in nature if the selenium sublattice was in fact retained from the initial wurtzite CdSe host.

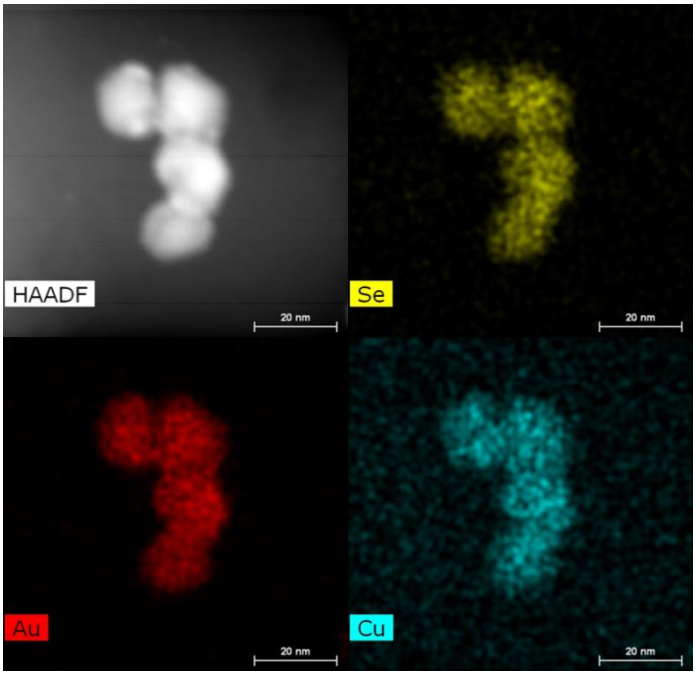

Figure 4.4 TEM HAADF and EDS mapping acquired for quasi-spherical $Cu_2Au_5Se_3$ NCs. Mapping acquired demonstrates gold signal overlapping the particle area with fairly uniform intensity distribution, indicating consistent gold exchange throughout the particle.

4.4 Future Directions

As previously mentioned, elucidation of the structure of $Cu_2Au_5Se_3$ will necessitate either the synthesis of a bulk single crystal or diffraction of a single NC during electron microscopy. The former presents little viability, as the lack of reports in general may be indicative of the material being metastable, and therefore difficult to synthesize using traditional solution-phase crystallization methods. While cation exchange has been demonstrated to an extent in bulk-scale materials, the hexagonal Cu_2Se hosts themselves are known to be metastable, virtually eliminating the viability synthesizing a bulk scale precursor.[100,111] Therefore, diffraction efforts towards solving the crystal phase in question may need to be performed with electrons rather than X-rays, as smaller probe sizes and the lensable nature of electron beams make microscopy techniques more suitable for diffraction at the nanoscale.

A potential method of electron diffraction in a microscopy apparatus is precession electron diffraction (PED), which has been used previously for solving nanoscale protein structures and inorganic crystals.[121,166–168] Being analogous to single-crystal X-ray diffraction, the data acquired consists of diffraction spots rather than the rings observed during diffraction of a randomly oriented cluster of particles.[168] However, instead of manipulating the crystal in space while acquiring diffraction data, PED instead uses a series of lenses to precess the beam about an axis at a defined angle, allowing for visualization of diffraction spots further in d-space compared to traditional electron diffraction techniques.[168] (Figure 4.5) The primary limitation of this technique is the very nature of beam tilting. As precession angle (φ) increases, diffraction patterns become more kinematical – due to the patterns being generated off of the zone axis – however this very deviation can accentuate spherical aberrations (C_s) in the probe lens. Additional considerations include probe diameter (d), as size minimums are typically 50 nm, but can be made much smaller in aberration corrected systems.[169,170] These parameters can be related in the equation below, where α denotes the convergence angle of the electron beam.[171]

$$d \propto 4C_s\varphi^2\alpha$$

Further practical constraints include material size, as thickness of the sample must fall within certain ranges for acquisition to be feasible. Most samples which undergo precession are sub-50 nm thick, which is ideal for generating atomic structure maps using kinematic approximations.[168] Lastly, sample degradation under the electron beam can be heightened due to the small probe size and extended exposure time necessary in PED. So, while thinner samples are standard for these experiments, diminished volume could render a material unsuitable for extended imaging sessions. With the above considerations in mind, the quasi-spherical $Cu_2Au_5Se_3$ may be

suitable for PED in an aberration corrected electron microscope assuming they do not degrade during data acquisition.

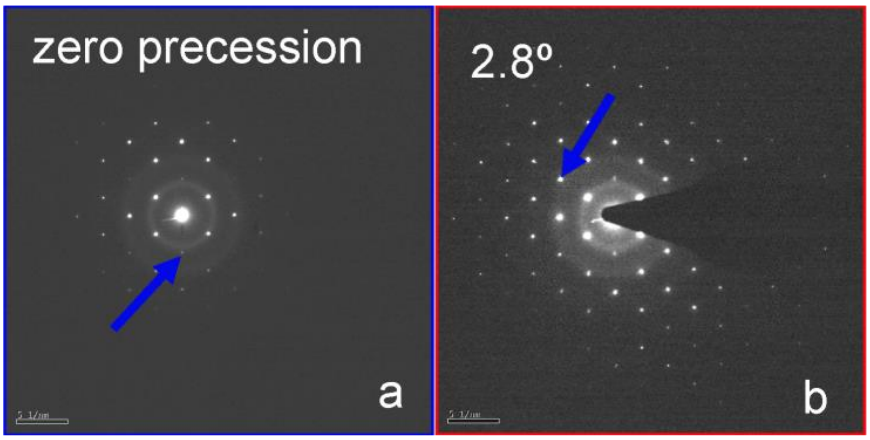

Figure 4.5 Electron diffraction of a silicon crystal directly comparing scanning area electron diffraction (SAED) and 2.8 degree PED acquisition. Kinematically forbidden reflections – (002) and (-22-2), respectively – are indicated with blue arrows.[168] Reproduced with permission from AIP Conference Proceedings 1173, 299 (2009). Copyright 2009, AIP Publishing.

An alternative to PED would be any number of microscopy techniques which are able to tilt a sample while using specialized software and AI to remain fixed on a single particle. In practice, this requires loading a sample holder (grid) with nanoparticles and choosing a lone particle with good crystallinity. The sample is then be raised to a specific height – referred to as the "z-height" – to prevent changes in distance from the detector as a goniometer tilts the sample about an access. As the sample is tilted, diffraction data is gathered and de-scanned into a map of diffraction spots suitable for phase determination. This data can be acquired using a variety of known methods such as automated diffraction tomography (ADT), rotation electron diffraction (RED), and microcrystal electron diffraction (Micro-ED); each of which incorporate movement of the particle in space as well as the electron beam.[166] In practice, it may be possible to acquire the necessary data simply by tilting the grid on a goniometer if the microscope being used has access to automatic sample acquisition and focusing software.

After data acquisition, the resulting diffraction spots may be processed in a software package such as X-ray Detector Software (XDS) designed for monochromatic diffraction processing. Successful processing would yield the space group and lattice parameters of the crystal in question which can then be used to search crystal databases for structures of similar structure. This seems to be the only reasonable method forward towards elucidating the structure of $Cu_2Au_5Se_3$ from a non-synthetic approach.

4.5 Experimental Methods

Materials. Sodium borohydride ($NaBH_4$, 99%) was supplied by Fisher Chemical. Cadmium Oxide (99.999%, CdO), copper(II) acetylacetonate ($Cu(acac)_2$, 98+%), and gold(III) chloride ($AuCl_3$, 99%) were supplied by Strem Chemical. Selenium (99.5+% trace-metal basis), 1-bromododecane (97%, 1-BrDD), tetrahydrofuran (99.9+%, THF), trioctylphosphine oxide (90%, TOPO), trioctylphosphine (90%, TOP), neocuproine hydrate (99%), octadecene (90%, ODE), octadecylamine (90%, ODA), and oleylamine (70%, OLAM) were supplied by Sigma-Aldrich. Octadecylphosphonic acid (ODPA) and hexylphosphonic acid (HPA) were supplied by PCI. OLAM was the only chemical distilled for synthetic purposes.

Didodecyl Diselenide. $C_{24}H_{50}Se_2$ Didodecyl Diselenide (DD_2Se_2) was synthesized following a method reported in literature.[172] A 1 L three neck flask with stir bar was flushed with argon prior to addition of 9.32 g (1.2 mol) Se and 75 mL (4.16 mol) DI water. The flask was then chilled for 10 minutes in an ice bath. Separately, 9.8 g (0.26 mol) $NaBH_4$ was added to a vial of 40 mL (2.22 mol) chilled DI water and broken up with a metal spatula. This was then pipetted into the 1 L flask

and a color change to white was observed. The solution was allowed to stir for 30 minutes before adding another 9.32 g (1.2 mL) Se at which point the contents turned dark with a black precipitate. The ice bath was removed, and the solution continued to stir for another 30 minutes. The flask was then heated to 70 °C and held for 30 minutes before being allowed to cool to RT (roughly 30 minutes; a brown precipitate may form). 56.44 mL (0.24 mol) 1-BrDD and 280 mL (3.45) THF were combined in a 500 mL separatory funnel and added to the 1 L flask dropwise. Solution may turn yellow with black precipitate. The 1 L flask was then heated to 50 °C and stirred for 18 h. After removing from heat and cooling to room temperature (roughly 30 minutes), the contents of the 1 L flasks were added to a separatory funnel and separated. The organic layer was washed once with a 1:1 volume equivalent of brine solution. The final organic layer was dried with $MgSO_4$, and solvent was removed under reduced pressure. The resulting oil was diluted with 70 mL HPLC grade heptane and recrystallized with cold IPA in an ice bath. The resulting crystals are yellow needles with the texture of glass wool. Yield = 61.5%.

Wurtzite CdSe Host Nanoparticles. Wurtzite phase CdSe hosts were synthesized following the method reported by Rice *et al*.[164] In a three neck round bottom flask (Flask 1) 3 g TOPO, 0.28 g ODPA and 0.06 g CdO were combined and placed on a Schlenk line. The mixture was then and degassed at 120 °C for 1 h before ramping to 300 °C. 0.7 mL of TOP was then injected into Flask 1 prior to ramping to 370 °C. Once at temperature, a solution of 0.058g Se in 1 mL TOP was injected into Flask 1 and allowed to react at 370 °C prior to cooling to room temperature. Separately, 3 g TOPO, 0.29 g ODPA, 0.08 g HPA and 0.057 g CdO were combined in a three neck round bottom (Flask 2) and degassed on a Schlenk line at 115 °C for 1 h before ramping to 350 °C. At temperature, a solution of 0.295 g Se in 3025 mL TOP and the contents of Flask 1 were

injected simultaneously into Flask 2 and allowed to react at 350 °C for 10 minutes. Flask 2 was then cooled to room temperature before washing in triplicate with hexanes and MeOH (1:1) at 8700 RPM for 5 minutes. The sample was then dispersed in toluene.

Hexagonal Cu_2Se Quasi-Spheres via Cation Exchange. Hexagonal Cu_2Se quasi-spherical hosts were synthesized following the method reported by Gariano *et al*.[152] The total yield of CdSe was assumed to contain 1 mmol of Cd^{2+} and dispersed in 4 mL anhydrous toluene. 1.5 mmol of tetrakis(acetonitrile)copper(I) hexafluorophosphate was solubilized in 6 mL of anhydrous MeOH before combining with CdSe and vortexing. The product was then washed twice in toluene and EtOH (1:1) before washing once in water at 8700 RPM for 5 minutes. The sample pellet was then dispersed in chloroform. The concentration of Cu(I)/mL in this stock solution was calculated using a previously reported based using UV-vis. A 10 uL aliquot of this solution was dissolved in a 10 mL volumetric flask with a mixture of 1:1 chloroform:MeOH and 50 mg neocuproine for 6 h. A 1 mL aliquot was then serial diluted to 5 mL before addition to a cuvette. The visible absorbance at 460 nm was measured and compared to a calibration curve of Cu(I) neocuproine.[94]

Hexagonal Cu_2Se Nanodisks via Solvothermal One-Pot. Hexagonal Cu_2Se nanodisk hosts were directly synthesized following a previously reported synthesis.[100] 524 mg $Cu(acac)_2$, 1092.4 mg DD_2Se_2, 10 mL ODE, and 215.6 mg ODA were combined in a three neck round bottom flask and degassed briefly at room temperature. The sample was then raised to 80 °C and further degassed for 30 minutes. After ramping to 165 °C, the solution was allowed to react for 1 h before cooling to room temperature. The sample was washed in triplicate with chloroform and acetone (1:2) at

8700 RPM for 5 minutes before dispersing in chloroform. The concentration of Cu(I)/mL in this stock solution was calculated using the method described for the quasi-spheres.

$Cu_2Au_5Se_3$ Nanoparticles. $Cu_2Au_5Se_3$ was synthesized through cation exchange. $AuCl_3$ was solubilized in a solution of 0.6 mL distilled OLAM and 6 mL anhydrous toluene before sparging with N_2 gas. This gold solution was then chilled in a IPA/N_2 bath. Separately, a volume of Cu_2Se (0.127 mmol Cu) was dispersed in 2 mL anhydrous toluene before injecting into the chilled $AuCl_3$ solution and stirring vigorously for 1 minute. The product was washed in triplicate in toluene:acetone (1:3) at 8700 RPM for 5 minutes. The final pellet was dispersed in a mixture of toluene and chloroform.

Instrumentation. Transmission electron microscopy (TEM) was acquired using a FEI Tecnai Osiris TEM operated at 200 keV. Powder x-ray diffraction (pXRD) was performed on a Rigaku SmartLab powder X-ray diffractometer with a CuKα (λ = 0.15418 nm) radiation source set to 40 kV and 44 mA, and a D/teX Ultra 250 1D silicon strip detector. pXRD patterns were acquired with a step size of 0.01° at 10° 2θ/min. Scanning electron microscopy (SEM) was performed with a Thermofisher Helios g3x at 30.00 kV.

Chapter 5

CONCLUSION

5.1 Summary

While there has been a push for alternative materials aimed at new technology development, phase selectivity can prove difficult in traditional solvothermal synthesis when novel phases and morphologies are sought. At the nanoscale these materials – which are often unseen in bulk – are able to be trapped through kinetic and thermodynamic approaches. Towards this end, the prevailing theme of this thesis demonstrates ion exchange as a viable approach towards achieving products of unusual structures and compositions. Despite the primary emphasis of ion exchange being phase and morphology preservation – a result of maintaining the counterion lattice throughout the reaction – occurrences of significant changes to the crystal lattice have been reported. With emphasis on copper chalcogen systems, ternary nanoparticles (NPs) of novel phase and morphology were synthesized post synthetically with discussion aimed at elucidating the experimental conditions which result in these changes. The following chapter summarizes the findings from the research presented above, followed by potential future work and the broad stroke impacts of this research in NP research.

Chapter 2 discussed the kinetic trapping of a hexagonal $CuFeS_2$ phase, which is a metastable product derived from a wurtzite (WZ) structure. Beginning with a preliminary synthesis for WZ-$CuFeS_2$, the reaction was further optimized while demonstrating that L-type ligands of variable donor strength would yield variable mixtures of hexagonal and tetragonal product. L-type ligands would strongly complex with ferric ions in solution – as demonstrated by color changes of

the aqueous iron ions – thus preventing complete exchange of copper with iron. As cuprous ions were continuing to be removed from the lattice by copper chelating neucuproine, vacancies would develop in the absence of free iron. Therefore, in accordance with Ostwald's rule, the hexagonal anion sublattice would collapse into a more stable tetragonal phase.

A linear trend was then drawn demonstrating that stronger donating ligands would prevent iron from exchanging quickly, allowing for vacancies to form and changing the nanocrystal (NC) kinetics to favor a tetragonal orientation. Despite ligand-based phase control suggesting a thermodynamic explanation to this trend, a kinetic approach was instead confirmed by reducing the amount of strongly donating L-type ligand, which produced the same products as would be expected in the presence of a large amount of weakly donating L-type ligand. Product was characterized with powder X-ray diffraction (pXRD) to determine phase identity and percent composition and transmission electron microscopy (TEM) for topography and lattice visualization. Energy dispersive X-ray spectroscopy (EDS) was used in determining elemental percent composition and mapping. In summary, this project further demonstrates the prevalence of Ostwald's rule when isolating metastable products while further clarifying experimental considerations developing ion exchange.

Chapter 3 covered post-synthetic conversion of π-SnS to $Cu_{1.8}S$@Sn-Cu-S core@shell nanocubes with large cavities, a known result of the Kirkendall effect. π-SnS nanocubes were synthesized in one pot solvothermally before hot injection of a copper-oleylamine complexed solution. While an initial Cu-Sn-S amorphous shell forms at relatively low temperatures, it is only at 170 °C where the copper becomes sufficiently mobile to penetrate the π-SnS cores, which is particularly high for achieving copper mobility through a crystal lattice. The rapid core@shell

exchange which follows results in a change of both the of the cubic core's phase and shell's elemental composition producing a hexagonal $Cu_{1.8}S$ core (roxbyite) and Sn-Cu-S shell.

This exchange occurs so quickly that no intermediate products could be isolated and observed in TEM. Instead, high angle annular dark field (HAADF) imaging shows pitting of the nanocube faces as copper ions attempt to penetrate the core, followed by an avalanche of ion movement out of the core once the energy barrier for ion diffusion and mobility is crossed. Due to the mismatch of ion diffusion rates during exchange (known as the "Kirkendall effect"), the higher speed of Sn leaving the NC core relative to the speed of Cu entering forms large cavities on one face of the nanocubes, resulting in $Cu_{1.8}S$ of high surface area relative to NC volume. The final products were identified as roxbyite via pXRD, with their elemental compositions and morphologies imaged in TEM. Further experiments involved photoabsorbance measurements in quantum dot sensitized solar cells (QDSSCs), where π-SnS shelling did not significantly improve performance. This finding opposes the hypothesis that defects which limit voltage in π-SnS solar cells is on the material surface, thereby suggesting the critical defects may be limited to the NC cores.

Chapter 4 contains preliminary work on the synthesis and characterization of $Cu_2Au_5Se_3$. A seemingly novel structure, $Cu_2Au_5Se_3$ is synthesized through cation exchange of hexagonal Cu_2Se with auric ions. While nanodisks were achievable without further synthetic efforts, quasi-spherical $Cu_2Au_5Se_3$ could only be achieved through synthesis of WZ CdSe, followed by Cu exchange to Cu_2Se and finally Au exchange. pXRD phase matching was unable to identify the signals acquired, suggesting the product is in fact novel, however an inability to find any matching phase (or phases) of any elemental composition is quite unusual. TEM tomography shows fairly

single-crystalline product with elemental composition of roughly 2:5:3 for copper, gold and selenium, respectively.

This chapter further discusses the steps needed to finalize characterization of the product. Due to the unlikelihood of synthesizing the product in the bulk scale, intensive electron diffraction will be necessary. Previously reported precession electron diffraction (PED) is a viable method for nanocrystal diffraction which uses a rotation of an electron beam about an axis to probe diffraction data in further out d-space. Additional electron diffraction techniques make use of this kinematic approach to crystal diffraction while combining it with movement of the sample holder. These methods – performed in microscopy instruments – are able to achieve probe sizes far below that of single crystal X-ray diffraction, making them ideal for characterization of micron and nanoscale materials. The resulting diffraction spots can then be analyzed in crystallography software, allowing for crystal phase space groups and lattice parameters to be elucidated.

5.2 Future Directions

Some of the work presented has proved relevant in recent publications. The alternative phases presented in Chapter 2 have been applied to thermoelectric thin films by Pang *et al*.[173] Phase conversion between the metastable WZ and thermodynamic chalcopyrite phases were shown to significantly impact thermoelectric properties of $CuFeS_2$ thin films, where manipulating the deposition temperature during radio-frequency magnetron sputtering resulted in mixed compositions of $CuFeS_2$.[173] It was found that mixtures of roughly 50:50 demonstrated the lowest electrical resistivity at all temperatures, while relatively pure WZ phase products demonstrated higher resistance even at elevated temperatures.[173] As such, mixed-phase $CuFeS_2$ synthesizable by

either magnetron sputtering or cation exchange in a moderately donating ligand may prove useful in nanoscale semiconductor thermoelectrics compared to their phase-pure counterparts.

In a broader context, the Brutchey group has explored copper-iron chalcogen nanomaterials in photovoltaic and optoelectronic technologies.[174] Particularly, DFT calculations indicated that the metastable WZ-like polymorph of $Cu_2FeSnSe_4$ has enhanced electronic structure, electron mobility, and longer-lived hot electrons compared to the thermodynamic phase, lending viability to photovoltaic applications.[174] Furthermore, the direct bandgap of around 1.48-1.59 eV is similar to popular optoelectronic nanoscale semiconductors like InP and CdSe.[175,176] This bandgap may even prove tunable as the metal ratios and alloying potential allow for flexible compositions. As such, further exploration of metastable WZ nanostructures may prove fruitful in novel technology applications.

With regard to Chapter 3, novel heterostructures and morphologies are highly sought-after products in ion exchange. In addition to core@shell structures which can help passivate surface defects for photoelectric applications, many different morphologies with unique elemental compositions across the structure are possible. Sen *et al*. has demonstrated Janus metal-telluride nanoparticles that are the result of either cation or anion exchange. $Cu_{2-x}Te$/M-Te Janus NPs and CdTe@SnTe core@shell structures were both synthesized through cation exchange, while CdTe/CdS stacked nanodisks were achieved through anion exchange.[177] On the extreme end of heterostructured nanomaterials, Steimle *et al*. used cation exchange to synthesize nanorods containing 6 distinct regions of metal sulfides and went on to demonstrate an unprecedented degree of control when isolating layered metal sulfide nanorods post-synthetically.[114–116] These striped nanorods may have applications in water splitting, photon upconversion and photodetection if the

layers can be arranged in such a way that band gaps and band-edge alignment permits direction electron and hole transport.

Progress of Chapter 4 largely relies on methodology development. As previously mentioned, while nanoscale crystal characterization is feasible by way of electron microscopy, sample sizes are often limited to tens or hundreds of nanometers at minimum. As a great deal of novel crystal phases have been isolated only in the nanoscale, increasingly precise and more widely available microscopy instruments will be necessary to characterize materials sub-50 nm in size. Elucidation of these novel materials will allow for further insight with regard to their properties and subsequently, potential applications.

5.3 Outlook

The broader impact of copper chalcogen ternary systems in nanomaterial synthesis is not one which should be dismissed. Barring potential applications of the materials described herein, exploration of the experimental considerations which determine products synthesized is critical to expansion of this relatively young field. The ability to quickly develop a synthetic route towards a proposed material is one which only comes with a great wealth of experimental knowledge and experience, both of which nanosynthesis lacks compared to other synthetic fields such as molecular chemistry. While investigating the black box of nanoscale reactions is an attractive pursuit for researchers, it comes with the consequence of lengthened development time and increased resource consumption towards specific goals. As such, all efforts in development of novel nanomaterials are a great boon to this rapidly growing field.

While cation exchange as a methodology is not a commonly used means of materials synthesis at the industrial scale, the unique nature of its compositional tuning lends it to isolation of novel materials difficult to otherwise produce, often with a high degree of predictability. However, achieving an unexpected product can sometimes be more interesting than achieving an expected one. It is here in the subversion of assumptions that I pursued explanations of what makes or breaks a reliable synthesis. In addition to isolation of novel NCs with potential applications in efficient and greener technologies, a persistent goal has always been to further hone the synthetic toolkit of nano researchers.

As researchers with focus on computational, synthetic, and application goals continue to work towards advancing our society, it is my hope and that of the Macdonald lab that closer examination of methodology will help the field continue to grow together. In an ideal world, computational researchers will be able to propose a material of desired properties to synthetic chemists, who will already have a sufficient library of synthetic methods to quickly produce this product for applications testing. As a scientist, I aim for this thesis to further contribute towards that goal.

APPENDIX

A. Supplementary material for Chapter 2

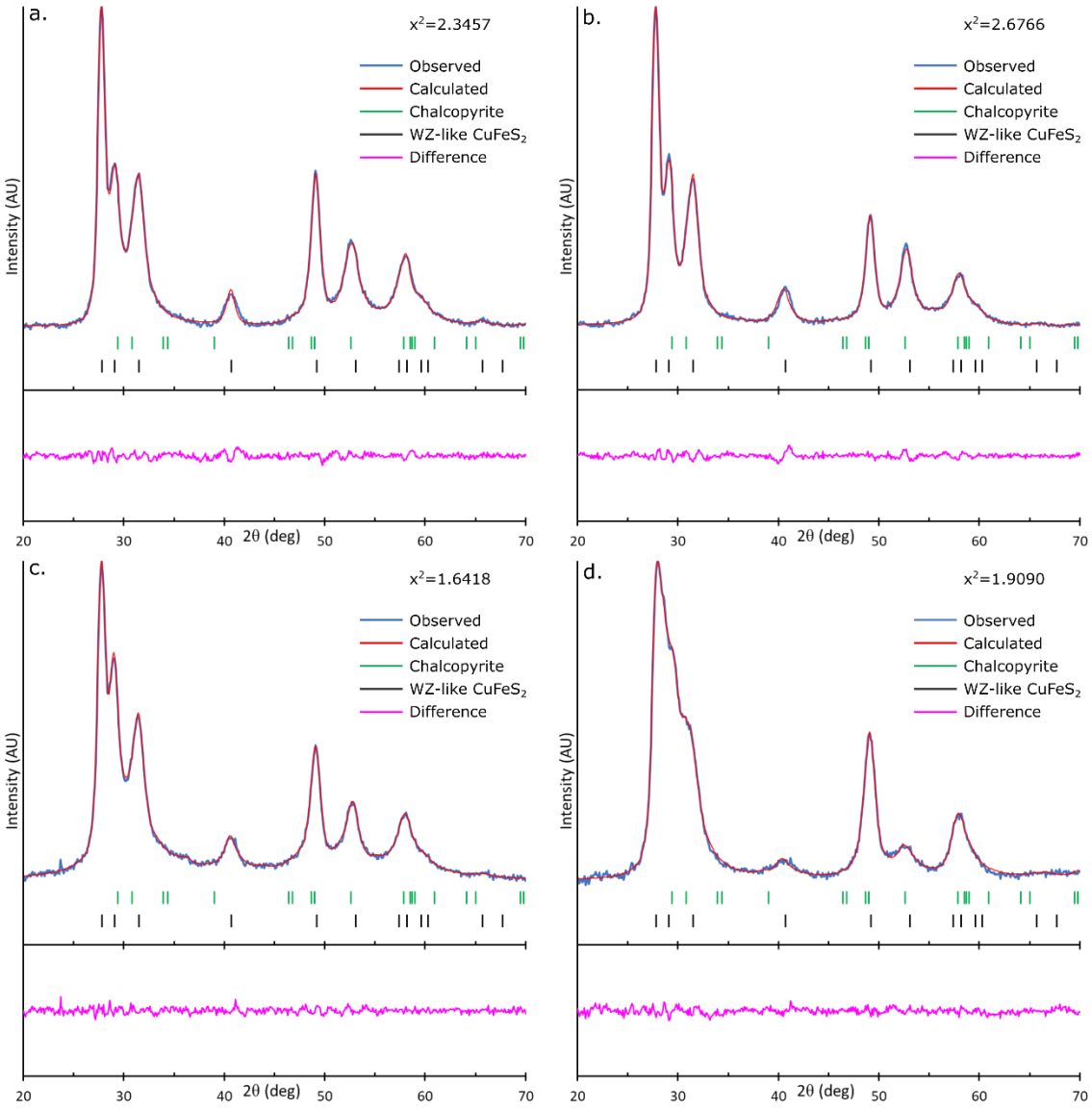

Figure A.1 Phase refinement of the pXRD patterns acquired for $CuFeS_2$ synthesized in the presence of a. trioctylamine, b. triphenylphosphite, c. triisopropyl phosphite, d. tris-4-chlorophenylphosphine. Refinements were performed using tetragonal chalcopyrite (AMCSD 0009476) and wurtzite-like (WZ-like) $CuFeS_2$ derived from a ZnS unit cell (AMCSD 0015179).

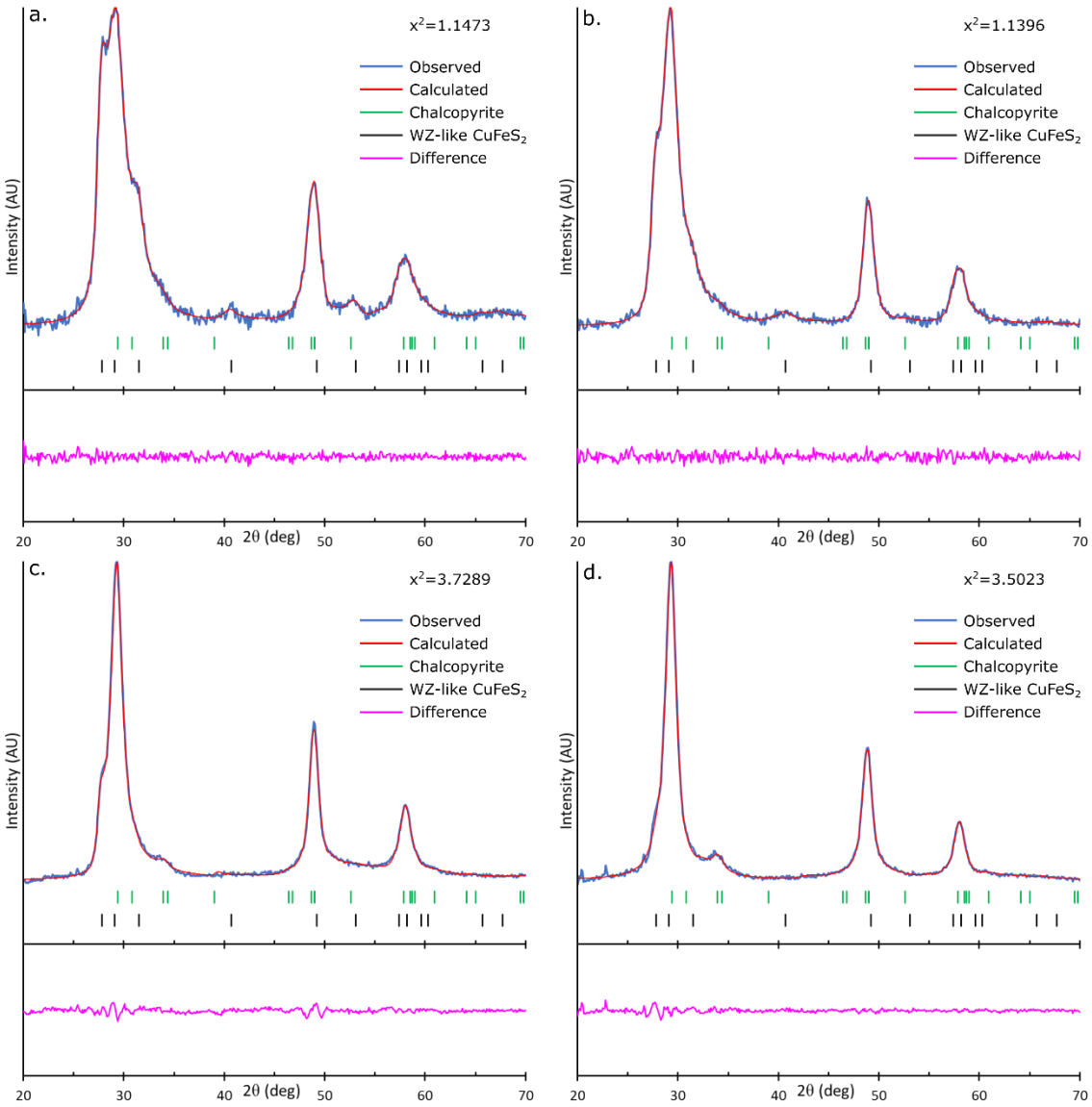

Figure A.2 Phase refinement of the pXRD patterns acquired for $CuFeS_2$ synthesized in the presence of a. triphenylphosphine, b. triethylphosphine, c. trioctylphosphine, d. tributylphosphine. Refinements were performed using tetragonal chalcopyrite (AMCSD 0009476) and WZ-like $CuFeS_2$ derived from a ZnS unit cell (AMCSD 0015179).

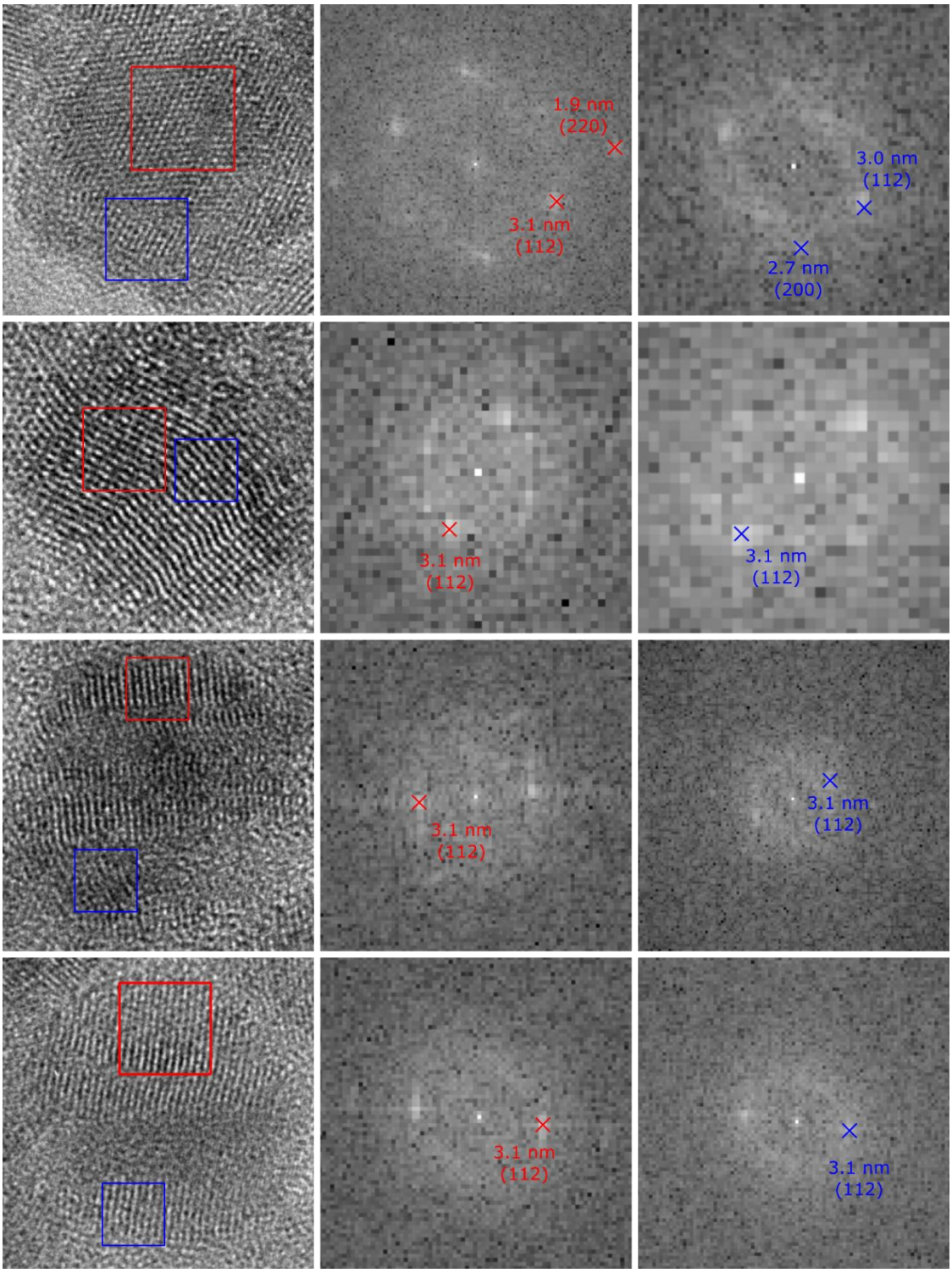

Figure A.3 (L) additional HR-TEM of examples of polycrystalline particles of $CuFeS_2$ synthesized in the presence of triphenylphosphine. (M and R) FFT of the boxed regions are indexed to CP $CuFeS_2$. Both CP [112] and WZ-like [002] $CuFeS_2$ reflections have similar spacings of 3.04 and 3.06 Å respectively. CP could be sometimes be conclusively identified.

B. Supplementary material for Chapter 3

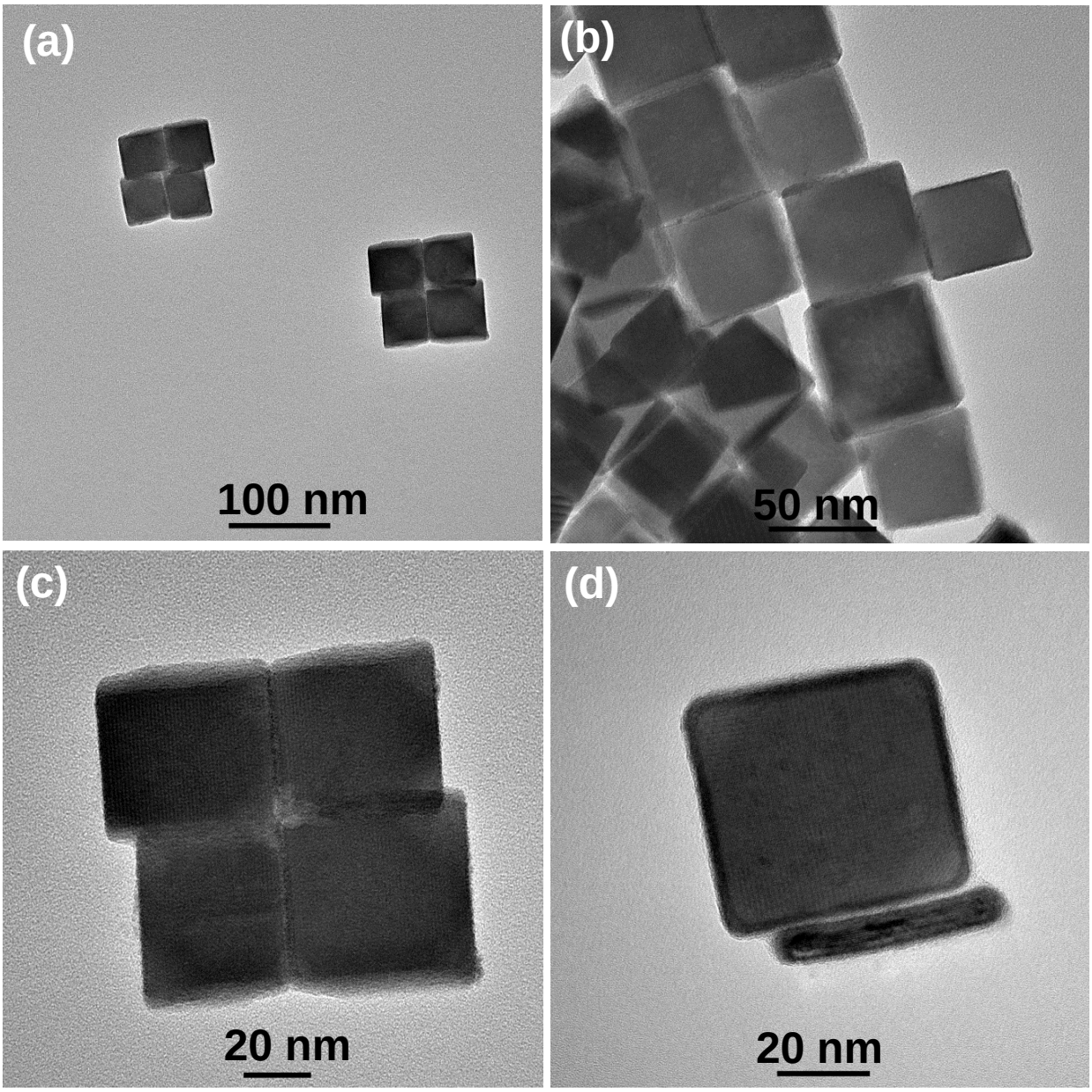

Figure B.1 Additional TEM images of pristine nanocuboids of π-SnS.

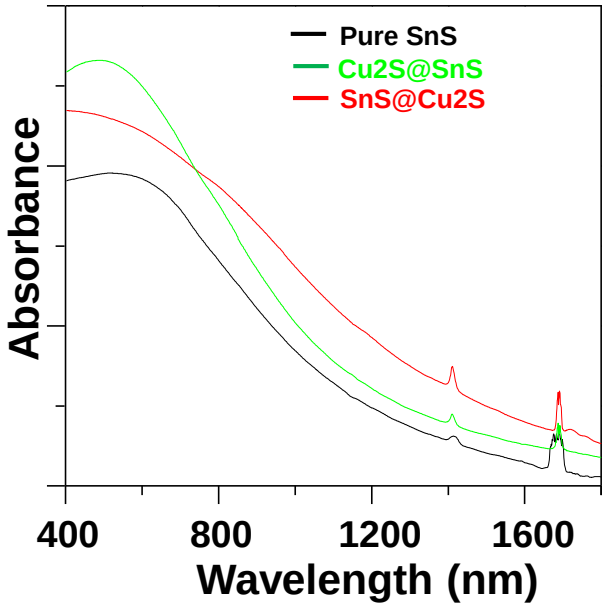

Figure B.2 UV-vis of the aliquots collected at the different stages of the cation exchange reaction. It should be noted that no fluorescence was observed for the products.

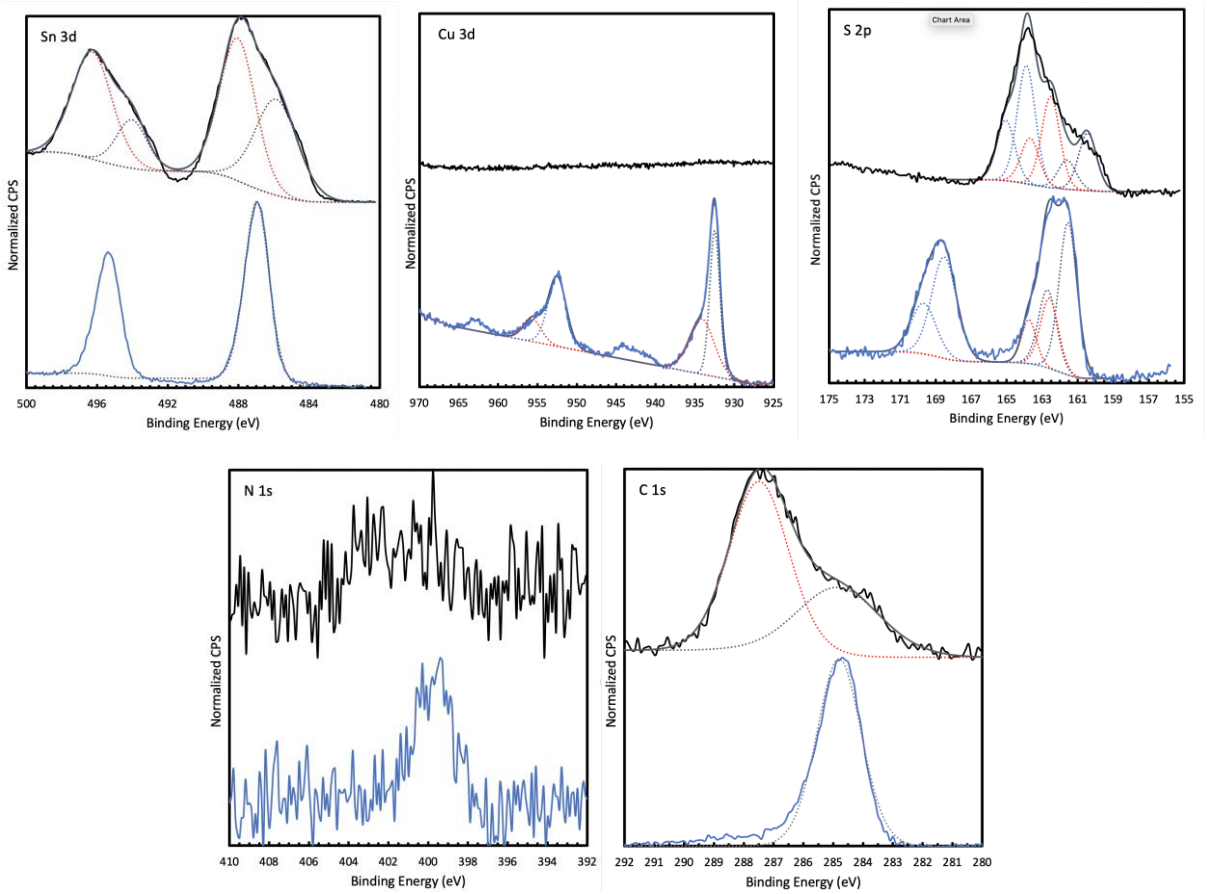

Figure B.3 HR-XPS of the p-SnS Cubes (black, top) and p-SnS@Cu-Sn-S (Blue Bottom). Fittings are given in dotted lines with spin-orbit couples in matching colors. The fitting sums are in dark grey solid. S 2p spin orbit couples were given the constraints: position splitting of 1.16 eV, area constraints of the ½ peak being of 0.511 times that of the 3/2 peak, and the FWHM of the couples were constrained to match.

The XPS of the p-SnS cubes is consistent with previous descriptions. The Sn 3d shows broad signals for the $3d_{5/2}$ and $3d_{3/2}$ couples indicating more than one chemical environment. The low binding energy component (485.8 eV & 494.1 eV) is assigned to p-Sn(II)S.[178] The high binding energy component (488.4 eV & 496.2 eV) is sufficiently high to be assigned to Sn(IV) oxide rather than a Sn(IV) sulfide.[179] The sulfur signal is also very broad with spin orbit couples at 160.4 eV & 161.8 eV, 162.5 eV & 163.9 eV, 169.0 eV & 165.1 eV. While difficult to assign specifically, especially since the O 1s peak is contaminated by the substrate (not included), the signal is likely from mixture of Sn(II), Sn(IV) sulfide and oxy-sulfide environments. Such oxidation is likely a result of exposure of the cubes to atmosphere before XPS analysis. A small nitrogen signal is present due to the amine surface ligands.

For the p-SnS@Cu-Sn-S, the Cu:Sn:S ratio on the surface was found to be ~1:0.9:1.7. Like the p-SnS cubes, there is also evidence of significant oxidation on the surface. The 1.65 eV FWHM of the Sn $3d_{5/2}$ peak is consistent with either one or at best a set of chemically similar species. The peaks of the Sn 3d spin orbit couple were centered at 486.9 eV & 395.3eV. These values are similar to that of Cu_3SnS_4, more generally Sn(IV)sulfides.[123,179] The S signal could be fitted to

three components. Two spin-orbit couples at 161.5eV & 162.6 eV and 162.5 eV & 163.6 eV are consistent with the sulfides of Sn(II) and Sn(IV). An additional broad signal at high binding energy (168.3 eV & 169.6 eV) can be assigned to sulfate. The copper 2p has strong signals at 932.5 eV & 952.3 eV indicative of Cu(I) and is similar to those seen in mixed cation phases such as Cu_3SnS_4.[123] A second, high binding energy component at 934.4eV and 935.4 eV and along with satellite peaks at 943.2 eV and 962.5 are indicative of Cu(II). Taken together, the evidence suggests that the amorphous shell has chemical speciation most similar to mixed phases such as $Cu^{1+}{}_3Sn^{4+}S_4$, but is also prone to surface oxidation of the Cu and S in the atmosphere to include Cu(II) and sulfate.

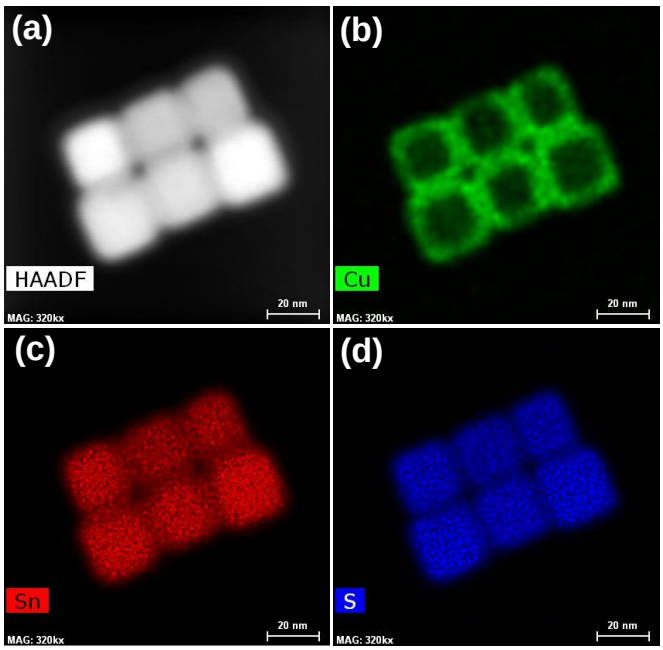

Figure B.4 High Angle Annular Dark Field- Scanning Transmission Electron Microcopy (HAADF-STEM) image of the nanocuboids (23±2 nm, n = 120) collected at 110 °C (b-d) EDS elemental mapping.

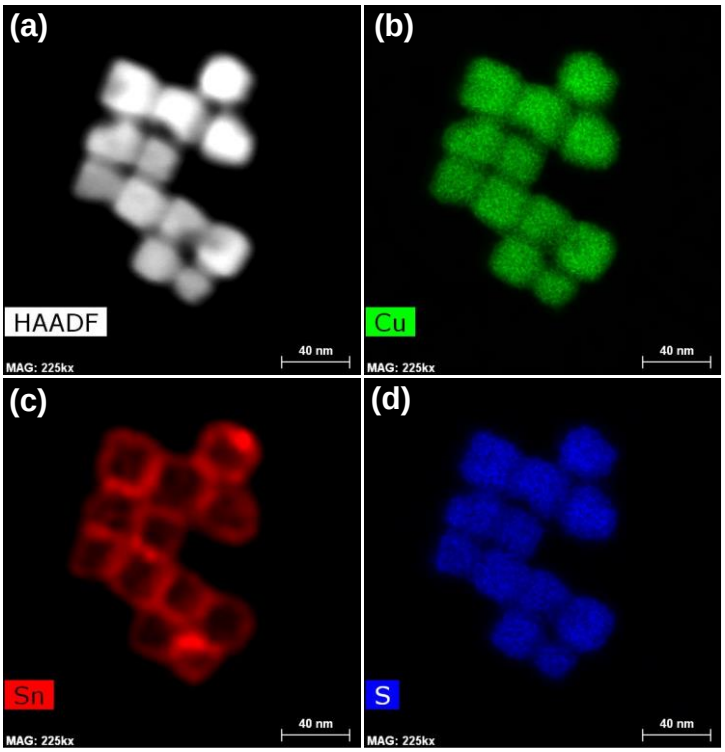

Figure B.5 High Angle Annular Dark Field- Scanning Transmission Electron Microcopy (HAADF-STEM) image of the nanocuboids (23±2 nm, n = 120) collected at 170 °C (b-d) EDS elemental mapping.

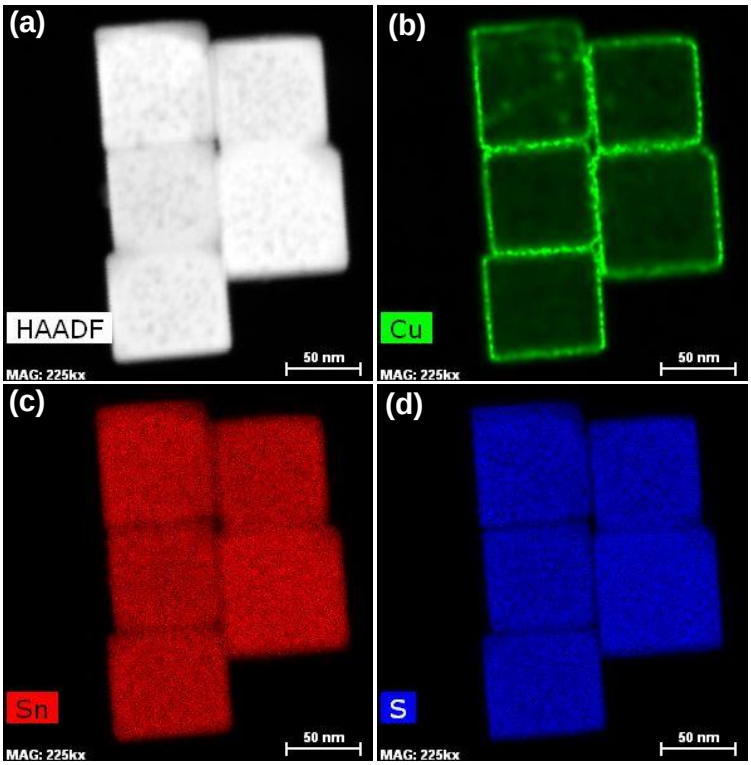

Figure B.6 High Angle Annular Dark Field- Scanning Transmission Electron Microcopy (HAADF-STEM) image of the nanocuboids (78±10 nm, n = 120) collected at 135 °C (b-d) EDS elemental mapping.

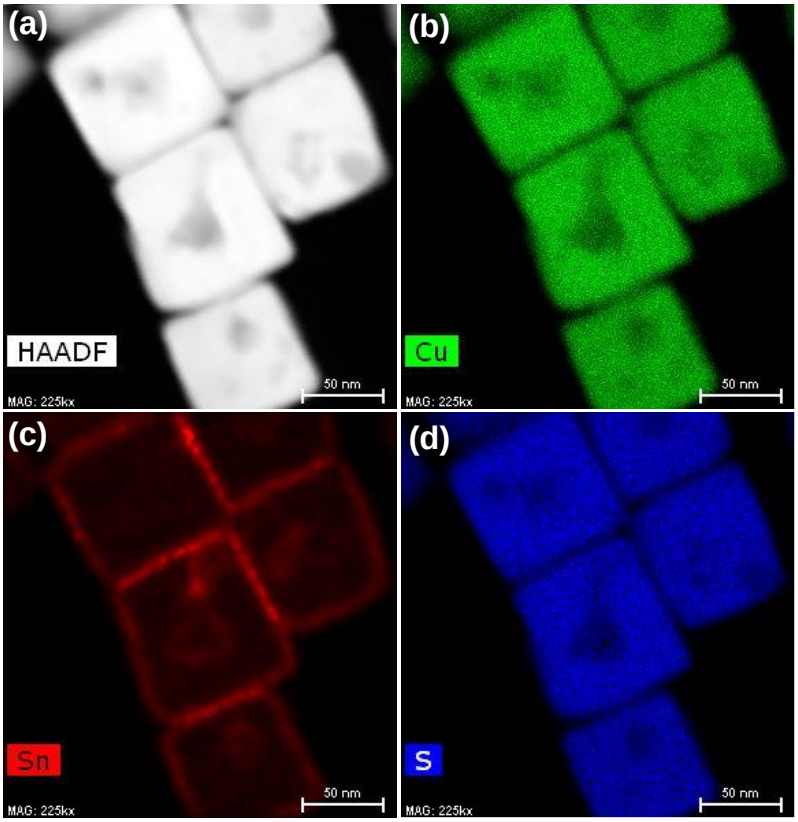

Figure B.7 High Angle Annular Dark Field- Scanning Transmission Electron Microcopy (HAADF-STEM) image of the nanocuboids (78±10 nm, n = 120) collected at 170 °C (b-d) EDS elemental mapping.

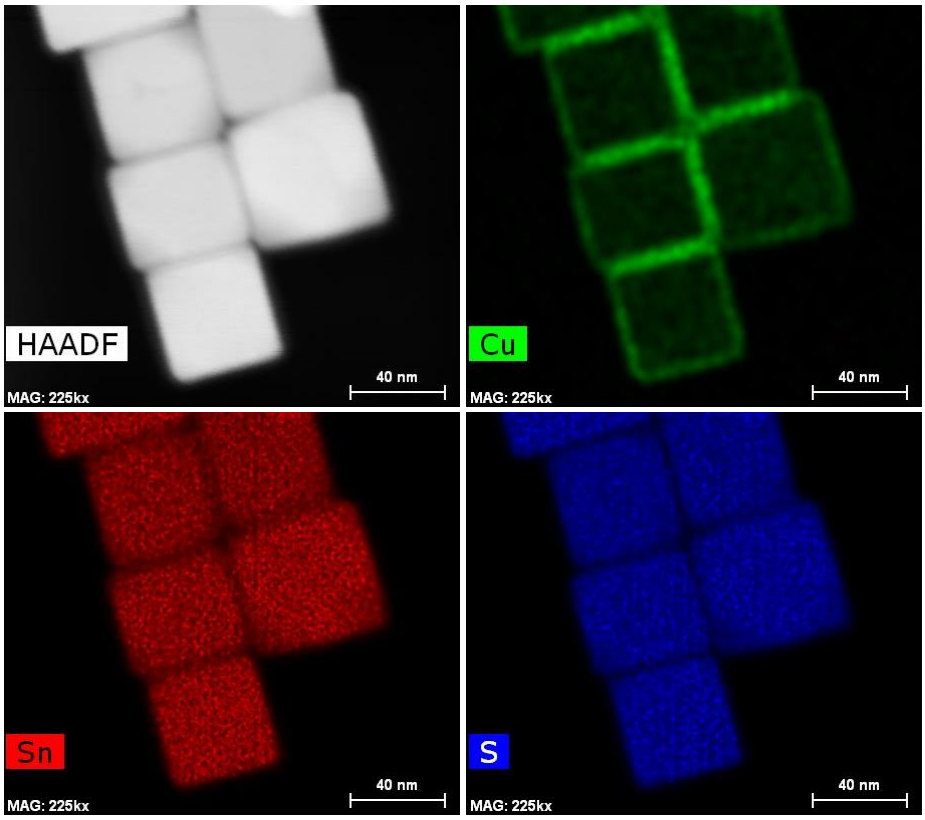

Figure B.8 HAADF image and elemental mapping of an aliquot with prolonged time (1hr) of annealing at 135 °C.

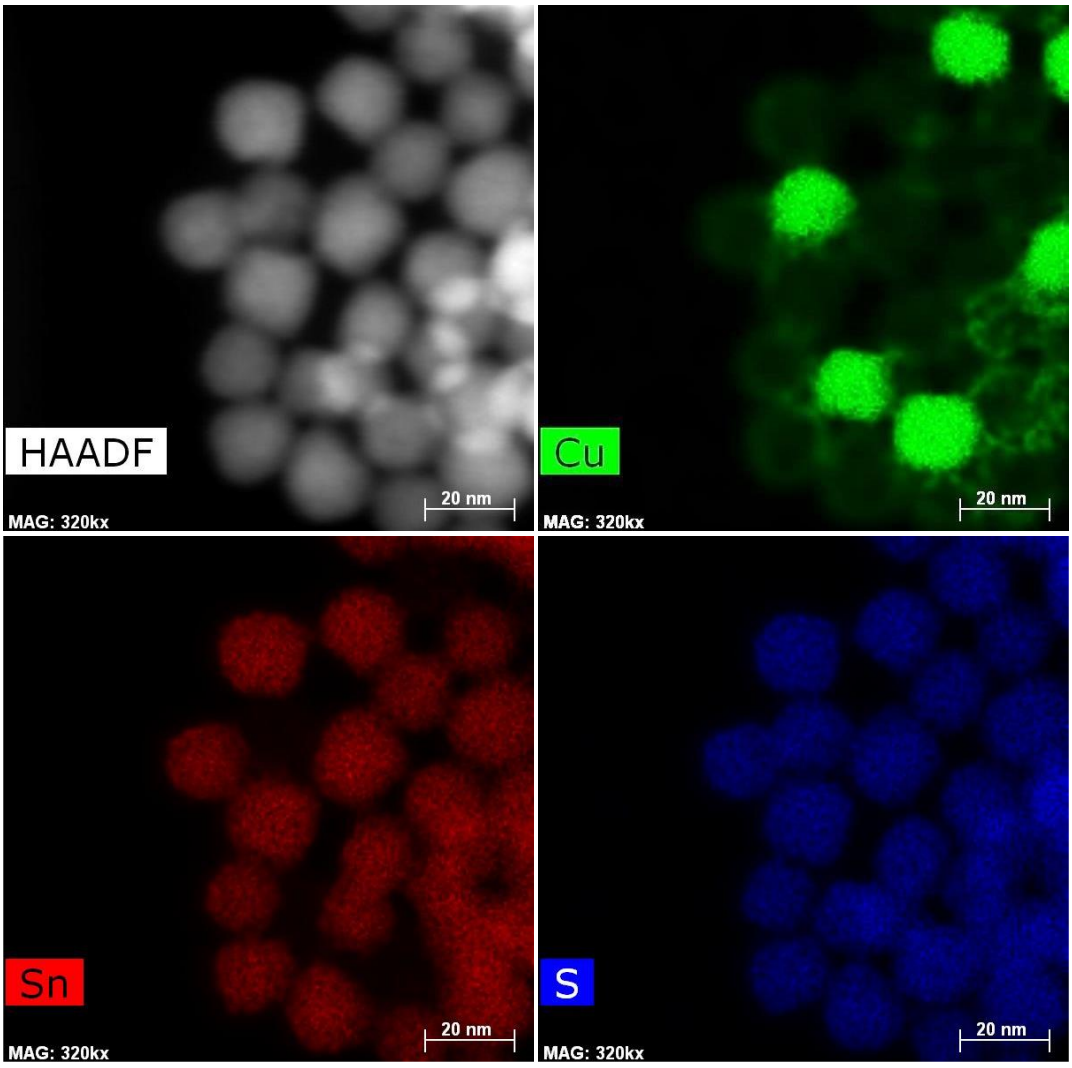

Figure B.9 HADAAF image and elemental mapping of an aliquot collected at 145 °C for a typical cation exchange reaction with smaller size π-SnS nanocuboids. It shows a mixture of both types of core@shell nanocuboids.

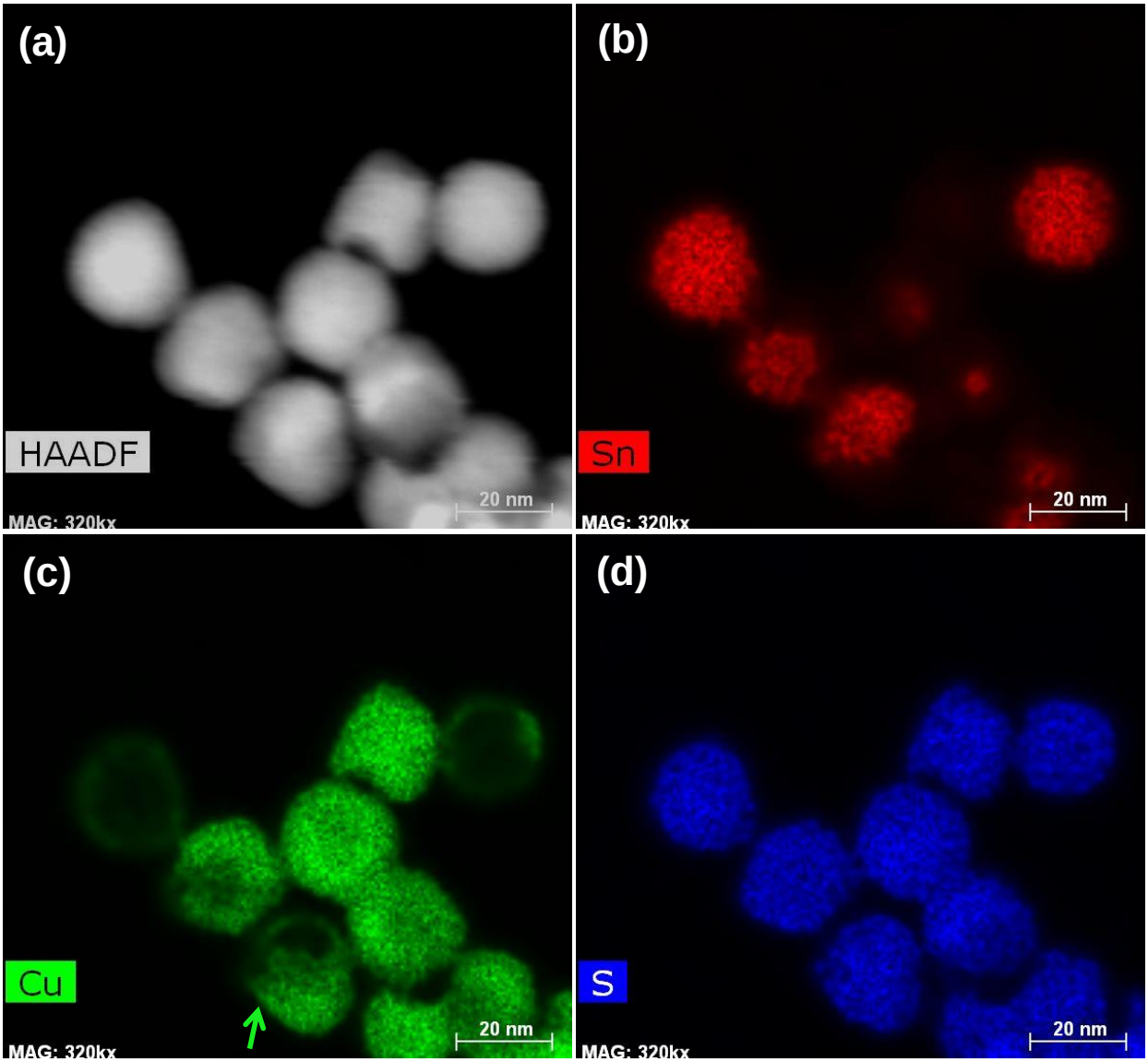

Figure B.10 HADAAF image and elemental mapping of an aliquot collected at 125 °C for a typical cation exchange reaction with smaller size of pristine π-SnS nanocuboids. It shows a mixture of both types of core-shell nanocuboids along with a pseudonanocube with Cu^{+} approached halfway shown in panel (C), while taking over the core of the π-SnS nanocuboids.

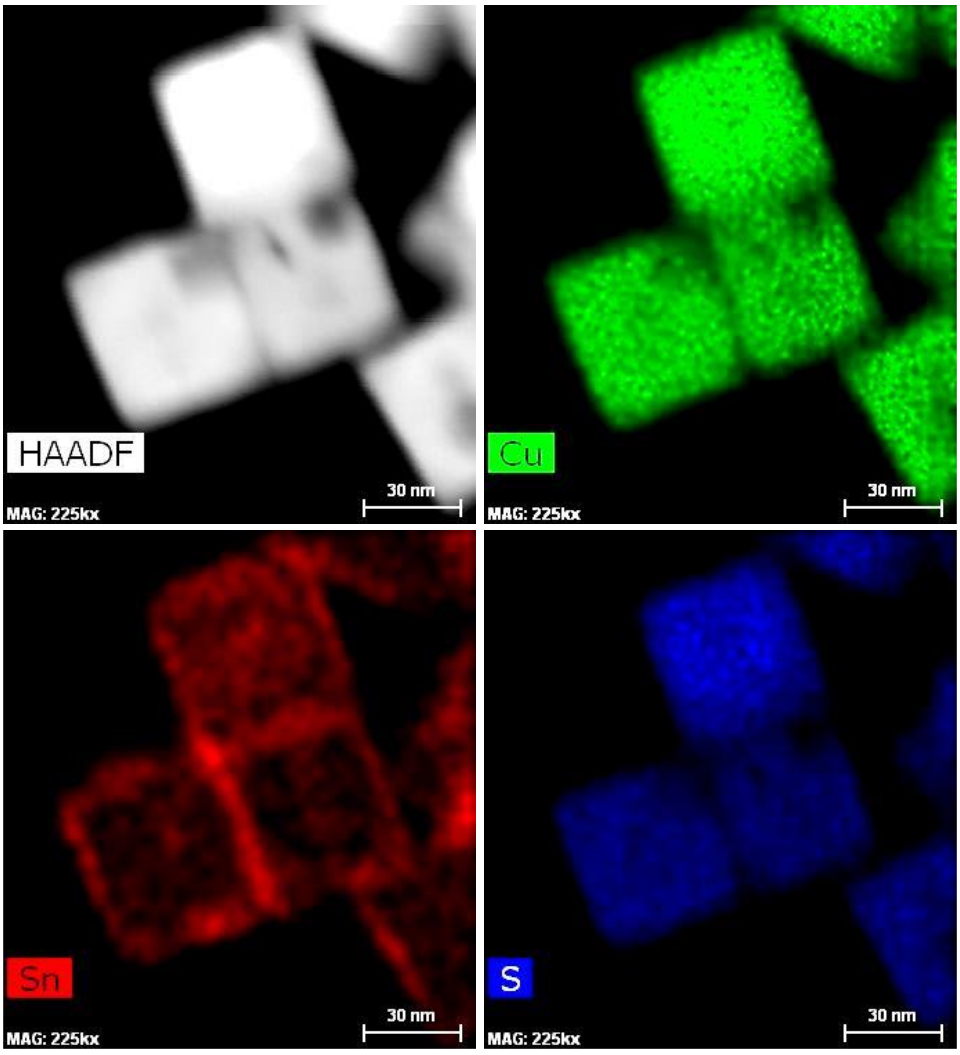

Figure B.11 HAADF image and elemental mapping of an aliquot collected at 160 °C for a typical cation exchange reaction with higher amount of Cu^{+} (1.5 times than the optimized amount).

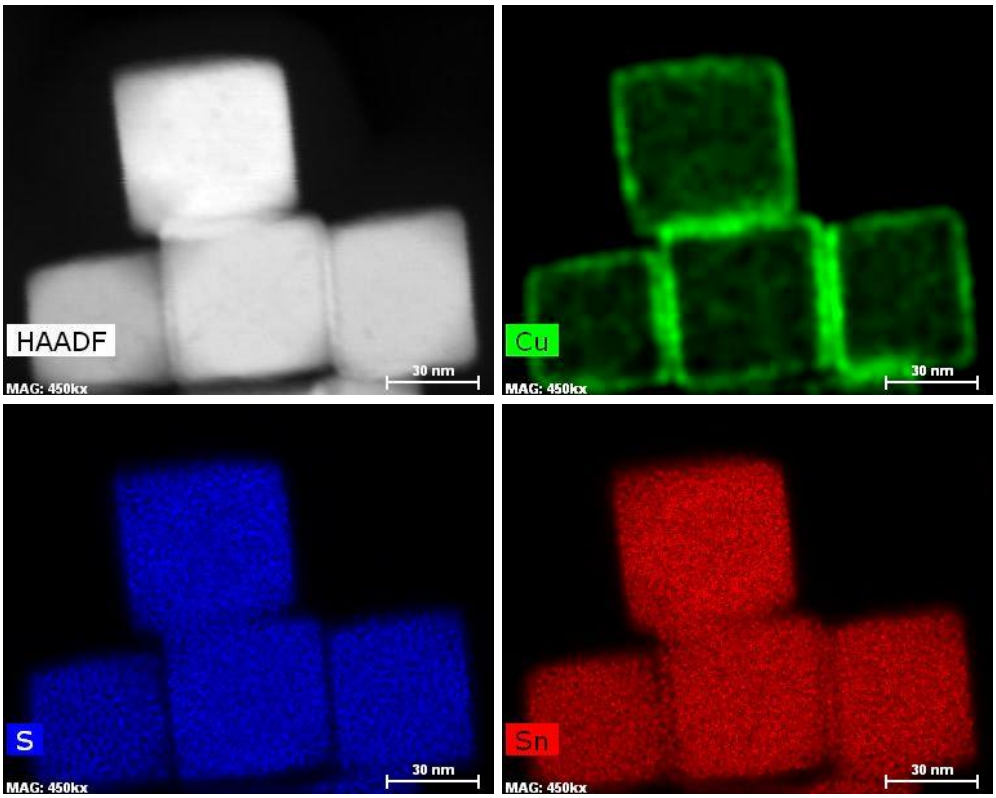

Figure B.12 HADAAF image and elemental mapping of an aliquot collected at 170 °C for a typical cation exchange reaction with addition of 0.5 mL of extra TBP prior to the addition of Cu^{+}-oleylamine solution into the reaction mixture. It shows the formation of only π-SnS@Cu-Sn-S.

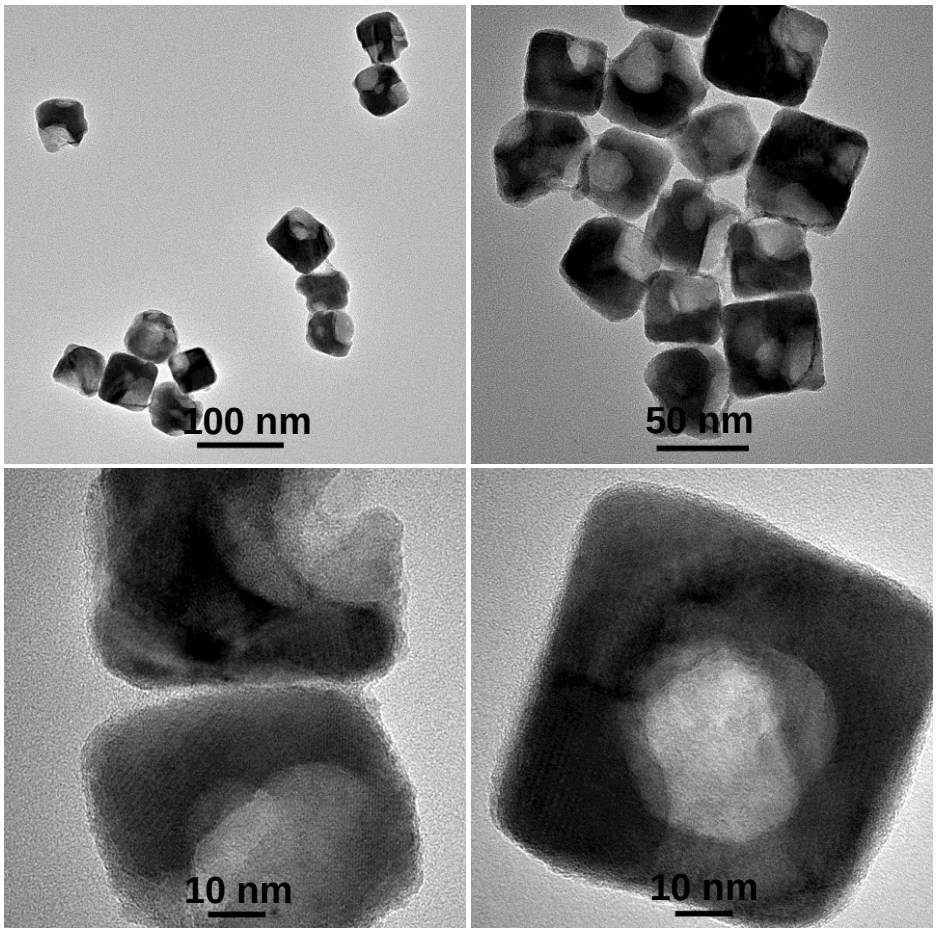

Figure B.13 Additional TEM images of Cu1.8S@Sn-Cu-S obtained after annealing for 15 minutes at 170 °C.

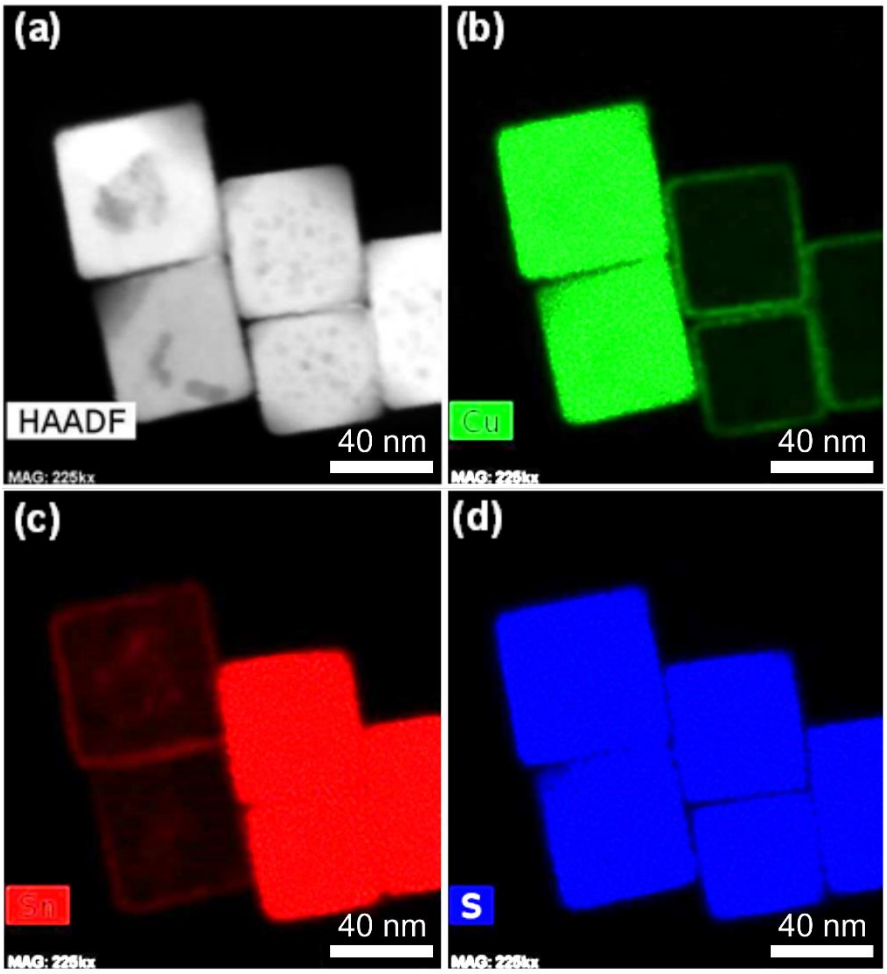

Figure B.14 Figure 7 of the manuscript photo editing of color brilliance to highlight the shelling observed. EDS elemental mapping of an aliquot collected at 155 °C.

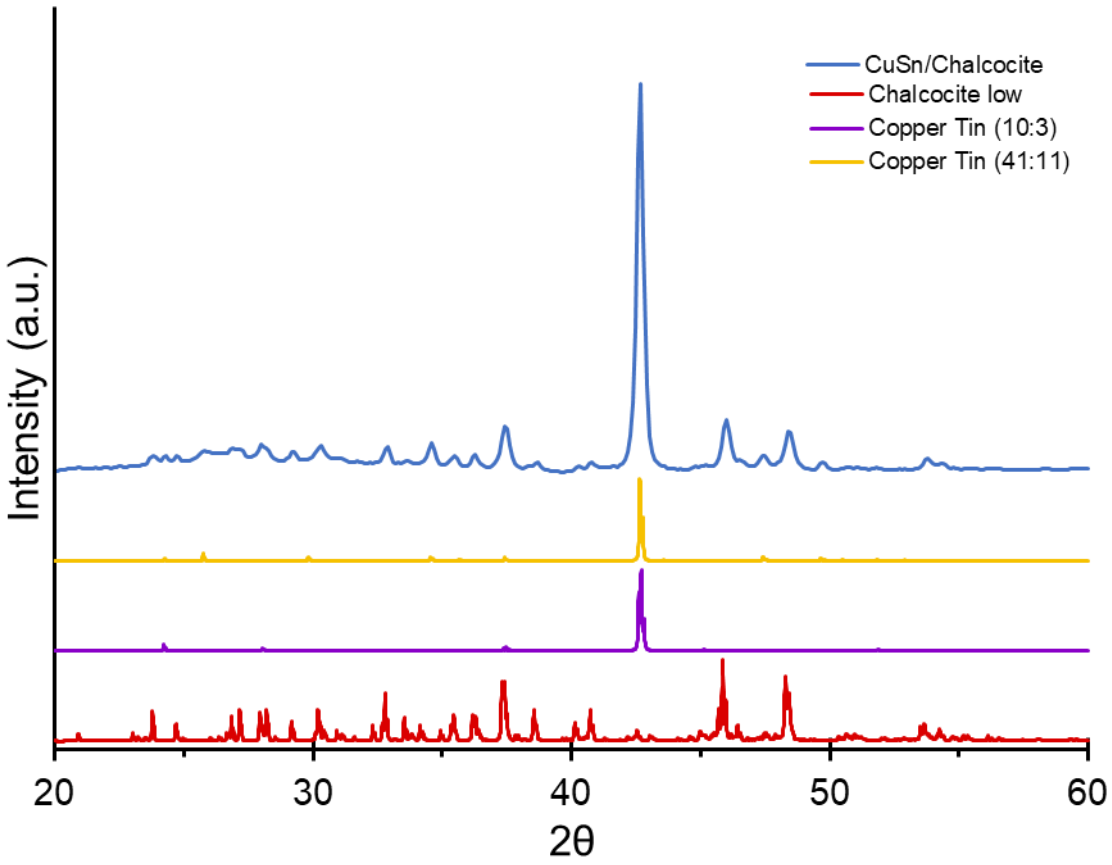

Figure B.15 Powder X-ray diffraction of the SnS/Cu^{+} cation exchange solution to 300 °C. Product primarily contains low chalcocite and copper tin alloys with no shelled SnS cubes formed or host nanocuboids remaining. Reference patterns are included.

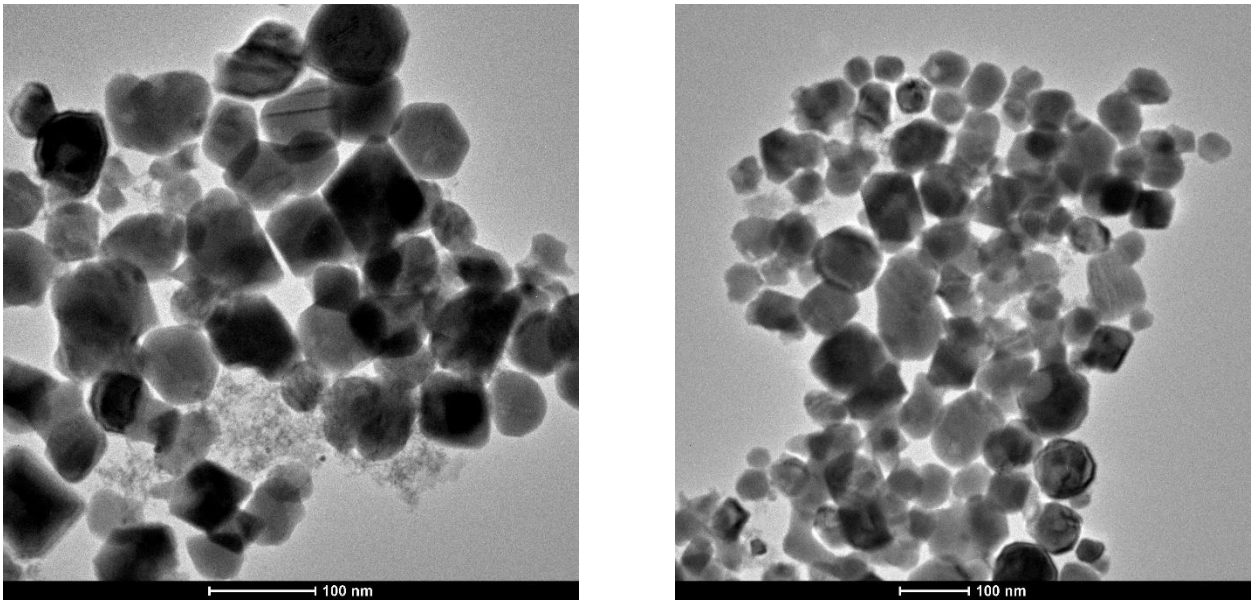

Figure B.16 TEM of chalcocite low/copper tin mixed product. Variable sizes and morphologies present indicate both ripening during reaction as well as new nucleation events. No core@shell structures or particles possessing voids were observed.

C. Supplementary material for Chapter 4

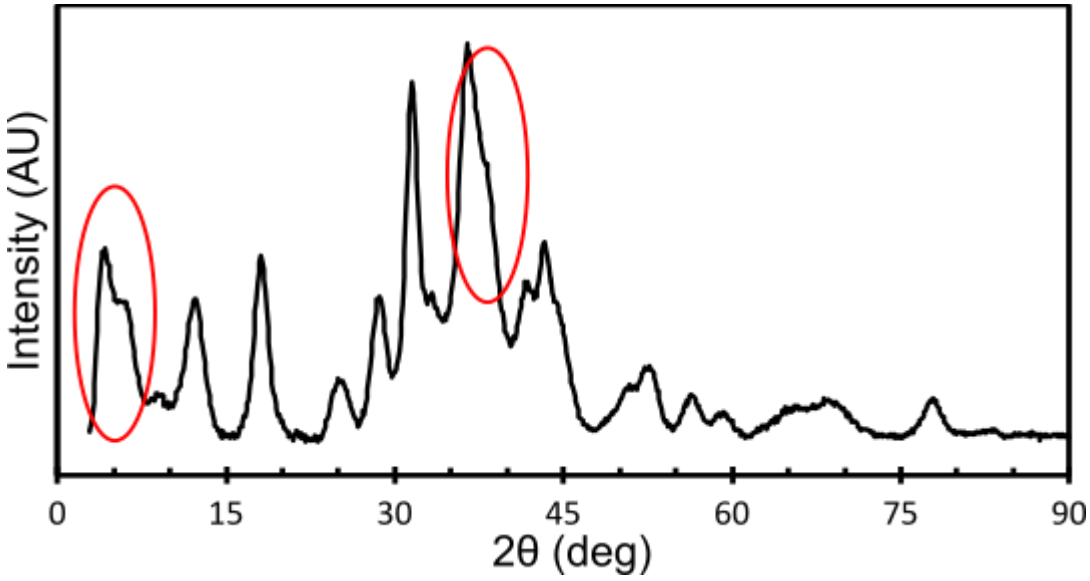

Figure C.1 Powder X-ray diffraction of $Cu_2Au_5Se_3$ nanodisks. Red circles indicate artifact signals observed due to (L) stacking of nanodisks during dropcasting and (R) preferred orientation of the product on the sample holder.

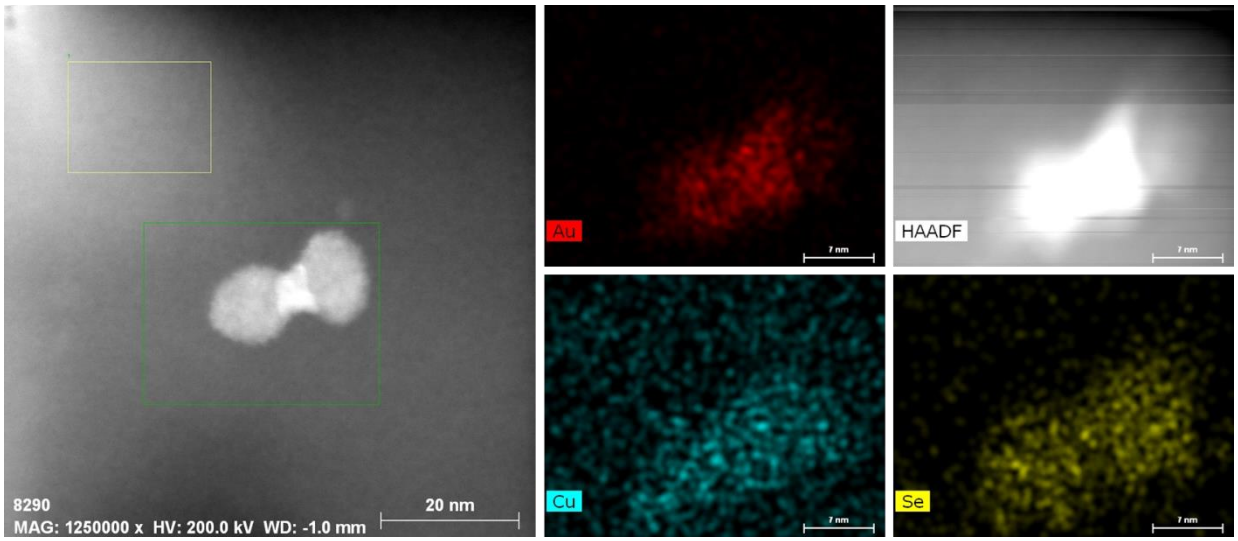

Figure C.2 TEM-HAADF of $Cu_2Au_5Se_3$ nanodisks. Degradation is readily observed over extended rasterized scans in an effort to obtain elemental mapping data.

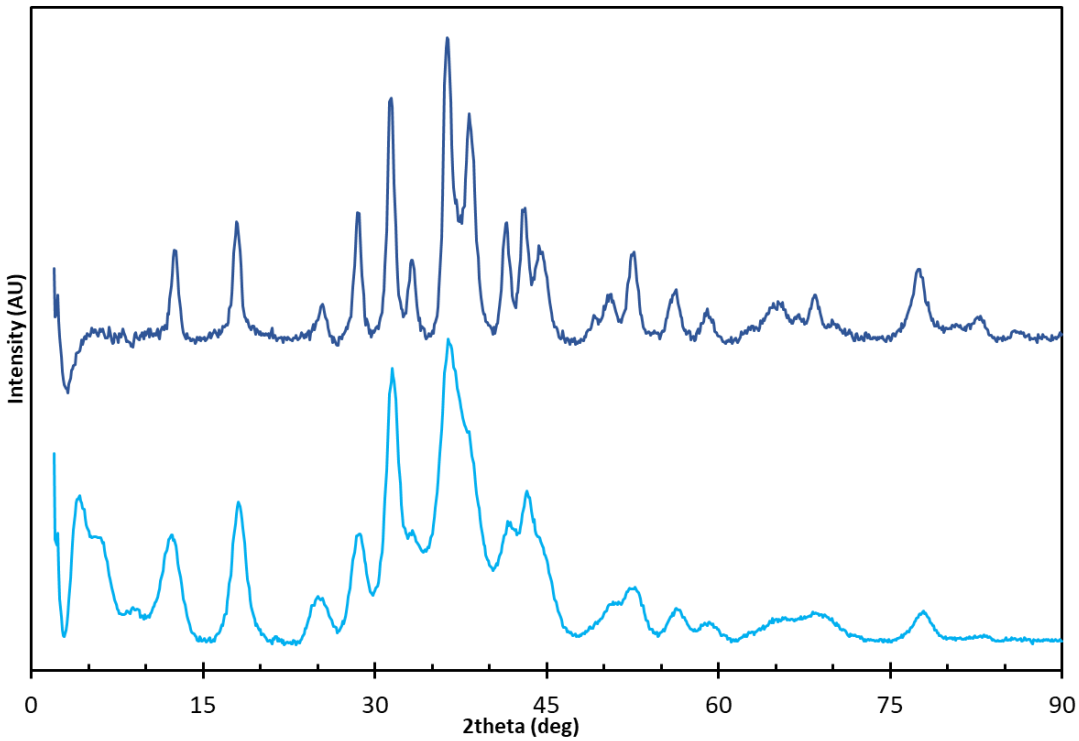

Figure C.3 Powder X-ray diffraction of $Cu_2Au_5Se_3$ nanodisks (bottom) and quasi-spheres (top). The morphology related artifacts observed sub-10 degrees are no longer present in the quasi-spherical sample. Furthermore, the peak at ~39 degrees is now discretely resolved.

Figure C.4 ^{1}H NMR of DD_2Se_2

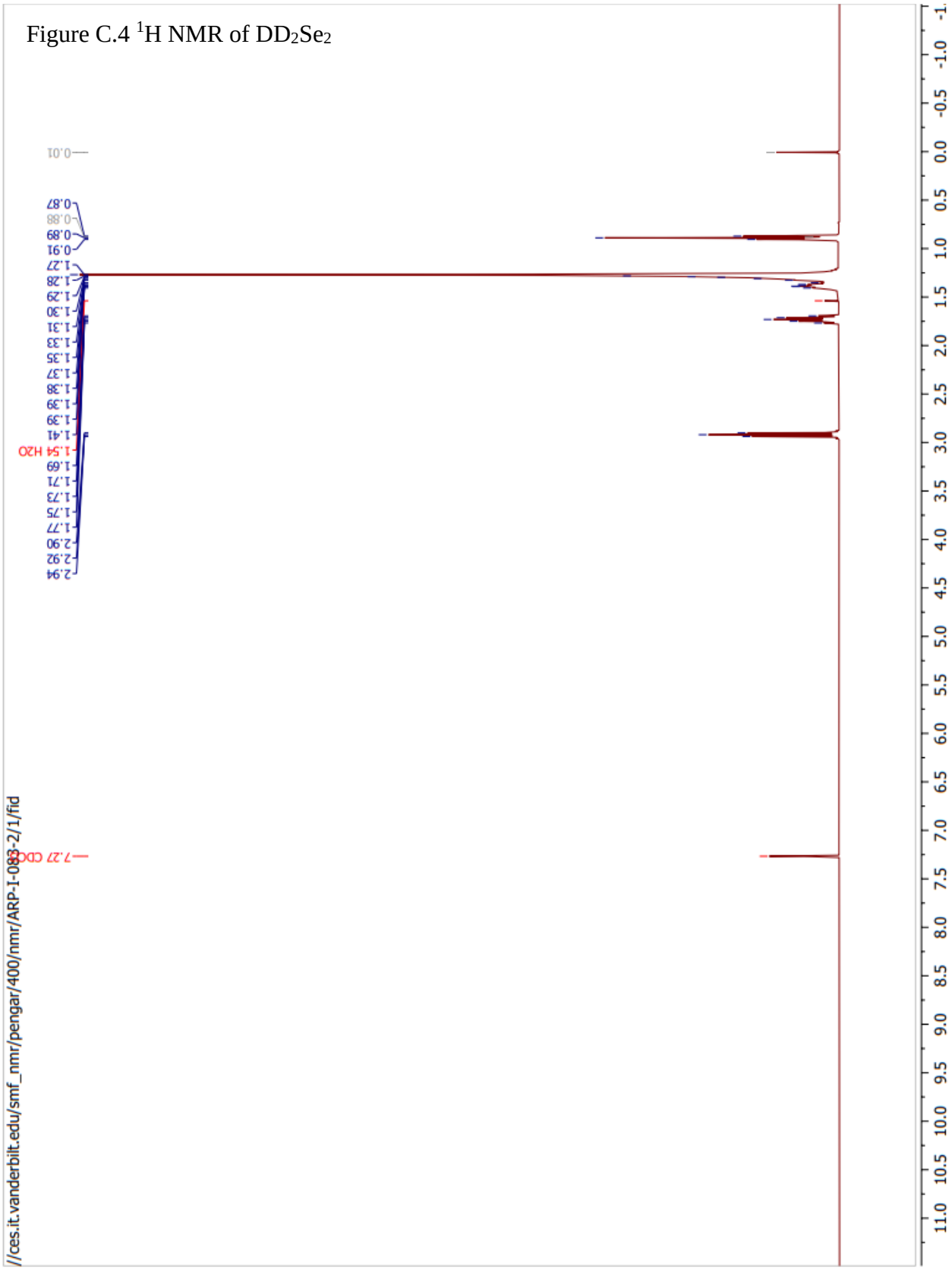

Figure C.5 ^{77}Se NMR of DD_2Se_2

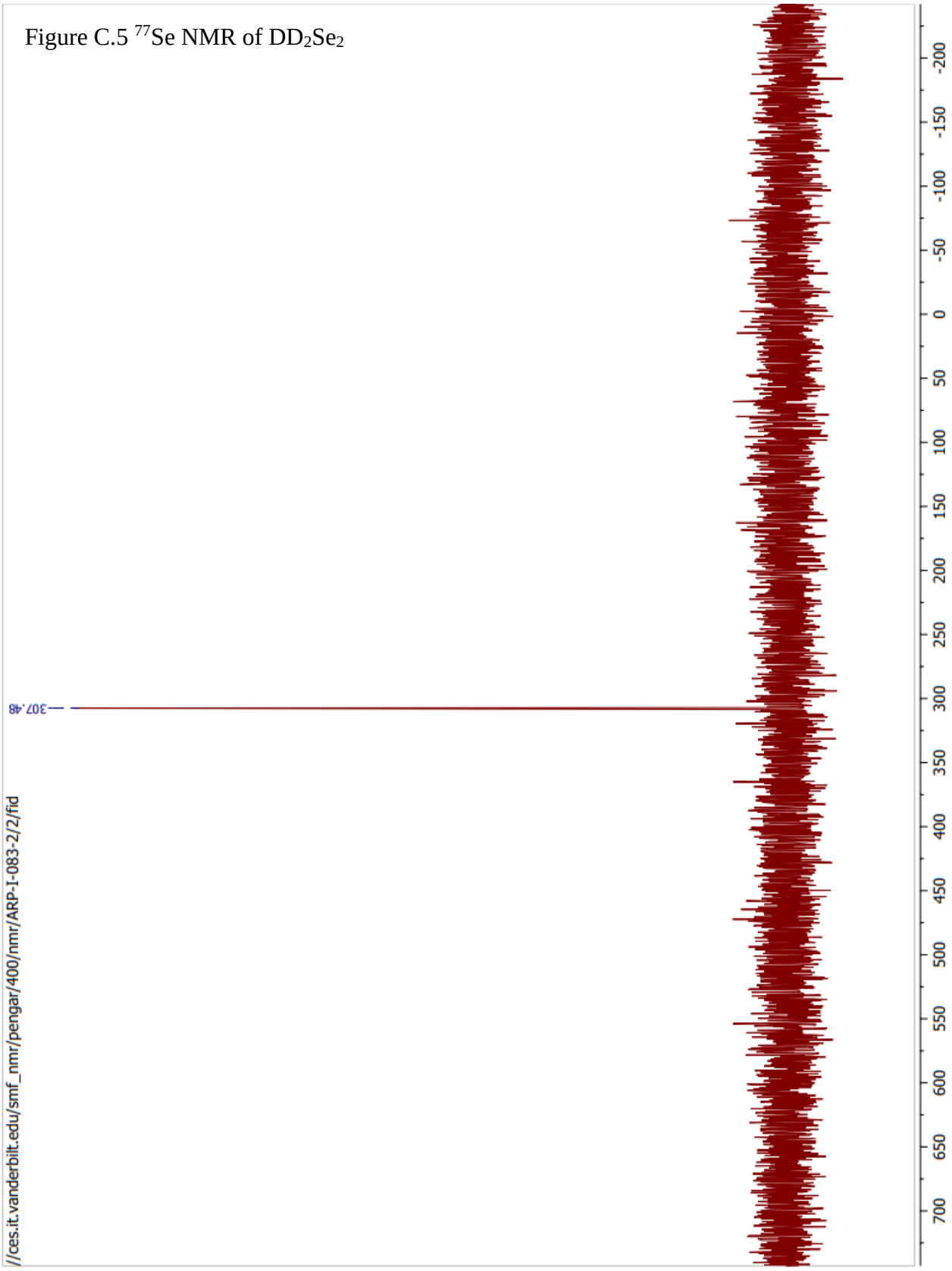

D. Adapted Publications

Parts of this dissertation have been published previously, copyright approval has been obtained for reproduced figures or text in the following chapters:

Chapter II

Reprinted with permission from Sharp, C. G.; Leach, A. D. P.; Macdonald, J. E. Nano Lett. 2020, 20, 12, 8556–8562. Copyright 2020 American Chemical Society.

Chapter III

Reprinted with permission from Sarkar, S.; Sharp, C. G.; Macdonald, J. E. Chem. Mater. 2021, 33, 8, 3011–3019. Copyright 2021 American Chemical Society. First authorship is shared with Suresh Sarkar and his permission was granted to publish this work herein.

REFERENCES

1. Barbier, E. B. The Evolution of Economic Views on Natural Resource Scarcity. *Rev Environ Econ Policy* **15**, 24–44 (2021).
2. Yokoi, R., Nansai, K., Hatayama, H. & Motoshita, M. Significance of country-specific context in metal scarcity assessment from a perspective of short-term mining capacity. *Resour Conserv Recycl* **166**, 1–9 (2021).
3. Håkansson, A. What is overconsumption? – A step towards a common understanding. *Int J Consum Stud* **38**, 692–700 (2014).
4. Cleveland, C. J. An exploration of alternative measures of natural resource scarcity: the case of petroleum resources in the U.S. *Ecological Economics* **7**, 123–157 (1993).
5. Goodenough, J. B. Energy storage materials: A perspective. *Energy Storage Mater* **1**, 158–161 (2015).
6. Mall, R. K., Gupta, A., Singh, R., Singh, R. S. & Rathore, L. S. Water resources and climate change: An Indian perspective. *Curr Sci* **90**, 1610–1626 (2006).
7. Brekkel, L. D. *Climate Change and Water Resources Management: A Federal Perspective*. (DIANE Publishing Company, 2009).
8. Samarth, N. Quantum materials discovery from a synthesis perspective. *Nat Mater* **16**, 1068–1076 (2017).
9. Goldstein, A. N., Echer, C. M. & Alivisatos, A. P. Melting in Semiconductor Nanocrystals. *Science (1979)* **256**, 1425–1427 (1992).
10. Buffat, P. & Borel, J.-P. Size effect on the melting temperature of gold partlclese. *Phys Rev A (Coll Park)* **13**, 2287–2298 (1976).
11. Scholes, G. D. & Rumbles, G. Excitons in nanoscale systems. *Nat Mater* **5**, 683–696 (2006).
12. Zhou, W. & Lee, J. Y. Particle size effects in Pd-catalyzed electrooxidation of formic acid. *J. Phys. Chem. C* **112**, 3789–3793 (2008).
13. Chacón, G. & Dupont, J. Arene Hydrogenation by Metal Nanoparticles in Ionic Liquids. *ChemCatChem* **11**, 333–341 (2019).
14. Zhang, H. *et al.* Carbon-wrapped Fe–Ni bimetallic nanoparticle-catalyzed Friedel–Crafts acylation for green synthesis of aromatic ketones. *Catal. Sci. Technol.* **11**, 7943–7954 (2021).
15. Clunan, A. & Rodine-Hardy, K. *Nanotechnology in a Globalized World Strategic Assessments of an Emerging Technology*. (2014).
16. Moriarty, P. Nanostructured materials. *Reports on Progress in Physics* **64**, 297 (2001).

17. Liu, K. *et al.* Superamphiphiles Based on Directional Charge-Transfer Interactions: From Supramolecular Engineering to Well-Defined Nanostructures. *Angew. Chem. Int. Ed.* **50**, 4952–4956 (2011).

18. Wang, Y. *et al.* Ordered Single-Crystalline Anatase TiO_2 Nanorod Clusters Planted on Graphene for Fast Charge Transfer in Photoelectrochemical Solar Cells. *Small* **13**, 1700793 (2017).

19. Guerrini, G., Magrì, D., Gioria, S., Medaglini, D. & Calzolai, L. Characterization of nanoparticles-based vaccines for COVID-19. *Nat Nanotechnol* **17**, 570–576 (2022).

20. Bayda, S., Adeel, M., Tuccinardi, T., Cordani, M. & Rizzolio, F. The History of Nanoscience and Nanotechnology: From Chemical–Physical Applications to Nanomedicine. *Molecules 2020, Vol. 25, Page 112* **25**, 112 (2019).

21. Anker, J. N. *et al.* Biosensing with plasmonic nanosensors. *Nat Mater* **7**, 442–453 (2008).

22. Agrawal, A. *et al.* Localized Surface Plasmon Resonance in Semiconductor Nanocrystals. *Chem Rev* **118**, 3121–3207 (2018).

23. Faraday, M. The Bakerian Lecture - Experimental relations of gold (and other metals) to light. *Philos Trans R Soc Lond* **147**, 145–181 (1857).

24. Brus, L. E. A simple model for the ionization potential, electron affinity, and aqueous redox potentials of small semiconductor crystallites. *J Chem Phys* **79**, 5566–5571 (1998).

25. Brus, L. E. Electron–electron and electron-hole interactions in small semiconductor crystallites: The size dependence of the lowest excited electronic state. *J Chem Phys* **80**, 4403–4409 (1998).

26. Scioli Montoto, S., Muraca, G. & Ruiz, M. E. Solid Lipid Nanoparticles for Drug Delivery: Pharmacological and Biopharmaceutical Aspects. *Front Mol Biosci* **7**, 319 (2020).

27. Xu, L. *et al.* Lipid Nanoparticles for Drug Delivery. *Adv Nanobiomed Res* **2**, 2100109 (2022).

28. Hou, X., Zaks, T., Langer, R. & Dong, Y. Lipid nanoparticles for mRNA delivery. *Nat Rev Mater* **6**, 1078–1094 (2021).

29. Cui, K. & Wardle, B. L. Breakdown of Native Oxide Enables Multifunctional, Free-Form Carbon Nanotube-Metal Hierarchical Architectures. *ACS Appl Mater Interfaces* **11**, 35212–35220 (2019).

30. Jackson, J. J. *et al.* Pulsed growth of vertically aligned nanotube arrays with variable density. *ACS Nano* **4**, 7573–7581 (2010).

31. Ekimov, A. I. *et al.* Absorption and intensity-dependent photoluminescence measurements on CdSe quantum dots: assignment of the first electronic transitions: erratum. *J. Opt. Soc. Am. B* **10**, 100–107 (1993).

32. Koole, R., Groeneveld, E., Vanmaekelbergh, D., Meijerink, A. & De Mello Donegá, C. Size effects on semiconductor nanoparticles. in *Nanoparticles: Workhorses of Nanoscience* 13–51 (Springer-Verlag Berlin Heidelberg, 2014). doi:10.1007/978-3-662-44823-6_2/FIGURES/23.

33. Sumanth Kumar, D., Jai Kumar, B. & Mahesh, H. M. Quantum Nanostructures (QDs): An Overview. in *Synthesis of Inorganic Nanomaterials: Advances and Key Technologies* 59–88 (Elsevier, 2018). doi:10.1016/B978-0-08-101975-7.00003-8.

34. Thomson, J. W., Nagashima, K., MacDonald, P. M. & Ozin, G. A. From sulfur-amine solutions to metal sulfide nanocrystals: peering into the oleylamine-sulfur black box. *J Am Chem Soc* **133**, 5036–5041 (2011).

35. Sobol, O., Gadot, E., Wang, Y., Weinstock, I. A. & Meshi, L. Addressing a 'Black Box' of Bottom-Up Synthesis: Revealing the Structures of Growing Colloidal-Nanocrystal Nuclei. *Inorg Chem* **54**, 10521–10523 (2015).

36. La Mer, V. K. Nucleation in Phase Transitions. *Ind Eng Chem* **44**, 1270–1277 (2002).

37. La Mer, V. K. & Dinegar, R. H. Theory, Production and Mechanism of Formation of Monodispersed Hydrosols. *J Am Chem Soc* **72**, 4847–4854 (1950).

38. Abécassis, B. *et al.* Persistent nucleation and size dependent attachment kinetics produce monodisperse PbS nanocrystals. *Chem Sci* **13**, 4977–4983 (2022).

39. Huang, J., Kovalenko, M. v. & Talapin, D. v. Alkyl chains of surface ligands affect polytypism of CdSe nanocrystals and play an important role in the synthesis of anisotropic nanoheterostructures. *J Am Chem Soc* **132**, 15866–15868 (2010).

40. Mahler, B., Lequeux, N. & Dubertret, B. Ligand-controlled polytypism of thick-shell CdSe/CdS nanocrystals. *J Am Chem Soc* **132**, 953–959 (2010).

41. Soni, U., Arora, V. & Sapra, S. Wurtzite or zinc blende? Surface decides the crystal structure of nanocrystals. *CrystEngComm* **15**, 5458–5463 (2013).

42. Gao, Y. & Peng, X. Crystal structure control of CdSe nanocrystals in growth and nucleation: Dominating effects of surface versus interior structure. *J Am Chem Soc* **136**, 6724–6732 (2014).

43. Peng, X. *et al.* Shape control of CdSe nanocrystals. *Nature* **404**, 59–61 (2000).

44. Ostwald, W. Studien über die Bildung und Umwandlung fester Körper. *Zeitschrift für Physikalische Chemie* **22U**, 289–330 (1897).

45. Washington, A. L. *et al.* Ostwald's rule of stages and its role in CdSe quantum dot crystallization. *J Am Chem Soc* **134**, 17046–17052 (2012).

46. Cho, G., Park, Y., Hong, Y. K. & Ha, D. H. Ion exchange: an advanced synthetic method for complex nanoparticles. *Nano Converg* **6**, 1–17 (2019).

47. Rivest, J. B. & Jain, P. K. Cation exchange on the nanoscale: an emerging technique for new material synthesis, device fabrication, and chemical sensing. *Chem Soc Rev* **42**, 89–96 (2013).

48. Peng, Z. *et al.* First-Principles Study of Cu_9S_5: A Novel p-Type Conductive Semiconductor. *J. Phys. Chem. C* **121**, 23317–23323 (2017).

49. Rivest, J. B., Fong, L.-K., Jain, P. K., Toney, M. F. & Alivisatos, A. P. Size Dependence of a Temperature-Induced Solid–Solid Phase Transition in Copper(I) Sulfide. *J Phys Chem Lett* **2**, 2402–2406 (2011).

50. Pearson, R. G. Hard and Soft Acids and Bases. *J Am Chem Soc* **85**, 3533–3539 (1963).

51. Sharp, C. G., Leach, A. D. P. & Macdonald, J. E. Tolman's Electronic Parameter of the Ligand Predicts Phase in the Cation Exchange to CuFeS 2 Nanoparticles. *Nano Lett* **20**, 8556–8562 (2020).

52. Moon, G. D., Ko, S., Xia, Y. & Jeong, U. Chemical transformations in ultrathin chalcogenide nanowires. *ACS Nano* **4**, 2307–2319 (2010).

53. Ristova, M., Ristov, M., Tosev, P. & Mitreski, M. Silver doping of thin CdS films by an ion exchange process. *Thin Solid Films* **315**, 301–304 (1998).

54. Estrada, C. A., Zingaro, R. A., Meyers, E. A., Nair, P. K. & Nair, M. T. S. Modification of chemically deposited ZnSe thin films by ion exchange reaction with copper ions in solution. *Thin Solid Films* **247**, 208–212 (1994).

55. Hässelbarth, A. *et al.* Chemistry and photophysics of mixed CdS/HgS colloids. *Journal of Physical Chemistry* **97**, 5333–5340 (1993).

56. Son, D. H., Hughes, S. M., Yin, Y. & Alivisatos, A. P. Cation Exchange Reactions in Ionic Nanocrystals. *Science (1979)* **306**, 1009–1012 (2004).

57. Pietryga, J. M. *et al.* Utilizing the lability of lead selenide to produce heterostructured nanocrystals with bright, stable infrared emission. *J Am Chem Soc* **130**, 4879–4885 (2008).

58. Luther, J. M., Zheng, H., Sadtler, B. & Alivisatos, A. P. Synthesis of PbS nanorods and other ionic nanocrystals of complex morphology by sequential cation exchange reactions. *J Am Chem Soc* **131**, 16851–16857 (2009).

59. Fenton, J. L. & Schaak, R. E. Structure-Selective Cation Exchange in the Synthesis of Zincblende MnS and CoS Nanocrystals. *Angew. Chem. Int. Ed.* **56**, 6464–6467 (2017).

60. Powell, A. E., Hodges, J. M. & Schaak, R. E. Preserving Both Anion and Cation Sublattice Features during a Nanocrystal Cation-Exchange Reaction: Synthesis of Metastable Wurtzite-Type CoS and MnS. *J Am Chem Soc* **138**, 471–474 (2016).

61. Hernández-Pagán, E. A. *et al.* Transformation of the Anion Sublattice in the Cation-Exchange Synthesis of Au_2S from $Cu_{2-x}S$ Nanocrystals. *Chem Mater* **30**, 8843–8851 (2018).

62. Mohamed, M. B., Tonti, D., Al-Salman, A., Chemseddine, A. & Chergui, M. Synthesis of high quality zinc blende CdSe nanocrystals. *J Phys Chem B* **109**, 10533–10537 (2005).

63. Talapin, D. v. *et al.* Seeded growth of highly luminescent CdSe/CdS nanoheterostructures with rod and tetrapod morphologies. *Nano Lett* **7**, 2951–2959 (2007).

64. Deng, Z., Cao, L., Tang, F. & Zou, B. A new route to zinc-blende CdSe nanocrystals: Mechanism and synthesis. *J Phys Chem B* **109**, 16671–16675 (2005).

65. Shen, X. *et al.* Interlaced crystals having a perfect Bravais lattice and complex chemical order revealed by real-space crystallography. *Nat Commun* **5**, (2014).

66. Leach, A. D. P. *et al.* Defect luminescence from wurtzite $CuInS_2$ nanocrystals: Combined experimental and theoretical analysis. *J Phys Chem C* **120**, 5207–5212 (2016).

67. Xie, B., Hu, B., Jiang, L., Li, G. & Du, Z. The phase transformation of $CuInS_2$ from chalcopyrite to wurtzite. *Nanoscale Res Lett* **10**, 1–7 (2015).

68. Koo, B., Patel, R. N. & Korgel, B. A. Wurtzite-Chalcopyrite polytypism in $CuInS_2$ nanodisks. *Chem Mater* **21**, 1962–1966 (2009).

69. Yunxia, Q. *et al.* Synthesis and characterization of nanostructured wurtzite $CuInS_2$: A new cation disordered polymorph of $CuInS_2$. *J Phys Chem C* **113**, 3939–3944 (2009).

70. Norako, M. E. & Brutchey, R. L. Synthesis of metastable wurtzite $CuInSe_2$ nanocrystals. *Chem Mater* **22**, 1613–1615 (2010).

71. Omata, T. *et al.* Wurtzite $CuGaO_2$: A new direct and narrow band gap oxide semiconductor applicable as a solar cell absorber. *J Am Chem Soc* **136**, 3378–3381 (2014).

72. Vaure, L. *et al.* Doping and Surface Effects of $CuFeS_2$ Nanocrystals Used in Thermoelectric Nanocomposites. *ChemNanoMat* **4**, 982–991 (2018).

73. Vahidshad, Y., Mirkazemi, S. M., Tahir, M. N., Ghasemzadeh, R. & Tremel, W. Synthesis of $CuFeS_2$ nanoparticles by one-pot facile method. *J. Nanostructures* **7**, 284–291 (2017).

74. Mahler, B., Lequeux, N. & Dubertret, B. Ligand-controlled polytypism of thick-shell CdSe/CdS nanocrystals. *J Am Chem Soc* **132**, 953–959 (2010).

75. Huang, J., Kovalenko, M. v & Talapin, D. v. Alkyl chains of surface ligands affect polytypism of CdSe nanocrystals and play an important role in the synthesis of anisotropic nanoheterostructures. *J Am Chem Soc* **132**, 15866–15868 (2010).

76. Kuzuya, T., Yamamuro, S., Hihara, T. & Sumiyama, K. Water-free solution synthesis of monodisperse Cu_2S nanocrystals. *Chem Lett* **33**, 352–353 (2004).

77. Leach, A. D. P., Mast, L. G., Hernández-Pagán, E. A. & Macdonald, J. E. Phase dependent visible to near-infrared photoluminescence of $CuInS_2$ nanocrystals. *J Mater Chem C* **3**, 3258–3265 (2015).

78. Hernández-Pagán, E. A., Leach, A. D. P., Rhodes, J. M., Sarkar, S. & Macdonald, J. E. A synthetic exploration of metal-semiconductor hybrid particles of $CuInS_2$. *Chem Mater* **27**, 7969–7976 (2015).

79. Tappan, B. A., Barim, G., Kwok, J. C. & Brutchey, R. L. Utilizing diselenide precursors toward rationally controlled synthesis of metastable $CuInSe_2$ nanocrystals. *Chem Mater* **30**, 5704–5713 (2018).

80. Beberwyck, B. J., Surendranath, Y. & Alivisatos, A. P. Cation exchange: A versatile tool for nanomaterials synthesis. *J Phys Chem C* **117**, 19759–19770 (2013).

81. De Trizio, L. & Manna, L. Forging colloidal nanostructures via cation exchange reactions. *Chem Rev* **116**, 10852–10887 (2016).

82. Kumar, P., Uma, S. & Nagarajan, R. Precursor driven one pot synthesis of wurtzite and chalcopyrite $CuFeS_2$. *Chem Commun* **49**, 7316–7318 (2013).

83. Ghosh, S. *et al.* Colloidal $CuFeS_2$ nanocrystals: Intermediate Fe d-band leads to high photothermal conversion efficiency. *Chem Mater* **28**, 4848–4858 (2016).

84. Robinson, E. H., Turo, M. J. & Macdonald, J. E. Controlled Surface Chemistry for the Directed Attachment of Copper(I) Sulfide Nanocrystals. *Chemistry of Materials* **29**, 3854–3857 (2017).

85. Kruszynska, M. *et al.* Size and shape control of colloidal copper(I) sulfide nanorods. *ACS Nano* **6**, 5889–5896 (2012).

86. Zheng, H. *et al.* Observation of transient structural-transformation dynamics in a Cu_2S nanorod. *Science (1979)* **333**, 206–209 (2011).

87. Van Der Stam, W. *et al.* Luminescent $CuInS_2$ quantum dots by partial cation exchange in $Cu_{2-x}S$ nanocrystals. *Chem Mater* **27**, 621–628 (2015).

88. Chang, J. & Waclawik, E. R. Controlled synthesis of $CuInS_2$, Cu_2SnS_3 and Cu_2ZnSnS_4 nano-structures: Insight into the universal phase-selectivity mechanism. *CrystEngComm* **15**, 5612–5619 (2013).

89. Kar, P., Farsinezhad, S., Zhang, X. & Shankar, K. Anodic Cu_2S and CuS nanorod and nanowall arrays: Preparation, properties and application in CO_2 photoreduction. *Nanoscale* **6**, 14305–14318 (2014).

90. Li, S. *et al.* Synthesis and assembly of monodisperse spherical Cu_2S nanocrystals. *J Colloid Interface Sci* **330**, 483–487 (2009).

91. Kruszynska, M., Borchert, H., Parisi, J. & Kolny-Olesiak, J. Synthesis and shape control of $CuInS_2$ nanoparticles. *J Am Chem Soc* **132**, 15976–15986 (2010).

92. Tolman, C. A. Steric effects of phosphorus ligands in organometallic chemistry and homogeneous catalysis. *Chem Rev* **77**, 313–348 (1977).

93. Alice Dorinda Penrice Leach *et al.* The phase dependent optoelectronic properties of ternary I-III-VI_2 semiconductor nanocrystals and their synthesis. (2017).

94. Macdonald, J. E., Bar Sadan, M., Houben, L., Popov, I. & Banin, U. Hybrid nanoscale inorganic cages. *Nat Mater* **9**, 810–815 (2010).

95. Han, W. *et al.* Synthesis and shape-tailoring of copper sulfide/indium sulfide-based nanocrystals. *J Am Chem Soc* **130**, 13152–13161 (2008).

96. Meyer, M., Albrecht-Gary, A. M., Dietrich-Buchecker, C. O. & Sauvage, J. P. π-π stacking-induced cooperativity in copper(I) complexes with phenanthroline ligands. *Inorg Chem* **38**, 2279–2287 (1999).

97. Kamsu Kom, J., Flahaut, J., Domange, L. & Chaudron, M. G. Sur deux séries de composés ternaires, derivés du bore: $CuBS_2$ et $CuBSe_2$, et dérives du posphore: $CuPS_2$ et $CuPSe_2$. *Comptes rendus* 3919–3922 (1963).

98. Pan, D. *et al.* Synthesis of Cu-In-S ternary nanocrystals with tunable structure and composition. *J Am Chem Soc* **130**, 5620–5621 (2008).

99. Nelson, A., Ha, D. H. & Robinson, R. D. Selective etching of copper sulfide nanoparticles and heterostructures through sulfur abstraction: phase transformations and optical properties. *Chem Mater* **28**, 8530–8541 (2016).

100. Hernández-Pagán, E. A., Robinson, E. H., La Croix, A. D. & MacDonald, J. E. Direct synthesis of novel $Cu_{2-x}Se$ wurtzite phase. *Chem Mater* **31**, 4619–4624 (2019).

101. Prasad, S. & Pandey, B. D. Alternative processes for treatment of chalcopyrite - A review. *Miner Eng* **11**, 763–781 (1998).

102. Cotton, S. A. Iron(III) chloride and its coordination chemistry. *J Coord Chem* **71**, 3415–3443 (2018).

103. Shin, J. W., Han, J. H., Rowthu, S. R., Kim, B. G. & Min, K. S. Synthesis, Crystal structure, and Magnetic Properties of Dinuclear Iron(III) Complexes with Methoxo Bridges. *Bull Korean Chem Soc* **31**, 3617–3622 (2010).

104. Steimle, B. C., Lord, R. W. & Schaak, R. E. Phosphine-Induced Phase Transition in Copper Sulfide Nanoparticles Prior to Initiation of a Cation Exchange Reaction. *J Am Chem Soc* **142**, 13345–13349 (2020).

105. Manna, L., Scher, E. C. & Alivisatos, A. P. Synthesis of Soluble and Processable Rod-, Arrow-, Teardrop-, and Tetrapod-Shaped CdSe Nanocrystals. *J. Am. Chem. Soc.* **122**, 12700–12706 (2000).

106. Sahu, A., Qi, L., Kang, M. S., Deng, D. & Norris, D. J. Facile synthesis of silver chalcogenide (Ag_2E; E = Se, S, Te) semiconductor nanocrystals. *J Am Chem Soc* **133**, 6509–6512 (2011).

107. Coughlan, C. *et al.* Compound copper chalcogenide nanocrystals. *Chem Rev* **117**, 5865–6109 (2017).

108. Wang, L., Guan, Z. & Tang, A. Multinary copper-based chalcogenide semiconductor nanocrystals: synthesis and applications in light-emitting diodes and bioimaging. *Journal of Nanoparticle Research* **22**, (2020).

109. Gui, R., Jin, H., Wang, Z. & Tan, L. Recent advances in synthetic methods and applications of colloidal silver chalcogenide quantum dots. *Coord Chem Rev* **296**, 91–124 (2015).

110. Mu, L., Wang, F., Sadtler, B., Loomis, R. A. & Buhro, W. E. Influence of the Nanoscale Kirkendall Effect on the Morphology of Copper Indium Disulfide Nanoplatelets Synthesized by Ion Exchange. *ACS Nano* **9**, 7419–7428 (2015).

111. Li, H. *et al.* Sequential cation exchange in nanocrystals: Preservation of crystal phase and formation of metastable phases. *Nano Lett* **11**, 4964–4970 (2011).

112. Park, J., Zheng, H., Jun, Y. W. & Alivisatos, A. P. Hetero-epitaxial anion exchange yields single-crystalline hollow nanoparticles. *J Am Chem Soc* **131**, 13943–13945 (2009).

113. Hodges, J. M., Kletetschka, K., Fenton, J. L., Read, C. G. & Schaak, R. E. Sequential Anion and Cation Exchange Reactions for Complete Material Transformations of Nanoparticles with Morphological Retention. *Angew. Chem. Int. Ed.* **54**, 8669–8672 (2015).

114. Steimle, B. C., Fenton, J. L. & Schaak, R. E. Rational construction of a scalable heterostructured nanorod megalibrary. *Science (1979)* **367**, 418–424 (2020).

115. Schaak, R. E., Steimle, B. C. & Fenton, J. L. Made-to-Order Heterostructured Nanoparticle Libraries. *Acc Chem Res* **53**, (2020).

116. Steimle, B. C. *et al.* Experimental Insights into Partial Cation Exchange Reactions for Synthesizing Heterostructured Metal Sulfide Nanocrystals. *Chem Mater* **32**, 5461–5482 (2020).

117. Patel, M., Kim, H. S. & Kim, J. Wafer-scale production of vertical SnS multilayers for high-performing photoelectric devices. *Nanoscale* **9**, 15804–15812 (2017).

118. Ahmet, I. Y. *et al.* Evaluation of AA-CVD deposited phase pure polymorphs of SnS for thin films solar cells. *RSC Adv* **9**, 14899–14909 (2019).

119. González-Flores, V. E., Mohan, R. N., Ballinas-Morales, R., Nair, M. T. S. & Nair, P. K. Thin film solar cells of chemically deposited SnS of cubic and orthorhombic structures. *Thin Solid Films* **672**, 62–65 (2019).

120. Patra, B. K., Sarkar, S., Guria, A. K. & Pradhan, N. Monodisperse SnS Nanocrystals: In Just 5 Seconds. *J Phys Chem Lett* **4**, 3929–3934 (2013).

121. Rabkin, A. *et al.* New nanocrystalline materials: A previously unknown simple cubic phase in the SnS binary system. *Nano Lett* **15**, 2174–2179 (2015).

122. Abutbul, R. E. *et al.* Synthesis and properties of nanocrystalline π-SnS-a new cubic phase of tin sulphide. *RSC Adv* **6**, 5848–5855 (2016).

123. Chen, K. *et al.* Structural and electronic evolution in the Cu_3SbS_4-Cu_3SnS_4 solid solution. *J Mater Chem C Mater* **8**, 11508–11516 (2020).

124. Tu, R. *et al.* Influence of the Ion Coordination Number on Cation Exchange Reactions with Copper Telluride Nanocrystals. *J Am Chem Soc* **138**, 7082–7090 (2016).

125. Casavola, M. *et al.* Anisotropic Cation Exchange in PbSe/CdSe Core/Shell Nanocrystals of Different Geometry. *Chem Mater* **24**, 294–302 (2012).

126. Lambert, K., De Geyter, B., Moreels, I. & Hens, Z. PbTe|CdTe Core|Shell particles by cation exchange, a HR-TEM study. *Chem Mater* **21**, 778–780 (2009).

127. Bouet, C. *et al.* Synthesis of zinc and lead chalcogenide core and core/shell nanoplatelets using sequential cation exchange reactions. *Chem Mater* **26**, 3002–3008 (2014).

128. Morimoto, N. & Kullerud, G. Polymorphism in Digenite. *Am Mineral* **48**, 110–123 (1963).

129. Zhang, J. *et al.* Preparation of Cd/Pb Chalcogenide Heterostructured Janus Particles via Controllable Cation Exchange. *ACS Nano* **9**, 7151–7163 (2015).

130. Mumme, G. & Gable, W. The Crystal Structure of Roxbyite, $Cu_{58}S_{32}$. *The Canadian Mineralogist* **50**, 423–430 (2012).

131. Abutbul, R. E. & Golan, Y. Chemical epitaxy of π-phase cubic tin monosulphide. *CrystEngComm* **22**, 6170–6181 (2020).

132. Yang, J. X., Zhao, H. L., Gong, H. R., Song, M. & Ren, Q. Q. Proposed mechanism of HCP → FCC phase transition in titianium through first principles calculation and experiments. *Sci Rep* **8**, 23 (2018).

133. Nair, M. T. S., Guerrero, L. & Nair, P. K. Conversion of chemically deposited CuS thin films to Cu1.8S and Cu1.96S by annealing. *Semicond Sci Technol* **13**, 1164–1169 (1998).

134. Lee, S. *et al.* Transformation from $Cu_{2-x}S$ Nanodisks to $Cu_{2-x}S$@$CuInS_2$ Heteronanodisks via Cation Exchange. *Chem Mater* **28**, 3337–3344 (2016).

135. de Trizio, L. *et al.* Sn cation valency dependence in cation exchange reactions involving $Cu_{2-x}Se$ nanocrystals. *J Am Chem Soc* **136**, 16277–16284 (2014).

136. Sadtler, B. *et al.* Selective facet reactivity during cation exchange in cadmium sulfide nanorods. *J Am Chem Soc* **131**, 5285–5293 (2009).

137. Ha, D. H. *et al.* Solid-solid phase transformations induced through cation exchange and strain in 2D heterostructured copper sulfide nanocrystals. *Nano Lett* **14**, 7090–7099 (2014).

138. Lesnyak, V. *et al.* Alloyed copper chalcogenide nanoplatelets via partial cation exchange reactions. *ACS Nano* **8**, 8407–8418 (2014).

139. Lee, D. *et al.* Direct Cd-to-Pb Exchange of CdSe Nanorods into PbSe/CdSe Axial Heterojunction Nanorods. *Chem Mater* **27**, 5295–5304 (2015).

140. De Trizio, L. *et al.* $Cu_{3-x}P$ nanocrystals as a material platform for near-infrared plasmonics and cation exchange reactions. *Chem Mater* **27**, 1120–1128 (2015).

141. Adel, P., Wolf, A., Kodanek, T. & Dorfs, D. Segmented CdSe@CdS/ZnS nanorods synthesized via a partial ion exchange sequence. *Chem Mater* **26**, 3121–3127 (2014).

142. Yalcin, A. O. *et al.* Atomic resolution monitoring of cation exchange in CdSe-PbSe heteronanocrystals during epitaxial solid-solid-vapor growth. *Nano Lett* **14**, 3661–3667 (2014).

143. Jain, P. K., Amirav, L., Aloni, S. & Alivisatos, A. P. Nanoheterostructure cation exchange: Anionic framework conservation. *J Am Chem Soc* **132**, 9997–9999 (2010).

144. Ott, F. D., Spiegel, L. L., Norris, D. J. & Erwin, S. C. Microscopic theory of cation exchange in CdSe nanocrystals. *Phys Rev Lett* **113**, 1–5 (2014).

145. Fan, Z., Lin, L. C., Buijs, W., Vlugt, T. J. H. & van Huis, M. A. Atomistic understanding of cation exchange in PbS nanocrystals using simulations with pseudoligands. *Nat Commun* **7**, (2016).

146. Eswar Neerugatti, K. R., Shivaji Pawar, P. & Heo, J. Differential growth and evaluation of band structure of π-SnS for thin-film solar cell applications. *Mater Lett* **284**, 129026 (2021).

147. Finn, S. T. & Macdonald, J. E. Petaled molybdenum disulfide surfaces: Facile synthesis of a superior cathode for QDSSCs. *Adv Energy Mater* **4**, 1–6 (2014).

148. Zhao, K., Yu, H., Zhang, H. & Zhong, X. Electroplating Cuprous Sulfide Counter Electrode for High-Efficiency Long-Term Stability Quantum Dot Sensitized Solar Cells. *The Journal of Physical Chemistry C* **118**, 5683–5690 (2014).

149. Hodes, G., Manassen, J. & Cahen, D. Electrocatalytic Electrodes for the Polysulfide Redox System. *J Electrochem Soc* **127**, 544–549 (1980).

150. Yong, X. & Schoonen, M. A. A. The absolute energy positions of conduction and valence bands of selected semiconducting minerals. *American Mineralogist* **85**, 543–556 (2000).

151. Hens, Z. & Martins, J. C. A solution NMR toolbox for characterizing the surface chemistry of colloidal nanocrystals. *Chem Mater* **25**, 1211–1221 (2013).

152. Gariano, G. *et al.* Role of the Crystal Structure in Cation Exchange Reactions Involving Colloidal Cu2Se Nanocrystals. *J Am Chem Soc* **139**, 9583–9590 (2017).

153. Fenton, J. L., Steimle, B. C. & Schaak, R. E. Structure-Selective Synthesis of Wurtzite and Zincblende ZnS, CdS, and CuInS 2 Using Nanoparticle Cation Exchange Reactions. *Inorg Chem* **58**, 672–678 (2019).

154. Dong, H. S., Hughes, S. M., Yin, Y. & Alivisatos, A. P. Cation exchange reactions in ionic nanocrystals. *Science (1979)* **306**, 1009–1012 (2004).

155. Sarkar, S., Sharp, C. G., Finn, S. T. & Macdonald, J. E. Cracking Shells and Scrambling Eggs: Intermediate Shell Formation and Anion Rearrangement in the Cation Exchange from π-SnS to Cu1.8S. *Chem Mater* **33**, 3011–3019 (2021).

156. Li, H. *et al.* Synthesis of uniform disk-shaped copper telluride nanocrystals and cation exchange to cadmium telluride quantum disks with stable red emission. *J Am Chem Soc* **135**, 12270–12278 (2013).

157. Lesnyak, V., Brescia, R., Messina, G. C. & Manna, L. Cu Vacancies Boost Cation Exchange Reactions in Copper Selenide Nanocrystals. *J Am Chem Soc* **137**, 9315–9323 (2015).

158. Xie, Y. *et al.* Copper sulfide nanocrystals with tunable composition by reduction of covellite nanocrystals with Cu+ ions. *J Am Chem Soc* **135**, 17630–17637 (2013).

159. Wang, X., Liu, X., Zhu, D. & Swihart, M. T. Controllable conversion of plasmonic Cu2−xS nanoparticles to Au2S by cation exchange and electron beam induced transformation of Cu2−xS–Au2S core/shell nanostructures. *Nanoscale* **6**, 8852–8857 (2014).

160. Yoon, D. *et al.* Plasmon Enhanced Direct Bandgap Emissions in Cu7S4@Au2S@Au Nanorings. *Small* **12**, 5728–5733 (2016).

161. Gan, X. Y., Sen, R. & Millstone, J. E. Connecting Cation Exchange and Metal Deposition Outcomes via Hume-Rothery-Like Design Rules Using Copper Selenide Nanoparticles. *J Am Chem Soc* **143**, 8137–8144 (2021).

162. Gilb, S., Weis, P., Furche, F., Alhrichs, R. & Kappes, M. M. Structures of small gold cluster cations (Aun+, n<14): Ion mobility measurements versus density functional calculations. *J Chem Phys* **116**, 4094 (2002).

163. Doña, J. M. & González-Velasco, J. The dependence of the surface diffusion coefficients of gold atoms on the potential: its influence on reconstruction of metal lattices. *Surf Sci* **274**, 205–214 (1992).

164. Rice, K. P., Saunders, A. E. & Stoykovich, M. P. Seed-mediated growth of shape-controlled wurtzite CdSe nanocrystals: Platelets, cubes, and rods. *J Am Chem Soc* **135**, 6669–6676 (2013).

165. Meden, A. Crystal Structure Solution from Powder Diffraction Data-State of the Art and Perspectives. in *Sixth Croatian-Slovenian Crystallographic Meeting* 615–633 (1998).

166. Nannenga, B. L. & Gonen, T. The cryo-EM method microcrystal electron diffraction (MicroED). *Nature Methods 2019 16:5* **16**, 369–379 (2019).

167. Own, C. S., Sinkler, W. & Marks, L. D. Rapid structure determination of a metal oxide from pseudo-kinematical electron diffraction data. *Ultramicroscopy* **106**, 114–122 (2006).

168. Moeck, P., Rouvimov, S. & Nicolopoulos, S. Precession electron diffraction and its utility for structural fingerprinting in the transmission electron microscope. *AIP Conf Proc* **1173**, 299 (2009).

169. Own, C. S., Dellby, N., Krivanek, O. L., Marks, L. D. & Murfitt, M. Aberration-corrected Precession Electron Diffraction. *Microscopy and Microanalysis* **13**, 96–97 (2007).

170. Eggeman, A. S. & Midgley, P. A. Precession Electron Diffraction. in *Advances in Imaging and Electron Physics* vol. 170 1–63 (Elsevier, 2012).

171. Vincent, R. & Midgley, P. A. Double conical beam-rocking system for measurement of integrated electron diffraction intensities. *Ultramicroscopy* **53**, 271–282 (1994).

172. Dilimon, V. S., Fonder, G., Delhalle, J. & Mekhalif, Z. Self-assembled monolayer formation on copper: A real time electrochemical impedance study. *J Phys Chem C* **115**, 18202–18207 (2011).

173. Pang, H. *et al.* Revealing an elusive metastable wurtzite CuFeS2 and the phase switching between wurtzite and chalcopyrite for thermoelectric thin films. *Acta Mater* **235**, 118090 (2022).

174. Tappan, B. A., Chu, W., Mecklenburg, M., Prezhdo, O. V. & Brutchey, R. L. Discovery of a Wurtzite-like $Cu_2FeSnSe_4$ Semiconductor Nanocrystal Polymorph and Implications for Related $CuFeSe_2$ Materials. *ACS Nano* **15**, 13463–13474 (2021).

175. Rahman, M. M. *et al.* Cadmium Selenide Quantum Dots for Solar Cell Applications: A Review. *Chem Asian J* **16**, 902–921 (2021).

176. Chen, B., Li, D. & Wang, F. InP Quantum Dots: Synthesis and Lighting Applications. *Small* **16**, 2002454 (2020).

177. Sen, S., Bera, S. & Pradhan, N. Maneuvering Tellurium Chemistry to Design Metal-Telluride Heterostructures for Diverse Applications. *Chem Mater* **34**, 9329–9343 (2022).

178. Rodríguez-Guadarrama, L. A., Escorcia-García, J., Alonso-Lemus, I. L. & Campos-Álvarez, J. Synthesis of π-SnS thin films through chemical bath deposition: effects of pH,

deposition time, and annealing temperature. *Journal of Materials Science: Materials in Electronics* **32**, 7464–7480 (2021).

179. Whittles, T. J. *et al.* Band Alignments, Valence Bands, and Core Levels in the Tin Sulfides SnS, SnS_2, and Sn_2S_3: Experiment and Theory. *Chem Mater* **28**, 3718–3726 (2016).